Control, Measurement and Entanglement of Remote Quantum Spin Registers in Diamond

Hannes Bernien

Control, measurement and entanglement of remote quantum spin registers in diamond

Control, measurement and entanglement of remote quantum spin registers in diamond

Proefschrift

ter verkrijging van de graad van doctor
aan de Technische Universtiteit Delft,
op gezag van de Rector Magnificus Prof. ir. K.C.A.M. Luyben,
voorzitter van het College voor Promoties,
in het openbaar te verdedigen op maandag 10 februari 2014 om 12:30 uur

door

Hannes BERNIEN

Diplom-Physiker, Universität Hannover, Duitsland
geboren te Rostock, Duitsland

Dit proefschrift is goedgekeurd door de promotor:

Prof. dr. ir. R. Hanson

Samenstelling promotiecommissie:

Rector Magnificus,	voorzitter
Prof. dr. ir. R. Hanson,	Technische Universiteit Delft, promotor
Prof. dr. ir. L.P. Kouwenhoven,	Technische Universiteit Delft
Prof. dr. ir. H.S.J. van der Zant,	Technische Universiteit Delft
Prof. dr. G. Rempe,	Max-Planck-Institut für Quantenoptik, München, Duitsland
Prof. dr. D.P. DiVincenzo,	Rheinisch-Westfälische Technische Hochschule Aachen en Forschungszentrum Jülich, Duitsland
Dr. S. Benjamin,	University of Oxford, Engeland
Prof. dr. Y.M. Blanter,	Technische Universiteit Delft, reservelid

Contents

Contents

---

x

INTRODUCTION

H. Bernien & W. Pfaff

The ability to control, measure and entangle few-qubit quantum registers creates unique opportunities for studying the non-classical features of quantum mechanics. Apart from being of great fundamental interest, this ability is an important requirement for future technologies powered by quantum mechanics, such as quantum computers and quantum networks (chapter 1.1). A promising candidate platform for constructing and studying elementary building blocks for such technologies are spins in diamond (chapter 1.2). This thesis presents a set of experiments that first establish a universal tool-box for quantum control and measurement of spins in diamond. We then make use of these tools to create entanglement between non-interacting remote spins and to perform deterministic quantum teleportation between them.

1.1   Quantum computers and quantum networks

Quantum mechanics is widely regarded as one of the most successful theories in physics, and to the best of our knowledge no experiment has been performed thus far that contradicts it. This accuracy is remarkable because today's experimental possibilities go well beyond of what the founders of quantum theory thought was achievable — Schrödinger for instance famously wrote[1]:

> *"we never experiment with just one electron or atom or (small) molecule. In thought-experiments we sometimes assume that we do; this invariably entails ridiculous consequences [...]*
>
> *it is fair to state that we are not experimenting with single particles, any more than we can raise Ichthyosauria in the zoo."*

This statement clearly does not hold any more, as experimental techniques to study single particles have been developed with great success in the recent decades — acknowledged by the recent awarding of the 2012 Nobel Prize in Physics to Serge Haroche and David J. Wineland *"for ground-breaking experimental methods that enable measuring and manipulation of individual quantum systems."*

Nonetheless, quantum mechanical predictions — and in particular their *"ridiculous consequences"*, such as quantum entanglement[2,3] — prevail, and we are lead to believe that seemingly exotic features of quantum theory are not merely side-effects of mathematical modelling, but real phenomena that can be observed. This development has in turn triggered great interest in the possibility to use these phenomena in new technologies that can outperform counterparts that operate solely on the basis of classical physics.

As experimental quantum physicists we are interested in studying and controlling the quintessential features of quantum mechanics on the smallest scale. These efforts are made in the hope that we can resolve fundamental disputes and questions about the interpretation of quantum theory[4,5], as well as demonstrate the feasibility of new quantum technologies.

In particular, quantum information processing can help to overcome limitations faced in classical computing. An illustrating example is quantum physics itself: assume we want to simulate a molecule of 500 degrees of freedom, where each of those dimensions has at least two possible states. The full state information consists of the complex amplitudes of all $\geq 2^{500}$ terms in the general superposition state — more numbers than the estimated total of atoms in the observable universe and certainly intractable by any classical computer. However, if controlled and preserved well enough, a quantum system that can be mapped to the very molecule to be described can be used for the task[6] — an idea that has been generalized to universal quantum simulators[7].

Furthermore it has become clear that also more general computational problems can be treated more efficiently when generalizing the classical computer to a quantum Turing

machine[8,9], where the classical bit that takes values of either 0 or 1 is replaced by the quantum bit (qubit) that can be in superpositions of basis states $|0\rangle$ and $|1\rangle$. This idea has since given raise to the new discipline of quantum information processing[10,11]. Potential applications that generated of lot of interest include the factorisation of large numbers[12] and the searching of unsorted databases[13].

The implementation of quantum information protocols demands very good control over individual and composite quantum systems[14]. Notably, quantum entanglement between qubits can be employed to achieve a performance-enhancement over classical protocols[15,16]. Furthermore, the ability to perform projective quantum measurements is desirable for a number of applications, for instance quantum error correction[10].

For the communication of quantum information and for distributed quantum computing quantum networks have been devised[17]. If entanglement between (remote) nodes of such a network can be established, quantum states and operations can be transmitted via teleportation[18,19]. The entanglement required can be generated, for instance, by interference and measurement of photons[20].

The realisation of an extended network of quantum registers or computers that are linked by entanglement would allow us to study quantum physics at a truly macroscopic scale and test its limits. At the same time this step could enable radically new applications in computation and communication. The focus of this work is the generation of entanglement between non-interacting solid-state qubits by quantum measurement, in order to show a pathway for creating prototypes of such quantum networks.

1.2 Spins in diamond as building block for quantum technologies

We implement quantum registers with single spins that are associated to the Nitrogen Vacancy (NV) colour defect in diamond. The NV centre has gained much interest in experimental quantum physics since the first observation of a single such centre in 1997[21]: the defect behaves much like a single ion or small molecule, but comes "pre-packaged" in a robust solid-state environment that it does not strongly interact with. The NV centre displays quantum phenomena that can be accessed with relatively simple experimental arrangements, and under moderate environment conditions.

The NV shows photoluminescence under excitation with visible light and is a stable single-photon emitter[22]. It has an electronic spin that can be initialized and read out optically, and manipulated with standard magnetic resonance techniques[23]. Remarkably, these properties are available even at room temperature. As a result, the NV has been used for experiments in various aspects of quantum science, from sensitive metrology[24–27], studies of single-spin decoherence[28–30], to fundamental tests of quantum mechanics[31–33], to name only a few.

Recent critical advances show the potential for NV centres in quantum information processing: It has been shown that nuclear spins interacting with the NV electronic spin can be used as qubits[34–36], opening up the possibility for building local multi-qubit quantum
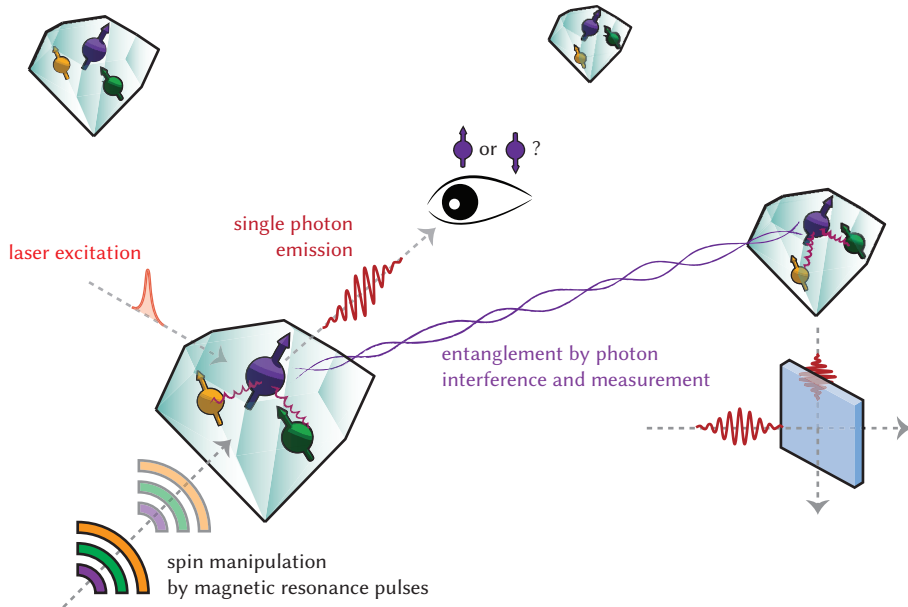
Figure 1.1 | Vision of a macroscopic quantum network based on spins in diamond.
Nodes consist of single NV centres in diamonds that are separated by macroscopic distances
(metres up to kilometres). The NV electronic spin (purple) can be measured optically, and
serves as the interface for a quantum register of nuclear spins (orange, green). Entanglement
between nodes is established by interference and measurement of photons that are correlated
with the electron spins.

registers. Further, at cryogenic temperatures the electronic spin can be interfaced coherently
with photons [37], enabling linking of such registers to macroscopic networks. On these
grounds we believe that the NV centre is a promising platform for implementing quantum
registers and networks. A cartoon of the architecture we envision is shown in Fig. 1.1.

1.3   Thesis overview

In **chapter 2** we outline the relevant physical properties of the NV centre: we first discuss
how the electronic spin can serve as the central qubit of a nuclear spin register, and how it can
be used as the optical interface to this register. Furthermore, we explain how entanglement
between remote NV centres can be established.

   Chapter 3 describes the experimental details of our measurements. We discuss the
principles of addressing single NV centres and how to fabricate devices that enable high

fidelity spin control and readout. Finally, we discuss the experimental setup used.

In **chapter 4** we show that optical transitions of the NV centre can be manipulated coherently. We identify the main mechanism for decoherence and develop a method to overcome it.

The energy levels involved in the optical cycle are investigated further in **chapter 5**. We determine the spin-dependent intersystem crossing probabilities between the triplet and singlet states.

In **chapter 6** we implement a projective quantum measurement of the electronic spin of the NV centre and nuclear spin states of the nitrogen and nearby ^{13}C-atoms. We use spin selective optical excitation at low temperatures combined with the high collection efficiency enabled by solid immersion lenses (chapter 3.2), allowing us to measure the spin states in a single shot.

Chapter 7 shows that NV centres are suitable for measurement-based entanglement protocols. We obtain indistinguishable photons from separate NVs and observe two-photon quantum interference.

We demonstrate generation of entanglement between two NV centre electronic spins that are separated by a macroscopic distance of three metres in **chapter 8**. We show how quantum interference and measurement of indistinguishable single photons from the NV centres can project the spins into a Bell-state.

By combining this remote entanglement with a local Bell-state measurement we are able to deterministically teleport the state of a nuclear spin qubit onto an electronic spin over a macroscopic distance of three metres (**chapter 9**).

We finally summarise the work presented in **chapter 10** and discuss the future of this line of experiments.

1.4   Bibliography

[1]   E. Schrödinger. Are there quantum jumps? Part II. *Brit. J. Phil. Sci.* **3**, 233 (1952).

[2]   S. J. Freedman and J. F. Clauser. Experimental Test of Local Hidden-Variable Theories. *Phys. Rev. Lett.* **28**, 938 (1972).

[3]   A. Aspect, P. Grangier and G. Roger. Experimental Tests of Realistic Local Theories via Bell's Theorem. *Phys. Rev. Lett.* **47**, 460 (1981).

[4]   M. Schlosshauer, J. Kofler and A. Zeilinger. A Snapshot of Foundational Attitudes Toward Quantum Mechanics. *Stud. Hist. Phil. Mod. Phys.* **44**, 222 (2013).

[5]   G. A. D. Briggs, J. N. Butterfield and A. Zeilinger. The Oxford Questions on the foundations of quantum physics. *Proc. R. Soc. Lond. A* **469**, 20130299 (2013).

[6]   R. P. Feynman. Simulating physics with computers. *Int. J. Theor. Phys.* **21**, 467 (1982).

[7]   S. Lloyd. Universal Quantum Simulators. *Science* **273**, 1073 (1996).

[8]   P. Benioff. Quantum mechanical hamiltonian models of turing machines. *J. Stat. Phys.* **29**, 515 (1982).

[9]   D. Deutsch. Quantum theory, the Church-Turing principle and the universal quantum computer. *Proc. R. Soc. Lond. A* **400**, 97 (1985).

[10] M. A. Nielsen and I. L. Chuang. *Quantum Computation and Quantum Information.* Cambridge University Press, Cambridge (2001).

[11] N. D. Mermin. *Quantum computer science: an introduction.* Cambridge University Press, Cambridge (2007).

[12] P. W. Shor. Polynomial-Time Algorithms for Prime Factorization and Discrete Logarithms on a Quantum Computer. *SIAM J. Comput.* **26**, 1484 (1997).

[13] L. K. Grover. A fast quantum mechanical algorithm for database search. *Proceedings of the twenty-eighth annual ACM symposium on Theory of computing* 212–219 (1996).

[14] D. P. DiVincenzo. The Physical Implementation of Quantum Computation. *Fortschr. Phys.* **48**, 771 (2000).

[15] C. H. Bennett and D. P. DiVincenzo. Quantum information and computation. *Nature* **404**, 247 (2000).

[16] R. Jozsa and N. Linden. On the role of entanglement in quantum-computational speed-up. *Proc. R. Soc. Lond. A* **459**, 2011 (2003).

[17] H. J. Kimble. The quantum internet. *Nature* **453**, 1023 (2008).

[18] C. H. Bennett *et al.* Teleporting an unknown quantum state via dual classical and Einstein-Podolsky-Rosen channels. *Phys. Rev. Lett.* **70**, 1895 (1993).

[19] D. Gottesman and I. L. Chuang. Demonstrating the viability of universal quantum computation using teleportation and single-qubit operations. *Nature* **402**, 390 (1999).

[20] L.-M. Duan, M. D. Lukin, J. I. Cirac and P. Zoller. Long-distance quantum communication with atomic ensembles and linear optics. *Nature* **414**, 413 (2001).

[21] A. Gruber *et al.* Scanning Confocal Optical Microscopy and Magnetic Resonance on Single Defect Centers. *Science* **276**, 2012 (1997).

[22] C. Kurtsiefer, S. Mayer, P. Zarda and H. Weinfurter. Stable Solid-State Source of Single Photons. *Phys. Rev. Lett.* **85**, 290 (2000).

[23] F. Jelezko, T. Gaebel, I. Popa, A. Gruber and J. Wrachtrup. Observation of coherent oscillations in a single electron spin. *Phys. Rev. Lett.* **92**, 076401 (2004).

[24] J. R. Maze *et al.* Nanoscale magnetic sensing with an individual electronic spin in diamond. *Nature* **455**, 644 (2008).

[25] G. Balasubramanian *et al.* Nanoscale imaging magnetometry with diamond spins under ambient conditions. *Nature* **455**, 648 (2008).

[26] F. Dolde *et al.* Electric-field sensing using single diamond spins. *Nature Phys.* **7**, 459 (2011).

[27] G. Kucsko *et al.* Nanometre-scale thermometry in a living cell. *Nature* **500**, 54 (2013).

[28] G. de Lange, Z. H. Wang, D. Riste, V. V. Dobrovitski and R. Hanson. Universal Dynamical Decoupling of a Single Solid-State Spin from a Spin Bath. *Science* **330**, 60 (2010).

[29] C. A. Ryan, J. S. Hodges and D. G. Cory. Robust Decoupling Techniques to Extend Quantum Coherence in Diamond. *Phys. Rev. Lett.* **105**, 200402 (2010).

[30] B. Naydenov *et al.* Dynamical decoupling of a single-electron spin at room temperature. *Phys. Rev. B* **83**, 81201 (2011).

[31] V. Jacques *et al.* Experimental Realization of Wheeler's Delayed-Choice Gedanken Experiment. *Science* **315**, 966 (2007).

[32] G. Waldherr, P. Neumann, S. F. Huelga, F. Jelezko and J. Wrachtrup. Violation of a temporal bell inequality for single spins in a diamond defect center. *Phys. Rev. Lett.* **107**, 090401 (2011).

[33] R. E. George *et al.* Opening up three quantum boxes causes classically undetectable wavefunction collapse. *Proc. Natl. Acad. Sci. U.S.A.* **110**, 3777 (2013).

[34] F. Jelezko *et al.* Observation of Coherent Oscillation of a Single Nuclear Spin and Realization of a Two-Qubit Conditional Quantum Gate. *Phys. Rev. Lett.* **93**, 130501 (2004).

[35] M. V. G. Dutt *et al.* Quantum register based on individual electronic and nuclear spin qubits in diamond. *Science* **316**, 1312 (2007).

[36] P. Neumann *et al.* Multipartite Entanglement Among Single Spins in Diamond. *Science* **320**, 1326 (2008).

[37] E. Togan *et al.* Quantum entanglement between an optical photon and a solid-state spin qubit. *Nature* **466**, 730 (2010).

The NV centre in diamond as platform for quantum networks

H. Bernien & W. Pfaff

In this chapter we will outline the physical principles for using the NV centre as the elementary building block for quantum registers and quantum networks. In particular, we address the nature of the electronic spin and its suitability for serving both as a central qubit and an optical interface (chapter 2.2), and how a nuclear spin register around the electronic spin is formed (chapter 2.3). We finally lay out the principles for establishing entanglement between remote NV centres using a photonic channel (chapter 2.4).
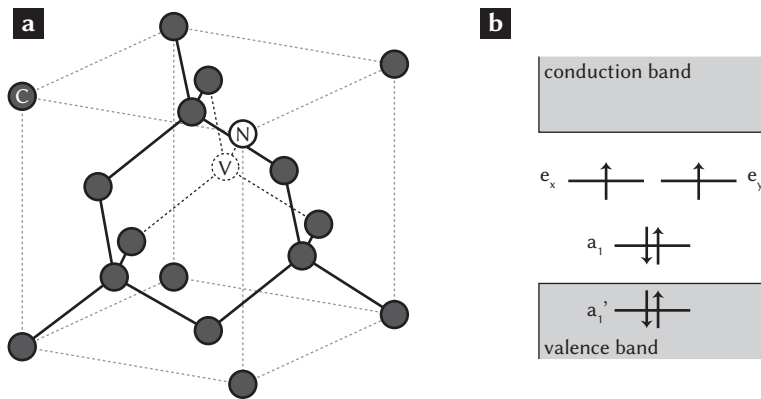
Figure 2.1 | Basic structure of the NV centre. a, The nitrogen-vacancy defect in the carbon-matrix of diamond is formed by a substitutional nitrogen atom (N) next to a lattice vacancy (V). **b,** Molecular orbitals (labels denote their symmetry) and their filling in the orbital ground state of NV^-. These orbitals are linear combinations of the hybridised sp^3 orbitals of the nitrogen and the 3 carbon atoms that transform according to the irreproducible representations of the C_{3v} symmetry group [1,2]. The lowest-lying orbital a_1' is located inside the valence band. The relevant physics of the NV centre is mainly governed by the occupation of the orbitals in the band gap. In the ground state of NV^- the orbital configuration is $a_1^2e^2$. Optical excitation can promote one electron to the first orbital excited state $a_1^1e^3$.

2.1 Introduction

The nitrogen-vacancy defect (NV) is a colour-centre in diamond consisting of a substitutional nitrogen atom and a neighbouring lattice vacancy (Fig. 2.1a). In its neutral charge state (NV^0) the defect hosts 5 electrons — 3 from the dangling bonds of the vacancy's next-neighbour carbon atoms, and 2 donor electrons from the nitrogen. In this work we are mainly concerned with the negatively charged state (NV^-), where an additional electron is captured from the environment.

The 6 electrons of NV^- occupy the available molecular orbitals in the ground state as shown in Fig. 2.1b. The two orbitals that have the highest energy are degenerate and host one unpaired electron each to form a spin triplet. Upon optical excitation one electron from the orbital below can be transferred to one of the two highest energy orbitals. Importantly, the energies of the ground as well as the first orbital excited state are located inside the band gap of diamond, resulting in ion-like properties of the defect.

In the following we will give only a brief overview of the features of the NV centre relevant for the experimental work presented. For more details we point the reader to the numerous reviews published very recently, covering both the fundamental properties of the defect [3,4]

as well as the current applications[5-11].

2.2 The electronic spin: central qubit and optical interface

In the simplified model of non interacting electrons both the ground state configuration $a_1^2 e^2$ and the first excited configuration $a_1^1 e^3$ have degenerate spin singlet and triplet states. This degeneracy is lifted by the Coulomb interaction which leads to spin triplet (S=1) ground states $^3A_2$ which are separated by 1.945 eV from the spin triplet excited states ^3E (Fig. 2.2)[1,2]. The exact positions of the singlet states are not yet determined[2] and are for this work summarised to one intermediate level. Adding spin-orbit and spin-spin interactions to the model splits the ground and excited triplet states.

Central qubit

Within the orbital ground state the $m_s = \pm 1$ levels are separated by a zero field splitting $D \approx 2.88$ GHz from the $m_s = 0$ state. The ground state is described by the Hamiltonian

$$\mathcal{H}_{GS} = DS_z^2 + \gamma_e \mathbf{B} \cdot \mathbf{S}, \tag{2.1}$$

where S_i are the Pauli spin operators and $\gamma_e = 2.802$ MHz/G is the gyromagnetic ratio. A magnetic field B_z parallel to the N-V axis splits the $m_s = \pm 1$ states by the Zeeman effect (Fig. 2.2d). For moderate field strengths the degeneracy between $m_s = -1$ and $m_s = +1$ is lifted and their transitions to $m_s = 0$ can be selectively driven by applying microwaves with the frequency of the corresponding transition[12]. We can define an effective two level system which serves as a qubit with $m_s = 0 := |0\rangle$ and $m_s = -1 := |1\rangle$ (equally well $m_s = +1$ can be defined as $|1\rangle$).

These qubit states are very robust. Coherence times of a few milliseconds can be observed even at room temperature and at low temperatures coherence times of single NVs beyond 10 ms for single NVs[13] and up to 0.5 s for ensembles[14] have been observed. There are two main reasons for these long times. First, the electronic energy levels lie deep within the large band gap of diamond (5.5 eV) and are therefore well isolated from the bulk electronic states. Second, the diamond lattice consists to 98.9% of spinless ^{12}C, leading to only slow dephasing from a fluctuating nuclear spin bath.

The limit on the coherence time is set by the remaining magnetic impurities. These form a spin bath which creates a fluctuating magnetic field at the NV location which leads to dephasing[15]. For type Ib diamonds the spin bath is dominated by nitrogen defect centres (P1) that have an electronic $S = 1/2$ spin. In type IIa diamonds the bath is given by the remaining ^{13}C nuclear spins ($I = 1/2$).

Optical interface

The spin-orbit and spin-spin interaction split the excited state triplet into four levels, two of which are doubly degenerate ($E_{1,2}$ and $E_{x,y}$). The spin of the $E_{x,y}$ states is $m_s = 0$. All others

states are superpositions of $m_s = +1$ and $m_s = -1$. The transitions between the ground state and the excited state are in the visible (637 nm) and follow the selection rules given in table 2.1[1]. At low temperature they can be resonantly excited using a laser of the corresponding frequency and this way different spin states can be selectively addressed.

	A_1	A_2	E_1	E_2	E_x	E_y
$^3A_{2,m_s=-1}$	σ_+	σ_+	σ_-	σ_-		
$^3A_{2,m_s=0}$					y	x
$^3A_{2,m_s=+1}$	σ_-	σ_-	σ_+	σ_+		

Table 2.1 | Optical selection rules. Transitions between the ground and excited states occur under the emission or absorption of a linearly polarised (x,y) or circularly polarised (σ_+, σ_-) photon.

The NV centre cannot also be excited off-resonantly with higher energy. In this way a phonon level above the excited state will be populated that quickly decays non radiatively into ^3E (see fig. 2.2a). During the emission the reverse process happens by which the NV either directly decays into the ground state (zero phonon line, ZPL) or via a phonon level above the ground state (phonon side band, PSB).

From the excited triplet state the NV centre can also decay to the metastable singlet states. This coupling is stronger for states with $m_s = \pm 1$ components than for $m_s = 0$ states. This difference results in a spin dependent fluorescence rate that allows to determine the spin state by averaging the fluorescence intensity over many experimental runs[3]. Decay from the singlets goes preferentially into $m_s = 0$, leading to spin polarisation under off-resonant excitation. The initialisation fidelity using this technique has been reported to range from 42–96%, depending on the experimental setting[4]. Higher initialisation fidelity and spin readout in a single shot can be achieved at low temperatures using spin selective resonant excitation (chapter 6).

The excited levels can be shifted by applying strain as well as by applying electric fields to the NV centre[16,17]. Electric fields along the N-V axis do not effect the spacing between the levels but offset the whole spectrum. Electric fields perpendicular to this axis break the C_{3v} symmetry and change the splittings between the levels (Fig. 2.2c). This also affects the spin components of the levels which are increasingly mixed with higher strain. The ability to tune the frequency of the emitted photons is crucial in order to link distant NV centres via a photonic channel.

2.3 Nuclear spins as quantum register

Nuclear spins in solids are promising candidates for quantum register qubits because of their long coherence times[18,19] and the availability of well-established nuclear magnetic resonance techniques to manipulate them[20,21]. In particular, nuclear spins in diamond that
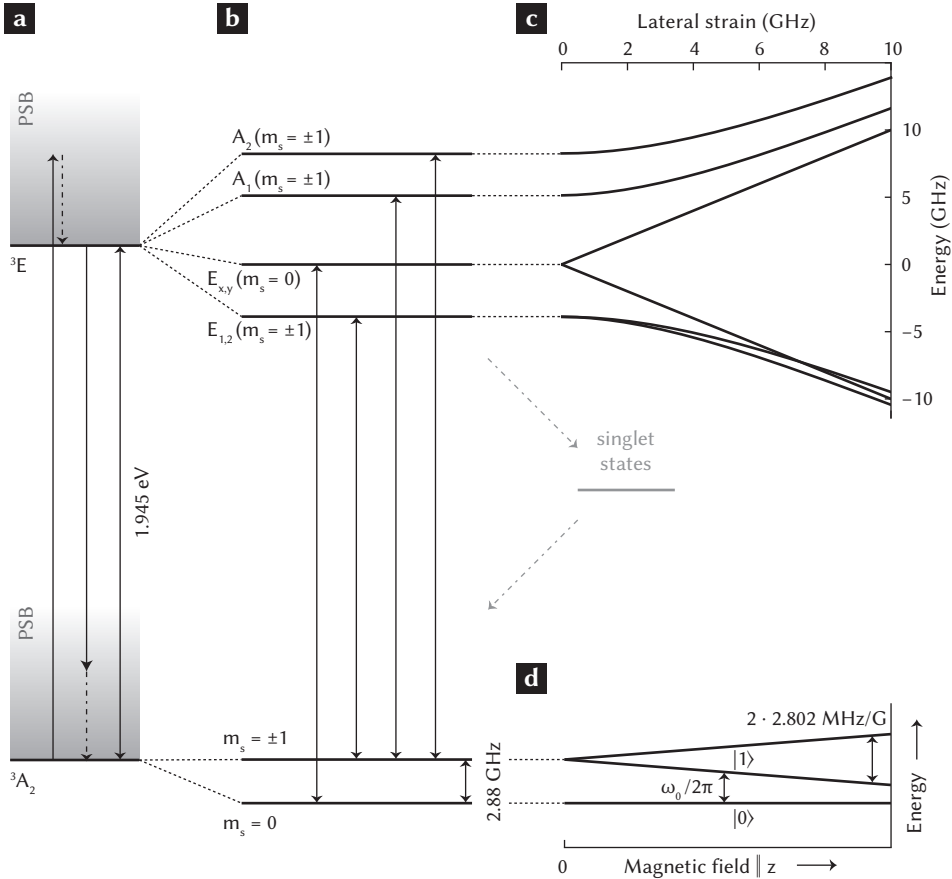
Figure 2.2 | Electronic level structure and optical excitation of NV⁻. a, The ground state triplet $^3A_2$ can be optically excited either resonantly to the ^3E excited or off-resonantly into higher lying levels in the phonon side band (PSB) that quickly decay to ^3E. Emission of photon can either occur directly or in to the PSB above the ground state. **b,** The ground state is split by the zero field splitting into one $m_s = 0$ and two degenerate $m_s = \pm 1$ states. Spin-spin and spin-orbit interactions split the excited state into four levels of which two are doubly degenerate. The labels indicate the symmetry of the state under C_{3v} transformations. Arrows indicate the allowed optical transitions. **c,** The excited state splittings are effected by strain (or equivalently by an electric field) that is applied perpendicular to the N-V-axis. With increasing strain the spin states of the levels are increasingly mixed. **d,** Magnetic fields along the N-V axis split the $m_s = \pm 1$ levels in the ground state by the Zeeman effect.

couple strongly to the electronic spin of an NV centre have shown great potential for use in quantum registers in a row of proof-of-principle experiments in the recent years [19,22–28].

We define nuclear spin qubits in the orbital ground state of NV⁻. The key ingredient that allows us to do so is the hyperfine interaction between nuclear spins and the NV electronic spin. This coupling causes a splitting of the electronic spin states $m_s = \pm 1$, with each of the sub-levels corresponding to a nuclear spin eigenstate that we can use as qubit basis state.

The exact nature of the basis states of a particular nuclear spin depends on the details of the hyperfine interaction, which is in general given by [20]

$$\mathcal{H}_{hf} = \mu_e \mu_n \sum_{\mu, \nu = x, y, z} S_\mu \left[\left(-\frac{8\pi}{3} |\psi(\mathbf{r}_n)|^2 + \left\langle \frac{1}{|\mathbf{r} - \mathbf{r}_n|^3} \right\rangle \right) \delta_{\mu\nu} - 3 \left\langle \frac{n_\mu n_\nu}{|\mathbf{r} - \mathbf{r}_n|^3} \right\rangle \right] I_\nu, \qquad (2.2)$$

where both Fermi contact and dipolar coupling are included. **S** and **I** are the electronic and nuclear spin operators, respectively, $\mu_{e,n}$ are the magnetic moments of the electron and nucleus, $\psi(\mathbf{r})$ is the electron wavefunction, $\mathbf{r}_n$ is the position of the nucleus, **n** is a unit vector along the $\mathbf{r} - \mathbf{r}_n$ axis, $\delta_{\mu\nu}$ is the Kronecker delta, and $\langle \cdot \rangle$ denotes the average.

For the case of small magnetic fields — corresponding to the experimental settings used throughout this thesis — this interaction can be simplified: the largest energy involved is the zero-field splitting in z direction, $D \approx 2\pi \times 2.88$ GHz, that defines the quantisation of the electron spin. One can make a secular approximation and neglect terms in the Hamiltonian that contain S_x or S_y, because transitions of the electronic spin due to hyperfine interaction are strongly suppressed due to the large energy mismatch. If the dominating influence on the nuclear spin is the interaction with the electron, the quantisation axis in $m_s = \pm 1$ is entirely determined by the direction of the hyperfine field of the electron at the point of the nucleus. The resulting simplified interaction Hamiltonian is then

$$\mathcal{H}_{hf} = S_z \sum_\nu \alpha_{z\nu} I_\nu \equiv A S_z I_{z'}, \qquad (2.3)$$

where z' is the quantisation direction of the nuclear spin for $m_s = \pm 1$, and $\alpha_{\mu\nu}$ are the components of the hyperfine tensor (implicitly given in (2.2)). We can see that our qubit basis states are nuclear spin eigenstates that are defined by the splitting due to the effective magnetic field of the electronic spin.

We are particularly interested in nuclear spins for which the interaction strength exceeds the line width of the electronic spin transitions, which is typically on the order of ~ 100 kHz for our samples. In this case it is possible to perform electron spin rotations between $m_s = 0 \leftrightarrow \pm 1$ that are conditional on the nuclear spin state, allowing for the implementation of a controlled-NOT (CNOT) gate. Suitable nuclei are the one of the nitrogen host atom of the NV centre as well as those of close-by ¹³C atoms.

The nitrogen host

Each NV centre has a nitrogen atom with nuclear spin. Most commonly, with a natural abundance of 99.3%, the nitrogen is of the isotope ^{14}N with a nuclear spin of $I_N = 1$. There is also the possibility for a ^{15}N ($I = 1/2$), either by chance or engineering[29,30]. We will only discuss the ^{14}N case here because all experiments presented have been performed using naturally occurring NV centres with the ^{14}N isotope.

The system Hamiltonian for electronic and nitrogen nuclear spin in the orbital ground state can be written as

$$\mathcal{H}_{e,N} = DS_z^2 + \gamma_e \mathbf{B} \cdot \mathbf{S} - QI_{Nz}^2 + \gamma_N \mathbf{B} \cdot \mathbf{I}_N - A_{\parallel} S_z I_{Nz} - A_{\perp} \left(S_x I_{Nx} + S_y I_{Ny} \right), \qquad (2.4)$$

where S_i and I_{Ni} are the i-components of spin-1 operators for electron and nucleus, $\mathbf{S}$ and $\mathbf{I}_N$. Note that the quantisation axes (z-axes) for both electron and nitrogen spin are parallel. $\gamma_{e,N}$ are the electron and nitrogen nuclear spin gyromagnetic ratios, and Q is the quadrupolar splitting of the nitrogen nuclear spin. The hyperfine interaction can be divided into a parallel component $A_{\parallel}$ and a perpendicular component $A_{\perp}$. In the secular approximation,

$$\mathcal{H}_{e,N} = DS_z^2 + \gamma_e B_z S_z - QI_{Nz}^2 + \gamma_N B_z I_{Nz} - A_N S_z I_{Nz}, \qquad (2.5)$$

where we neglect all off-diagonal terms of the ^{14}N spin because its quantisation is fully governed by its quadrupolar splitting, independent of the electron spin projection. The resulting level structure is shown in Fig. 2.3.

We can, for instance, identify $m_I = -1 := |1\rangle_N$ and $m_I = 0 := |0\rangle_N$, leaving the third nuclear spin projection idle. The splitting of the two basis states is — up to an additional Zeeman splitting — determined by the sum of the quadrupolar splitting and the hyperfine interaction strength, $\omega_{N0} = Q + A_N = 2\pi \times 7.132\,\text{MHz}$, and qubit rotations can be performed using magnetic resonance pulses in the radio-frequency (RF) domain.

^{13}C spins

Besides the spin of the nitrogen host, the NV electronic spin also couples to ^{13}C nuclear spins ($I = 1/2$) in the environment. In non-purified diamond, the ^{13}C isotope occurs with a natural abundance of 1.1% within the otherwise spin-free ^{12}C material, and the resulting spin bath is to a large extent responsible for the dephasing of the electronic spin[31]. However, individual ^{13}C atoms that are located only a few lattice sites away from the NV centre experience a strong hyperfine interaction[32], and are usable as qubits.

For a strongly coupled carbon nuclear spin coupled to the NV centre electronic spin we can write the Hamiltonian in the orbital ground state as

$$\mathcal{H}_{e,N,C} = DS_z^2 + \gamma_e B_z S_z - QI_{Nz}^2 + \gamma_N B_z I_{Nz} - A_N S_z I_{Nz} + \gamma_C \mathbf{B} \cdot \mathbf{I}_C + A_C S_z I_{Cz'}, \qquad (2.6)$$

where we have again made the secular approximation. For small magnetic fields, the quantisation axis z' of the carbon spin in the $m_s = \pm 1$ manifold is determined by the hyperfine field
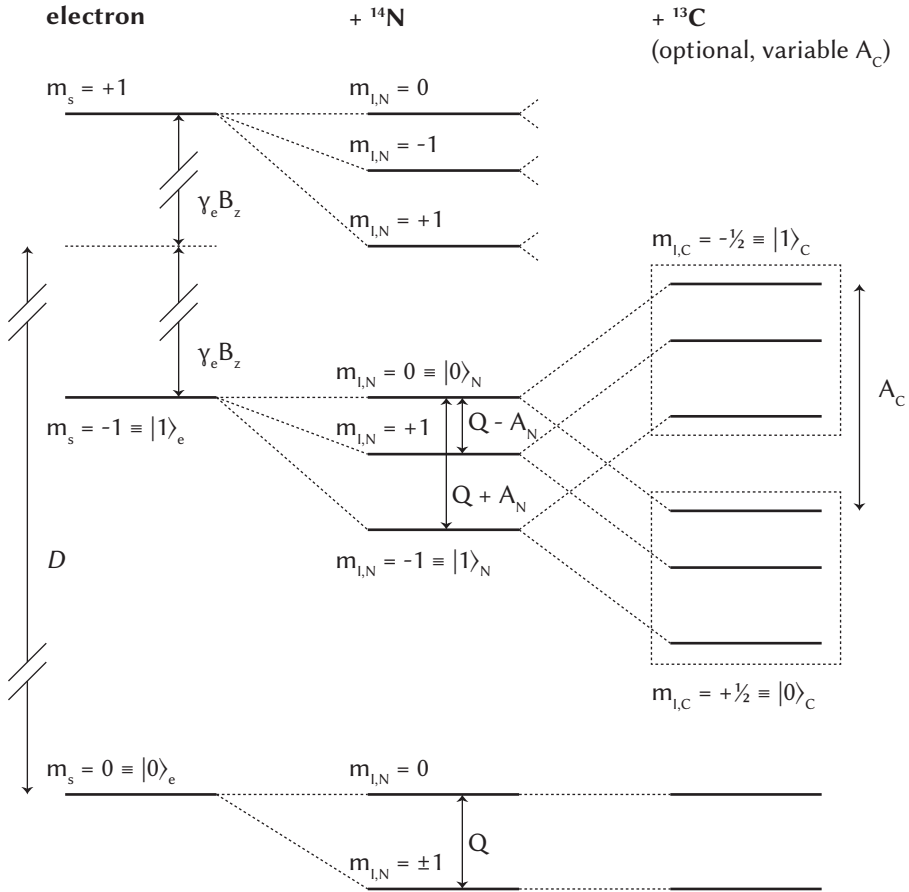
Figure 2.3 | Spin level structure in the orbital ground state. The electronic $m_s = 0$ state is separated from the $m_s = \pm 1$ levels by the zero-field splitting, $D = 2\pi \times 2.878\,\mathrm{GHz}$ (at low temperature). In presence of an external magnetic field the $m_s = \pm 1$ levels are split by $2\gamma_e B_z$, where B_z is the z-component of the field, and $\gamma_e = 2\pi \times 2.802\,\mathrm{MHz/G}$ is the electron gyromagnetic ratio. The $m_I = \pm 1$ states of the of the nitrogen spin ($I = 1$ for $^{14}\mathrm{N}$, the case depicted here) are lowered with respect to the $m_I = 0$ level due to a nuclear quadrupole splitting, with $Q = 2\pi \times 4.946\,\mathrm{MHz}$. Hyperfine interaction between the electronic and the $^{14}\mathrm{N}$ spin splits the $m_I = \pm 1$ levels for $m_s = \pm 1$, with a coupling constant $A_N = 2\pi \times 2.186\,\mathrm{MHz}$. We ignore the magnetic field splitting of the nuclear spin at this point. In the presence of a strongly coupled $^{13}\mathrm{C}$ nuclear spin ($I = 1/2$) the $m_s = \pm 1$ levels are further split by a coupling constant A_C that depends on the lattice site that the $^{13}\mathrm{C}$ atom occupies. A typical set of qubit basis states are indicated.

of the electron at the lattice site of the ^{13}C atom. Contrary to the spin-1 ^{14}N the carbon spin has no pre-determined quantisation for $m_s = 0$ — its quantisation axis is then determined by the alignment of the externally applied magnetic field. Therefore, unless the magnetic field is aligned with the effective hyperfine field at the location of the nucleus, the quantisation axes can be different for $m_s = 0$ and $m_s = \pm 1$. An illustration of the level diagram for one ^{13}C spin coupled to the NV is shown in Fig. 2.3.

We identify qubit basis states as $m_I = +1/2 \coloneqq |0\rangle_C$ and $m_I = -1/2 \coloneqq |1\rangle_C$. The splitting depends on the hyperfine interaction strength, and can range from tens of kHz for ^{13}C atoms a few sites away, up to more than 100 MHz for neighbour sites of the vacancy[24,32].

2.4 Remote entanglement via a photonic channel

The optical interface of the NV centre does not only allow to access the local register but also provides a route to connect remote registers by entanglement. In a measurement-based scheme[33–36] a combined detection of photons emitted from both emitters projects the spins into an entangled state[13,37,38]. These type of protocols are particularly well suited for the case of the NV centre as the fidelity of the entangled state is not directly effected by the success probability and is therefore robust against photon loss.

The general scheme of entanglement generation is shown in figure 2.4. First, both centres are caused to emit a photon that is entangled with the electronic spin[39–42]. The overall spin-photon state is then

$$|\psi\rangle = \frac{1}{2}\left[|0\rangle\,|\alpha\rangle + |1\rangle\,|\gamma\rangle\right], \tag{2.7}$$

where $|0\rangle$, $|1\rangle$ are two electronic spin states and $|\alpha\rangle$, $|\gamma\rangle$ are two orthogonal photonic states, that could be, for instance, different polarization-, frequency-, time-bin-, or number-states. Such entangled states can be created by using the spin-dependent optical transitions of the NV centre at low temperatures.

In order to create entanglement between the two spins, both photons are overlapped on a beamsplitter. The beamsplitter transforms a photon $|\alpha\rangle$ in the input mode according to[43]:

$$|\alpha\rangle_a \longrightarrow \frac{1}{\sqrt{2}}(|\alpha\rangle_1 + |\alpha\rangle_2), \qquad |\alpha\rangle_b \longrightarrow \frac{1}{\sqrt{2}}(|\alpha\rangle_1 - |\alpha\rangle_2), \tag{2.8}$$

where the indices a, b describe the two input modes and $1, 2$ the two output modes (Fig. 2.4b).
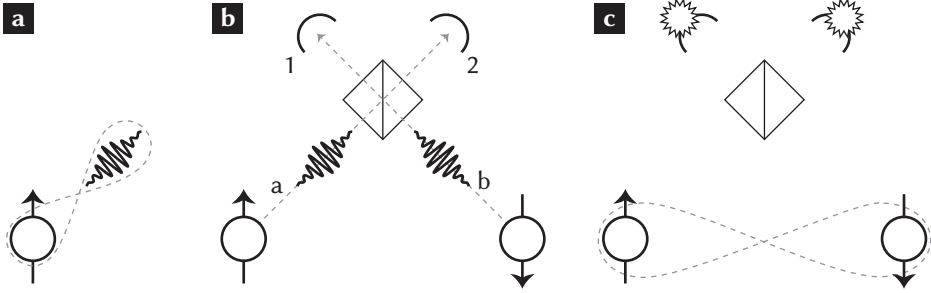
Figure 2.4 | Measurement-based creation of remote entanglement. a, Each spin is prepared in a state that is entangled with an emitted photon. **b,** The two photons are overlapped on a beamsplitter. If the photons are indistinguishable the beamsplitter erases the which-path information. **c,** Detection of certain photonic states projects the spins into an entangled state.

The full state of the two photons and two spins is

$$
\begin{aligned}
|\psi\rangle_a \otimes |\psi\rangle_b &= \frac{1}{\sqrt{2}}(|0\rangle_a |\alpha\rangle_a + |1\rangle_a |\gamma\rangle_a) \otimes \frac{1}{\sqrt{2}}(|0\rangle_b |\tilde{\alpha}\rangle_b + |1\rangle_b |\tilde{\gamma}\rangle_b) \\
&= \frac{1}{4}[|0\rangle_a (|\alpha\rangle_1 + |\alpha\rangle_2) + |1\rangle_a (|\gamma\rangle_1 + |\gamma\rangle_2) \\
&\quad \otimes |0\rangle_b (|\tilde{\alpha}\rangle_1 - |\tilde{\alpha}\rangle_2) + |1\rangle_b (|\tilde{\gamma}\rangle_1 - |\tilde{\gamma}\rangle_2)] \\
&= \frac{1}{4}[|00\rangle (|\alpha\tilde{\alpha}\rangle_1 - |\alpha\tilde{\alpha}\rangle_2 + |\tilde{\alpha}\rangle_1 |\alpha\rangle_2 - |\alpha\rangle_1 |\tilde{\alpha}\rangle_2) \\
&\quad + |11\rangle (|\gamma\tilde{\gamma}\rangle_1 - |\gamma\tilde{\gamma}\rangle_2 + |\tilde{\gamma}\rangle_1 |\gamma\rangle_2 - |\gamma\rangle_1 |\tilde{\gamma}\rangle_2) \\
&\quad + |01\rangle (|\alpha\tilde{\gamma}\rangle_1 - |\alpha\tilde{\gamma}\rangle_2 + |\tilde{\gamma}\rangle_1 |\alpha\rangle_2 - |\alpha\rangle_1 |\tilde{\gamma}\rangle_2) \\
&\quad + |10\rangle (|\tilde{\alpha}\gamma\rangle_1 - |\tilde{\alpha}\gamma\rangle_2 + |\tilde{\alpha}\rangle_1 |\gamma\rangle_2 - |\gamma\rangle_1 |\tilde{\alpha}\rangle_2)].
\end{aligned} \tag{2.9}
$$

For indistinguishable photons ($|\alpha\rangle = |\tilde{\alpha}\rangle$, $|\gamma\rangle = |\tilde{\gamma}\rangle$) terms such as $|\tilde{\alpha}\rangle_1 |\alpha\rangle_2 - |\alpha\rangle_1 |\tilde{\alpha}\rangle_2$ cancel. This effect is called two-photon quantum interference, or Hong-Ou-Mandel effect[44], and is essential for the success of the protocol. Then equation 2.9 becomes:

$$
\begin{aligned}
|\psi\rangle_a \otimes |\psi\rangle_b &= \frac{1}{4}[|00\rangle (|2\alpha\rangle_1 - |2\alpha\rangle_2) \\
&\quad + |11\rangle (|2\gamma\rangle_1 - |2\gamma\rangle_2) \\
&\quad + (|01\rangle + |10\rangle)(|\alpha\gamma\rangle_1 - |\alpha\gamma\rangle_2) \\
&\quad + (|01\rangle - |10\rangle)(|\gamma\rangle_1 |\alpha\rangle_2 - |\alpha\rangle_1 |\gamma\rangle_2)].
\end{aligned} \tag{2.10}
$$

Detecting a certain photonic state projects the two emitters into the corresponding spin state. Assume that $|\alpha\rangle$ and $|\gamma\rangle$ are two orthogonal polarization of the photon. Then the detection of one photon in each output port of the beamsplitter (figure 2.4 c) projects the two spins into the entangled Bell state $\Psi^- = 1/\sqrt{2}(|01\rangle - |10\rangle)$.

In chapter 8 we use such a measurement-based protocol to create entanglement between two NV centres that are separated by three metres. The photon states used in that experiment are number states, $|\alpha\rangle = |1\rangle_{\text{photon}}$ and $|\gamma\rangle = |0\rangle_{\text{photon}}$. With the detectors used states as $|2\alpha\rangle_1 = |2\rangle_{1,\text{photon}}$ and $|\alpha\rangle_1 |\gamma\rangle_2 = |1\rangle_{1,\text{photon}} |0\rangle_{2,\text{photon}}$ cannot be distinguished. Therefore, the spins are projected into a mixed state. This issue can be overcome with an adaptation of the protocol as suggested by Barret and Kok[36], consisting of two rounds of the protocol with a spin flip in between. Detection of exactly one photon in each round then projects the two spins into an entangled state (chapter 8).

2.5 Bibliography

[1] J. R. Maze *et al.* Properties of nitrogen-vacancy centers in diamond: the group theoretic approach. *New J. Phys.* **13**, 5025 (2011).

[2] M. W. Doherty, N. Manson, P. Delaney and L. C. L. Hollenberg. The negatively charged nitrogen-vacancy centre in diamond: the electronic solution. *New J. Phys.* **13**, 5019 (2011).

[3] F. Jelezko and J. Wrachtrup. Single defect centres in diamond: A review. *phys. stat. sol. (a)* **203**, 3207 (2006).

[4] M. W. Doherty *et al.* The nitrogen-vacancy colour centre in diamond. *Physics Reports* **528**, 1 (2013).

[5] V. Acosta and P. Hemmer. Nitrogen-vacancy centers: Physics and applications. *MRS Bull.* **38**, 127 (2013).

[6] L. Childress and R. Hanson. Diamond NV centers for quantum computing and quantum networks. *MRS Bull.* **38**, 134 (2013).

[7] L. T. Hall, D. A. Simpson and L. C. L. Hollenberg. Nanoscale sensing and imaging in biology using the nitrogen-vacancy center in diamond. *MRS Bull.* **38**, 162 (2013).

[8] S. Hong *et al.* Nanoscale magnetometry with NV centers in diamond. *MRS Bull.* **38**, 155 (2013).

[9] M. Lončar and A. Faraon. Quantum photonic networks in diamond. *MRS Bull.* **38**, 144 (2013).

[10] D. M. Toyli, L. C. Bassett, B. B. Buckley, G. Calusine and D. D. Awschalom. Engineering and quantum control of single spins in semiconductors. *MRS Bull.* **38**, 139 (2013).

[11] J. Wrachtrup, F. Jelezko, B. Grotz and L. McGuinness. Nitrogen-vacancy centers close to surfaces. *MRS Bull.* **38**, 149 (2013).

[12] F. Jelezko, T. Gaebel, I. Popa, A. Gruber and J. Wrachtrup. Observation of coherent oscillations in a single electron spin. *Phys. Rev. Lett.* **92**, 076401 (2004).

[13] H. Bernien *et al.* Heralded entanglement between solid-state qubits separated by three metres. *Nature* **497**, 86 (2013).

[14] N. Bar-Gill, L. M. Pham, A. Jarmola, D. Budker and R. L. Walsworth. Solid-state electronic spin coherence time approaching one second. *Nature Commun.* **4**, 1743 (2013).

[15] V. V. Dobrovitski, A. E. Feiguin, R. Hanson and D. D. Awschalom. Decay of Rabi oscillations by dipolar-coupled dynamical spin environments. *Phys. Rev. Lett.* **102**, 237601 (2009).

[16] P. Tamarat *et al.* Stark Shift Control of Single Optical Centers in Diamond. *Phys. Rev. Lett.* **97**, 83002 (2006).

[17] L. C. Bassett, F. J. Heremans, C. G. Yale, B. B. Buckley and D. D. Awschalom. Electrical Tuning of Single Nitrogen-Vacancy Center Optical Transitions Enhanced by Photoinduced Fields. *Phys. Rev. Lett.* **107**, 266403 (2011).

[18] M. Steger *et al.* Quantum Information Storage for over 180 s Using Donor Spins in a 28Si "Semiconductor Vacuum". *Science* **336**, 1280 (2012).

[19] P. C. Maurer *et al.* Room-Temperature Quantum Bit Memory Exceeding One Second. *Science* **336**, 1283 (2012).

[20] C. P. Slichter. *Principles of magnetic resonance.* Springer, New York, 3rd edition (1990).

[21] L. Vandersypen and I. Chuang. NMR techniques for quantum control and computation. *Rev. Mod. Phys.* **76**, 1037 (2005).

[22] F. Jelezko *et al.* Observation of Coherent Oscillation of a Single Nuclear Spin and Realization of a Two-Qubit Conditional Quantum Gate. *Phys. Rev. Lett.* **93**, 130501 (2004).

[23] M. V. G. Dutt *et al.* Quantum register based on individual electronic and nuclear spin qubits in diamond. *Science* **316**, 1312 (2007).

[24] P. Neumann *et al.* Multipartite Entanglement Among Single Spins in Diamond. *Science* **320**, 1326 (2008).

[25] P. Neumann *et al.* Single-Shot Readout of a Single Nuclear Spin. *Science* **329**, 542 (2010).

[26] L. Jiang *et al.* Repetitive readout of a single electronic spin via quantum logic with nuclear spin ancillae. *Science* **326**, 267 (2009).

[27] G. D. Fuchs, G. Burkard, P. V. Klimov and D. D. Awschalom. A quantum memory intrinsic to single nitrogen-vacancy centres in diamond. *Nature Phys.* **7**, 789 (2011).

[28] T. van der Sar *et al.* Decoherence-protected quantum gates for a hybrid solid-state spin register. *Nature* **484**, 82 (2012).

[29] D. M. Toyli, C. D. Weis, G. D. Fuchs, T. Schenkel and D. D. Awschalom. Chip-scale nanofabrication of single spins and spin arrays in diamond. *Nano Letters* **10**, 3168 (2010).

[30] K. Ohno *et al.* Engineering shallow spins in diamond with nitrogen delta-doping. *Appl. Phys. Lett.* **101**, 2413 (2012).

[31] J. R. Maze, J. M. Taylor and M. D. Lukin. Electron spin decoherence of single nitrogen-vacancy defects in diamond. *Physical Review B* **78**, 94303 (2008).

[32] B. Smeltzer, L. Childress and A. Gali. 13C hyperfine interactions in the nitrogen-vacancy centre in diamond. *New J. Phys.* **13**, 025021 (2011).

[33] C. Cabrillo, J. Cirac, P. Garcia-Fernandez and P. Zoller. Creation of entangled states of distant atoms by interference. *Phys. Rev. A* **59**, 1025 (1999).

[34] L.-M. Duan, M. D. Lukin, J. I. Cirac and P. Zoller. Long-distance quantum communication with atomic ensembles and linear optics. *Nature* **414**, 413 (2001).

[35] C. Simon and W. T. M. Irvine. Robust Long-Distance Entanglement and a Loophole-Free Bell Test with Ions and Photons. *Phys. Rev. Lett.* **91**, 110405 (2003).

[36] S. D. Barrett and P. Kok. Efficient high-fidelity quantum computation using matter qubits and linear optics. *Physical Review A* **71**, 60310 (2005).

[37] D. L. Moehring *et al.* Entanglement of single-atom quantum bits at a distance. *Nature* **449**, 68 (2007).

[38] J. Hofmann *et al.* Heralded Entanglement Between Widely Separated Atoms. *Science* **337**, 72 (2012).

[39] B. B. Blinov, D. L. Moehring, L.-M. Duan and C. Monroe. Observation of entanglement between a single trapped atom and a single photon. *Nature* **428**, 153 (2004).

[40] E. Togan *et al.* Quantum entanglement between an optical photon and a solid-state spin qubit. *Nature* **466**, 730 (2010).

[41] W. B. Gao, P. Fallahi, E. Togan, J. Miguel-Sanchez and A. Imamoglu. Observation of entanglement between a quantum dot spin and a single photon. *Nature* **491**, 426 (2013).

[42] K. De Greve *et al.* Quantum-dot spin-photon entanglement via frequency downconversion to telecom wavelength. *Nature* **491**, 421 (2013).

[43] T. Legero, T. Wilk, A. Kuhn and G. Rempe. Time-resolved two-photon quantum interference. *Applied Physics B Lasers and Optics* **77**, 797 (2003).

[44] C. K. Hong, Z. Y. Ou and L. Mandel. Measurement of subpicosecond time intervals between two photons by interference. *Phys. Rev. Lett.* **59**, 2044 (1987).

Experimental methods

H. Bernien & W. Pfaff

In this chapter we introduce the experimental techniques that allow us to employ the NV centre as a building block for quantum registers and networks. We first show how we can optically address and characterize single NVs (chapter 3.1). The fabrication of NV centre devices that allow for high collection efficiency of the emitted photons, spin manipulation and tuning of the optical transition frequencies is described in chapter 3.2. We then discuss how we can pre-select during an experiment on the correct charge-state of the NV centre and on the optical transitions being on resonance with the laser frequencies (chapter 3.3). We conclude with a technical description of the experimental setup used (chapter 3.4).

3.1   Addressing single NV centres

For the experiments presented in the following chapters we employ single NV centres in bulk diamond, cooled to liquid helium temperatures. We first locate and pre-select centres of interest in a simpler setup at room-temperature, and subsequently fabricate structures for enhancing the collection efficiency, tuning optical resonances, and manipulating spins.

Samples

We use naturally occurring NV centres in high purity type IIa chemical-vapor deposition grown diamond with either a ⟨100⟩ crystal orientation or a ⟨111⟩ crystal orientation that is obtained by cleaving a ⟨100⟩ substrate. The latter case has the advantage that NV centres with their axis perpendicular to the surface plane can be selected. For these centres the dipoles belonging to the E_x- and E_y-transition lie in the surface plane. The diamonds are supplied by *Element 6*.

Localising NV centres

Using confocal microscopy, Gruber *et al.* were able to detect single NV centres for the first time in 1997[1]. To date this technique remains the standard tool for addressing single NV centres optically. We use a home-built confocal microscope at room temperature for basic characterisation. To find NVs we focus the beam of a green laser (532 nm) onto the sample using a microscope objective with high numerical aperture (typically, $NA = 0.95$). The same objective captures the fluorescence from the sample. A dichroic mirror separates the red-shifted phonon side-band emission from the excitation beam into a detection path (Fig. 3.1a).

By scanning the sample in all three dimensions using piezo-electric positioners and monitoring the position-dependent fluorescence via an avalanche photo diode (APD) we are able to localise emitters within the sample (Fig. 3.1b). We test whether such a candidate is indeed an NV centre: The spectrum of the NV emission exhibits a characteristic zero-phonon line (ZPL) at wavelength $\lambda \approx 637$ nm and a dominant red-shifted phonon side-band (PSB) which can be recognised easily (Fig. 3.1c). We can see whether the emission detected comes from a single NV centre (or more general, from a single-photon emitter) by measuring the second-order autocorrelation function $g^2(\tau)$ using a Hanbury Brown-Twiss configuration[4]. By directing the emission onto a 50:50 beamsplitter with an APD located at each output port we can record two-photon coincidences on the APDs as a function of the delay τ between the two events. This corresponds, up to normalisation, to $g^2(\tau)$ (Fig. 3.1d). A single emitter shows $g^2(0) < 1/2$.
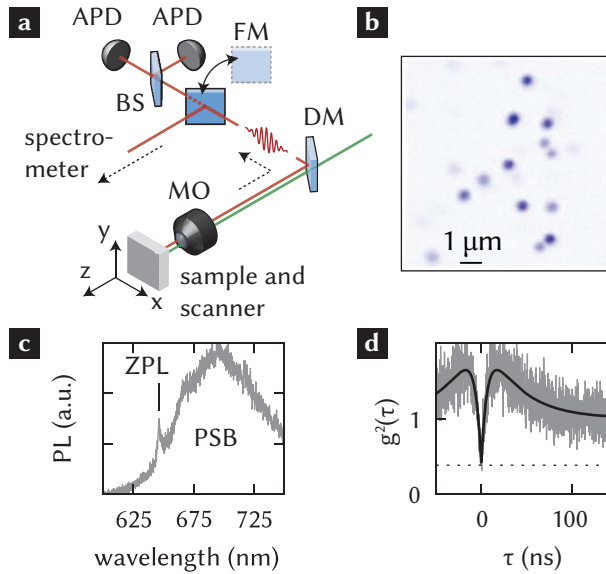
Figure 3.1 | Identifying single NV centres. a, Setup for sample characterisation. A microscope objective (MO; *Olympus MPlanApo50x*) focuses the green excitation laser (*Coherent Compass 315M*, frequency doubled Nd:YAG) onto the sample, mounted on a piezo scanning stage (*Physik Instrumente*). A dichroic mirror (DM; *Semrock*) separates the fluorescence spectrally into the detection path. Via a mechanically switchable mirror (FM) the emission is guided either to a spectrometer (*Princeton Instruments Acton*) or to a beam splitter (BS) followed by two APDs (*Perkin Elmer SPCM-AQR-14-FC*) in HBT configuration. The signals of the APDs are recorded by a time-tagging module (*FastComTec P7889*). **b,** Confocal map of a typical sample. The colour map indicates fluorescence level, where blue is high intensity. The high-intensity spots correspond to emission coming from single NV centres. (Figure adapted from [2].) **c,** Spectrum of the emission of a typical NV centre. The zero phonon line is clearly visible at $\lambda = 637$ nm. **d,** Second-order autocorrelation function. Taking into account background luminescence (dotted line), the anti-bunching dip at $\tau = 0$ reaches a value close to 0. The solid line is a fit to a three-level model taking into account relaxation via the singlet-levels [3].

3.2   Fabrication of NV centre devices

One of the main limitations that are encountered when performing optical measurements on single NV centres in bulk diamond is the low collection efficiency of the emitted photons. A large fraction of the 'lost' photons is due to the mismatch of the refractive indices between diamond ($n_\mathrm{diamond} \approx 2.4$) and air/vacuum (Fig. 3.2a). For angles

$$\theta > \arcsin(1/n_\mathrm{diamond}) \approx 24.6°$$

total internal reflection occurs. Furthermore, due to refraction at the interface even for angles $\theta < 24.6°$ the emission is distributed over a large range of angles which are not all collected by the numerical aperture of the objective. These problems can be overcome by using solid immersion lenses (SILs)[5–7]. In the configuration shown in figure 3.2b the NV centre is located in the centre of a half spherical lens. In this situation the emission is perpendicular to the air-diamond interface and no total internal reflection and refraction occurs.

In order to deterministically fabricate a solid immersion lens (SIL) around a specific NV centre we first fabricate a 200 nm thick gold marker grid defining a coordinate system onto the diamond surface via electron beam lithography. These markers are both visible in the focused ion beam system (FIB, *FEI Strata DB 235*), which is used to mill the SILs (Fig. 3.3a), as well as in the confocal microscope setup, in which we determine the relative positions of the NV centres (Fig. 3.3b). After locating the NV centres we use a 30 kV gallium ion beam to mill the lenses (Fig. 3.3c). The desired lens profile is approximated by milling concentric rings of varying diameters. The size of the lens is adjusted to fit the depth of the NV centre, which is selected within a range of $5-15\,\mu$m underneath the diamond surface in order to keep the milling time reasonable (0.5–4 hours per lens). After fabricating the lenses we
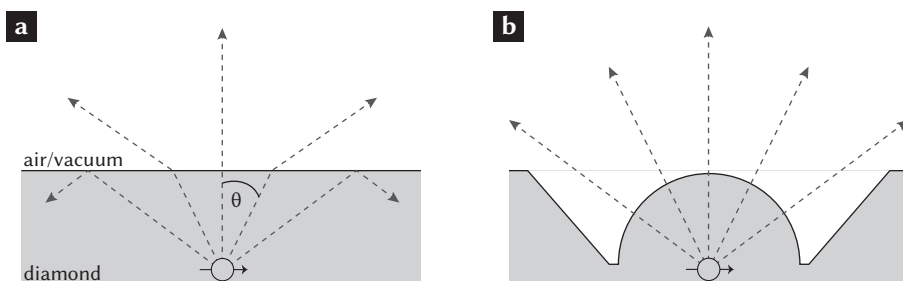
Figure 3.2 | Working principle of a solid immersion lens. a, For an emitter in bulk diamond total internal reflection and refraction occurs at the interface which limit the collection efficiency. **b,** In a geometry where the NV centre is placed in a half sphere, the emission is perpendicular to the surface and the collection efficiency is enhanced.
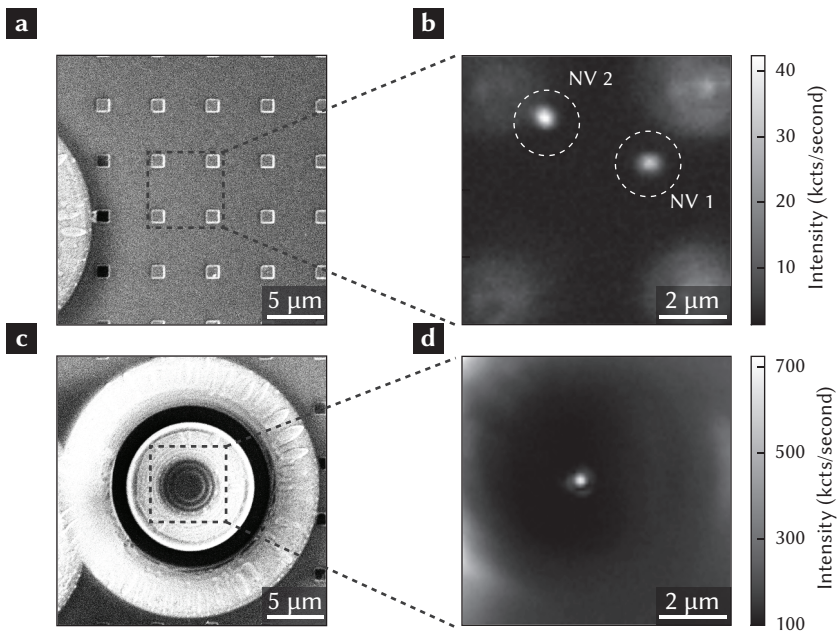
Figure 3.3 | Deterministic fabrication of SILs around preselected NVs. a, A coordinate system is fabricated on the diamond surface that is both visible in the focused ion beam (FIB) system and the confocal setup **b** (kcts = 1000 counts). **c,** The position of a selected NV centre are determined from the confocal image and a lens is milled in the FIB. **d,** After subsequent wet and dry etching the fluorescence from the NV inside the SIL can be detected with enhanced collection efficiency. (Confocal scans **b** and **d** are representative scans of similar devices.)
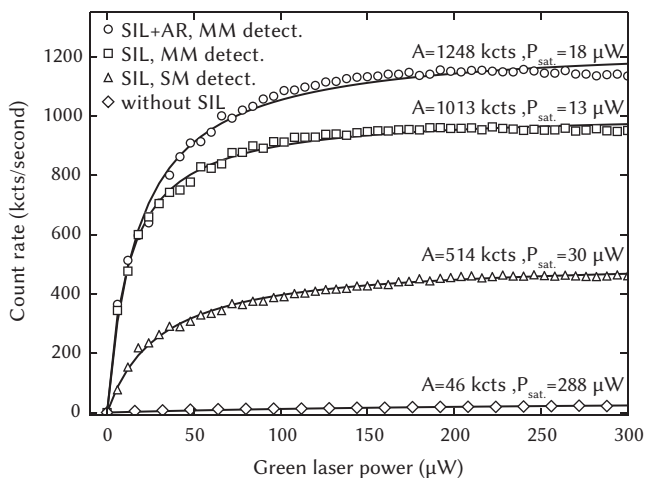
Figure 3.4 | Saturation measurements with and without SIL. Fluorescence count rates in dependence of off-resonant green excitation power (kcts = 1000 counts). Solid lines are fits to $A \cdot x/(x + P_{\text{sat.}})$. For single mode detection (SM detect.) the emission is collected with a single mode fiber which is attached to a fiber coupled APD. For multimode detection (MM detect.) a fiber with $60\,\mu$m core diameter is used. The use of a SIL increases the collection efficiency by about one order of magnitude and allows for multimode detection which additionally enhances the detected fluorescence. An anti-reflection coating further increases the count rates. The mismatch between the fit and the data for high count rates is likely due to the dead time of the APD and counting module which leads to an underestimation of the actual count rate. Data with SIL is taken on the same NV centre in a $\langle 111 \rangle$ orientated diamond, Data without SIL is recorded on a different NV centre in a $\langle 100 \rangle$ orientated diamond.

clean the sample for 30 minutes in a boiling mixture of equal parts of perchloric, sulfuric and nitric acid. This step removes material redeposited during the milling. During the FIB process gallium atoms are implanted into the diamond which form a conductive layer of about 30 nm thickness on the surface[8]. This layer is removed by reactive-ion etching in an oxygen-plasma. After these cleaning steps we can image the NV inside the SIL with enhanced collection efficiency (Fig. 3.3d).

Figure 3.4 shows the saturation behavior of an NV centre with and an NV centre without solid immersion lens. For the case of single mode detection the collection efficiency is increased by about one order of magnitude. Furthermore, by using SILs the excitation becomes more efficient, leading to lower saturation powers $P_{\text{sat.}}$. Owing to the high magnification of the lens, a low background count rate allows us to use multimode detection, which enhances our count rates by a factor of about two over single mode detection.
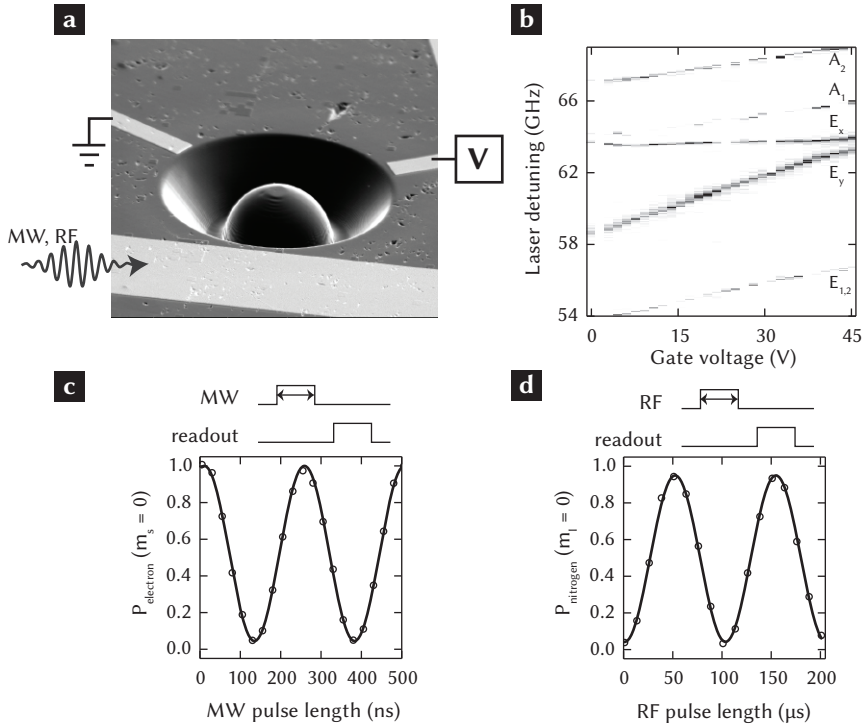
Figure 3.5 | NV centre device a, Scanning electron microscope image of a typical device after fabrication. Next to the lens are a gold strip line for applying magnetic resonance pulses ('RF' and 'MW') and gold gates for applying DC voltages. **b,** Applying a voltage to the gates shifts the optical resonances of the NV centre by the DC Stark effect. Two separate NV centres can be tuned on resonance by this method (Frequency is given relative to 470.4 THz). **c,** The electronic spin can be manipulated on ns-timescales by sending microwaves at 2.88 GHz through the strip line. **d,** Magnetic resonance pulses in the MHz range through the same strip line can rotate close-by nuclear spins on a μs-timescale. Shown are Rabi oscillations of the nitrogen nuclear spin associated with the NV centre.

Even when using SILs, the large mismatch of the refractive indices between diamond and air/vacuum still reduces the collection efficiency due to reflections. Under normal incidence the reflection coefficient is equal to 17 %. To decrease reflections we fabricate a single-layer anti-reflection coating (aluminum oxide) on top of the diamond surface[9] resulting in a further enhanced collection efficiency (top curve Fig. 6.8).

Further functionality is added to the device by fabricating a 200 nm thick gold microwave strip line and electronic gates around the lens via electron beam lithography (Fig. 3.5a). A

voltage applied to the gates shifts the optical transition frequencies via the DC Stark effect (Fig. 3.5b). This method allows us to bring two separate NV centres on resonance in order to produce indistinguishable photons (chapters 7, 8 and 9). The microwave strip line can be used to manipulate both the electronic spin (Fig. 3.5c) and nuclear spins (Fig. 3.5d).

3.3 Charge-state control and resonance verification

Our experiments require that before each run of an experimental sequence the NV centre is in its negative charge state, as well as that the lasers for optical control and readout are on resonance with the respective transitions. Optical excitation in the zero-phonon line, however, leads to ionisation[2] of the NV centre from NV^- to NV^0. The charge state can be re-pumped to NV^- by illumination with green laser-light (typically at a wavelength of $\lambda = 532$ nm), which in turn causes spectral diffusion of the zero-phonon line resonance frequencies due to changes of the local charge environment[2].

We ensure the correct conditions before each run of an experimental sequence using a preselection method as follows (Fig. 3.6). Before the experiment is started, we apply simultaneous laser pulses on both readout and spin-pumping transition, and monitor the fluorescence. The number of photons detected during this excitation interval is much higher if both lasers are on resonance compared to the case where either (or both) of the lasers are not. Also, the detection of any photons shows that the NV is with very high probability in its negative charge state. By imposing a suitable threshold for the number of photons detected we are able to preselect on the correct charge state and on-resonance configuration.
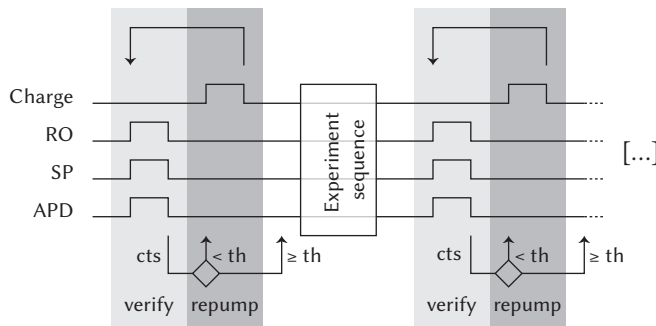
Figure 3.6 | Charge and resonance verification. Before each run of the experimental sequence we check whether the lasers are on resonance by exciting both readout (RO) and spin-pumping (SP) transitions and monitoring fluorescence counts on the APD. In case the counts detected surpass a pre-set threshold, we proceed with the experiment, otherwise we perform a charge-reset (Charge) until the resonance condition is met.

If the threshold is passed, the experiment is started. If not, we 'reset' the state probabilistically with a green laser pulse: In case the NV was in the neutral charge state, illumination with green laser light enables re-capturing an electron from the environment. Furthermore, due to spectral diffusion the resonance frequencies can shift. By repeating the probe/reset cycle, the NV can be brought into a useable configuration again.

An alternative method for ionising the charge state from NV^0 to NV^- is resonant excitation in the NV^0 zero-phonon line at a wavelength of $\lambda \approx 575$ nm. Via a two-photon absorption process the NV^- state can be restored [10]. This resonant excitation method requires less optical power (typically 2–3 orders of magnitude) and the optical wavelength employed causes less charge fluctuations in the environment [11], and is therefore beneficial to the spectral stability of the resonances compared to charge reset with green excitation [10].

3.4 Experimental setup

Experiments are performed using two home-built low temperature confocal microscopes featuring lasers for off-resonant and resonant excitation, cryogenic piezoelectric positioners and high-efficiency/low-background fluorescence detection paths (Fig. 3.7). One of the cryostats used is a flow cryostat operated at a temperature of 8–9 K (*Janis ST-500*) and the other one is a custom-built bath cryostat operating at liquid helium temperature (*CryoVac*). Both setups are equipped with almost-identical measurement hardware (see Fig. 3.7 for details).

Experiment control

The hardware used for experiments on a single setup and communication between the devices is schematically shown in Fig. 3.8. The experimental protocols discussed in this thesis involve conditional logic, for instance for probabilistic charge and resonance preparation and probabilistic preparation of nuclear spin states by projective measurement. We therefore implement the experiment control loops on a fast, programmable controller with DAC- and counter-modules (*ADwin Gold II* or *ADwin Pro*) that is able to trigger experiment sequences on other hardware. Specific realisations of such conditional protocols are discussed in the context of the respective experiments.

Setup for remote entanglement

For the generation of remote entanglement we combine two independent setups as schematically shown in Fig. 3.9. Both setups are capable of preparing charge and resonances autonomously using their single-setup capabilities (figures 3.7, 3.8), while the entanglement generation is performed in a synchronised protocol that is coordinated by the ADwin controller and AWG of one of the two setups.
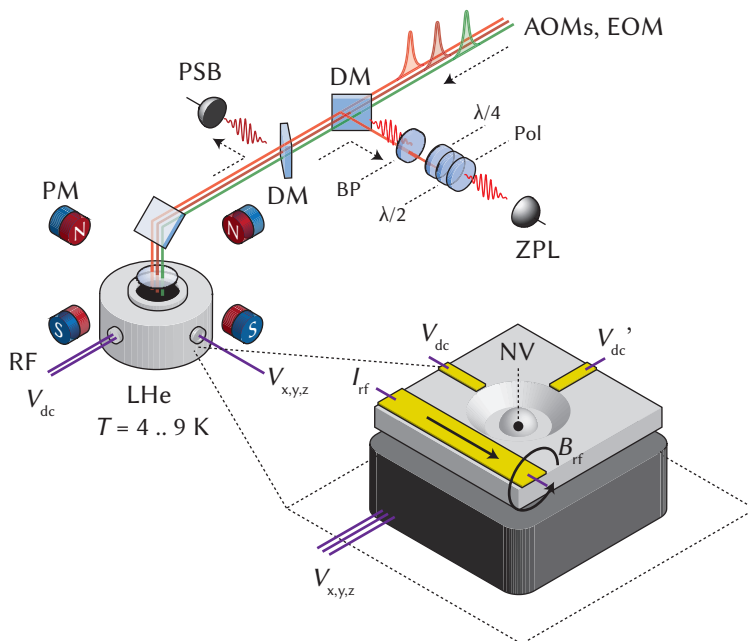
Figure 3.7 | Low temperature confocal microscope. Samples are mounted onto XYZ stepper/scanner piezo stacks (*Attocube*) and located inside a cryostat (see main text). The excitation light is focussed onto the sample using a microscope objective located inside the cryostat. The same objective collects the emission. Each cryostat is equipped with enough electrical lines to control the positioners ($V_{x,y,z}$), apply magnetic resonance pulses (RF), apply DC voltages to the gates (V_{dc}). Static magnetic fields are applied using permanent magnets (PM) arranged on the outside of the cryostat. Off-resonant green excitation is provided by 532 nm lasers (*Spectra Physics Millenia Pro* or *Laser 2000 Cobalt Samba*). Resonant excitation is performed with tuneable 637 nm lasers (*Newfocus Velocity* and *Sirah Matisse DS*), with pulses generated using acousto-optic modulators in double-pass configuration (AOM; *Crystal Technologies*). For fast excitation pulses the output of the *Matisse* is fed sequentially through an AOM and electro-optic modulator (EOM; *Jenoptik*). The photon emission of the NV is split into a ZPL part and an off-resonant PSB part by a dichroic long-pass filter (DM; *Semrock LPD01-633RS*). The PSB emission is detected by an avalanche photo diode (APD; *Perkin-Elmer SPCM* or *PicoQuant Tau-SPAD*). The ZPL emission is further filtered by a second dichroic filter (to remove green excitation light) and a tuneable band pass filter (BP; *Semrock TBP-700B*). Resonant excitation light is filtered by cross-polarisation rejection using half- and quarter-wave plates and a polariser ($\lambda/2$, $\lambda/4$, Pol), and then detected by an APD (*PicoQuant Tau-SPAD*).

Figure 3.8 | Single-setup control scheme. A PC programs the control loop on a integrated micro-controller (*ADwin*) and sequences on an arbitrary waveform generator (AWG; *Tektronix AWG 5014*). Sequences on the AWG are triggered from the ADwin, and the AWG notifies the ADwin when sequences are completed. Both ADwin and AWG generate laser pulses for charge re-pumping (Pump), electron spin pumping (SP), and electron spin readout (RO) via AOMs. The AWG also generates fast optical excitation pulses for coherent optical control on the readout transition via an EOM. Laser frequencies are monitored with a wave meter (*Highfinesse WS7* or *WSU*), and controlled using DAC modules on the frequency modulation inputs of the lasers (*Labjack*, or built-in for *Sirah Matisse* laser). MW pulses are generated by a vector source (*Rohde & Schwarz SMB100A*). The AWG controls frequency and timing of these pulses via IQ (I,Q) and pulse modulation (M). RF pulses are synthesised directly in the AWG. Spin manipulation signals are amplified (*Amplifier Research 20S1G4* or *40S1G4* for MW, and *AR 30W 1000B* or *Electronic & Innovation 240L* for RF) and combined (*Minicircuits*) before feeding to the sample. Gate voltages to the sample are controlled via a DAC module (*Labjack* or *ADwin*) and amplified by a home-built DC amplifier. APD signals are registered by both the counting module of the ADwin and a fast time-tagging module (PQ; *PicoQuant PicoHarp 300* or *HydraHarp 400*).

Figure 3.9 | Control scheme for remote entanglement. The ADwin of setup A runs a master control loop for synchronising the operations on both setups during the entanglement generation — only charge and resonance preparation is run on each setup autonomously. For the detection of entanglement events the zero-phonon line counts at the output ports of a fibre-coupled beam splitter (*Evanescent Optics*) are monitored by a programmable logic device (CPLD; *Altera Max V* development kit) that detects the photon signature for successful entanglement events and triggers the experimental sequence that is to follow entanglement generation. All photon events and CPLD output are recorded by a fast time-tagging module (*PicoQuant HydraHarp 400*) for data analysis and filtering of data. Synchronisation events for both CPLD and HydraHarp are provided by an AWG.

3.5 Bibliography

[1] A. Gruber *et al.* Scanning Confocal Optical Microscopy and Magnetic Resonance on Single Defect Centers. *Science* **276**, 2012 (1997).

[2] L. Robledo, H. Bernien, I. van Weperen and R. Hanson. Control and Coherence of the Optical Transition of Single Nitrogen Vacancy Centers in Diamond. *Physical Review Letters* **105**, 177403 (2010).

[3] C. Kurtsiefer, S. Mayer, P. Zarda and H. Weinfurter. Stable Solid-State Source of Single Photons. *Physical Review Letters* **85**, 290 (2000).

[4] M. Fox. *Quantum Optics.* Oxford University Press (2006).

[5] J. P. Hadden *et al.* Strongly enhanced photon collection from diamond defect centers under microfabricated integrated solid immersion lenses. *Applied Physics Letters* **97**, 241901 (2010).

[6] L. Marseglia *et al.* Nanofabricated solid immersion lenses registered to single emitters in diamond. *Applied Physics Letters* **98**, 133107 (2011).

[7] L. Robledo *et al.* High-fidelity projective read-out of a solid-state spin quantum register. *Nature* **477**, 574 (2011).

[8] W. R. McKenzie, M. Z. Quadir, M. H. Gass and P. R. Munroe. Focused Ion beam implantation of diamond. *Diamond and Related Materials* **20**, 1125 (2011).

[9] T. K. Yeung, D. Le Sage, L. M. Pham, P. L. Stanwix and R. L. Walsworth. Anti-reflection coating for nitrogen-vacancy optical measurements in diamond. *Applied Physics Letters* **100**, 251111 (2012).

[10] P. Siyushev *et al.* Optically Controlled Switching of the Charge State of a Single Nitrogen-Vacancy Center in Diamond at Cryogenic Temperatures. *Physical Review Letters* **110**, 167402 (2013).

[11] J. Wolters, N. Sadzak, A. W. Schell, T. Schröder and O. Benson. Measurement of the Ultrafast Spectral Diffusion of the Optical Transition of Nitrogen Vacancy Centers in Nano-Size Diamond Using Correlation Interferometry. *Physical Review Letters* **110**, 027401 (2013).

CONTROL AND COHERENCE OF THE OPTICAL TRANSITION OF SINGLE DEFECT CENTERS IN DIAMOND

L. Robledo, H. Bernien, I. van Weperen, and R. Hanson

We demonstrate coherent control of the optical transition of single Nitrogen-Vacancy defect centers in diamond. On applying short resonant laser pulses, we observe optical Rabi oscillations with a half-period as short as 1 nanosecond, an order of magnitude shorter than the spontaneous emission time. By studying the decay of Rabi oscillations, we find that the decoherence is dominated by laser-induced spectral jumps. By using a low-power probe pulse as a detuning sensor and applying post-selection, we demonstrate that spectral diffusion can be overcome in this system to generate coherent photons.

4.1 Introduction

Quantum control of light and matter is an outstanding challenge in modern science. Full control over both the spin state and the optical transition of a quantum system enables exciting applications such as spin-based quantum information processing and long-distance quantum teleportation of a spin state[1]. The basic operation underlying these applications, generation of non-local spin-spin entanglement, was recently demonstrated using individual trapped ions[2]. It is highly desirable to achieve the same level of control in solid-state systems as these may be easier to scale and promise higher integration density.

Candidate systems are required to have an electronic ground state with non-zero spin as well as a strong optical transition. Furthermore, coherent control over this transition is essential, as well as indistinguishability of the emitted photons[3]. In this context, several promising systems are studied extensively. Two-photon interference from independent sources was demonstrated for donor-bound excitons in semiconductors[4] and for quantum dots[5]. Optical Rabi oscillations have been observed in quantum dots[6] and Nitrogen-Vacancy (NV) color centers in diamond[7]. A major challenge for these solid-state systems is the inhomogeneous broadening of the optical transitions caused by fluctuations in the solid-state environment[8–10]. These fluctuations not only degrade the fidelity of optical control, but also reduce the visibility in two-photon interference experiments. Since this interference is crucial for generating non-local entanglement, imperfect contrast directly translates into a reduced entanglement fidelity.

Here, we demonstrate coherent optical control over the orbital state of single NV centers in diamond. Using short resonant laser pulses, we induce coherent oscillations of the optical transition. The decay of these oscillations yields important information on the transition's coherence[11]. We study the dependence of the coherence time on the involved laser fields. In particular, we find that spectral jumps, induced by an inevitable repump process, appear to degrade the fidelity of optical control. A scheme where the control is preceded by a detuning-sensitive stage is implemented. We show that post-selection based on the detuning sensing can be used to circumvent the degrading effect of spectral jumps on two-photon interference.

4.2 Experimental setting

The NV center consists of a single substitutional nitrogen atom in the diamond lattice, located next to a vacancy. We use a type IIa CVD-grown bulk diamond sample from Element Six ($\langle 100 \rangle$ oriented), containing a concentration low enough to detect individual negatively charged NV^- centers (Fig. 4.1a).

The experiments are performed in a scanning confocal microscope using a flow cryostat at a temperature of $T = 8$ K. NV center fluorescence is excited either off-resonant using a $\lambda = 532$ nm (green) laser or on resonance by means of a narrow-band tunable $\lambda = 637$ nm (red) diode laser. For continuous resonant excitation, the laser frequency is actively stabilized

using a high-resolution wavemeter. An electro-optical modulator (EOM) with risetime of 1.3 ns allows us to apply short resonant pulses. The green laser is sent through an acousto-optical modulator with a risetime of 4 ns. A dichroic mirror and additional longpass filters reject the excitation laser, so that only emission into the phonon sidebands (> 660 nm) is detected by an avalanche photodiode (APD) in the single-photon counting regime.

4.3 Photoluminescence excitation measurements

Excitation spectra are obtained by sweeping the excitation frequency across the NV center resonance and recording the red-shifted phonon-sideband emission. A spin triplet ground state with sublevels ($S_{x,y,z}$) and orbital A_2 symmetry, coupled to an excited state consisting of a spin triplet with sublevels ($S_{x,y,z}$) and orbital doublet with sublevels ($E_{x,y}$) gives rise to six resonances[12]. However, in general strong spin-flip transitions lead to fast spin polarization, preventing most resonances to be directly observed in single-laser excitation experiments[13]. Here, we show results from NV centers in the high strain regime ($\delta_{str} \approx 40$ GHz) where we excite the cycling (S_z, A_2) $\leftrightarrow$ (S_z, E_x) transition[13]. This transition has a very low probability for spin-flips. After a spin-flip the same laser field can excite the (S_x, A_2) $\leftrightarrow$ (S_x, E_x) resonance detuned by ≈ 200 MHz which suffers from strong spin polarization back into the S_z state[12]. Furthermore, the effect of hyperfine interaction can be neglected at the timescale of our experiment[14]. In conclusion this transition represents a good approximation to a 2-level system.

Continuous resonant excitation quickly bleaches NV emission, which can be recovered by off-resonant green excitation. We measure the fluorescence decay rate as function of resonant laser power by applying a pulse sequence that alternates a 10 μs green pulse and 200 ms resonant excitation. We find that the fluorescence during the resonant pulse decays exponentially at a rate proportional to the driving power, provided the excitation power saturates the NV transition (Fig. 4.1b). The same decay is observed with and without simultaneous MW excitation at 2.88 GHz, eliminating spin polarization as possible explanation. Excitation at $\lambda = 637$ nm but detuned from the exact resonance does not bleach the NV center. These results indicate that photo-ionization of the center out of the excited state is the origin of the observed decay. Off-resonant (green) excitation can excite charge impurities in the environment of the NV center (e.g. substitutional Nitrogen[15]) which can bring the NV center back to the negative charge state. This mechanism is intrinsic to the NV center, and explains the need for off-resonant repumping whenever driving NV centers resonantly.

Fig. 4.1c shows a series of resonant excitation scans. Between each scan, a green pulse was applied to prepare the NV center in the negative charge state and initialize the spin into the S_z state[12]. Large spectral jumps from scan to scan and occasional photoionization can be observed. In absence of the green pulse, spectral jumps remain below our experimental resolution (however the probability of ionization increases). This observation is consistent with the assumption that the green laser changes the local charge environment, leading to a shift of the resonance frequency via the DC Stark effect. The distribution of spectral jumps
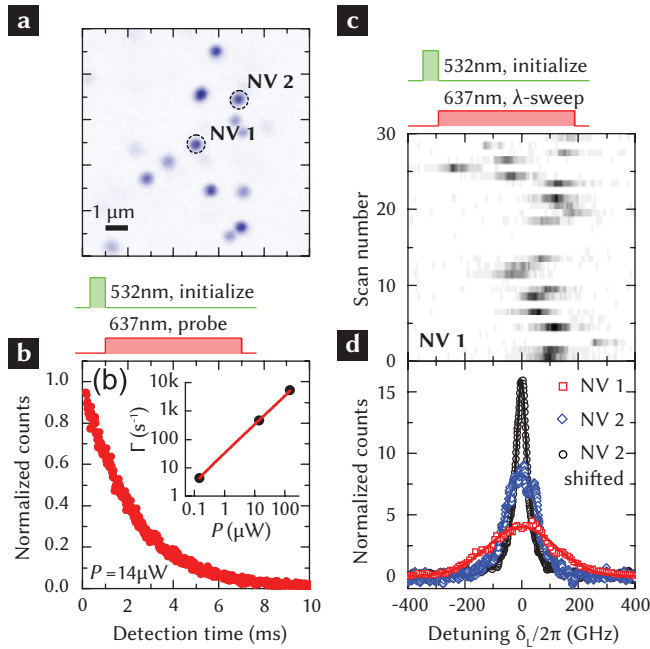
Figure 4.1 | Resonant excitation of single NV centers. a, Confocal fluorescence image of individual NV centers. **b,** Resonant excitation leads to exponential decay of fluorescence due to photo-ionization. Inset: Ionization rate Γ as function of power of the resonant excitation laser. **c,** Series of resonance scans. Green repump pulses applied in between scans to re-charge the NV center induce spectral jumps. **d,** Sum of individual excitation scans yields frequency distribution of spectral jumps for NV1 and NV2. In comparison, for NV2 individual scans have been shifted to coincide in center frequency and then summed, to obtain the intrinsic linewidth. Data is normalized to the area under the curve.

is thus dominated by the concentration of charge impurities in a center's direct environment. We observe large differences from center to center: In Fig. 4.1d, we compare the range of jumps for two centers. Spectral jumps of NV1 occur over a twice as large range as those of NV2, suggesting a higher concentration of nearby charge impurities. Summing individual scans while compensating for the spectral jumps reveals the Lorentzian-shaped absorption line in absence of green excitation. We find an intrinsic linewidth of 46 ± 2 MHz for both NV1 (data not shown) and NV2, presumably limited by interaction with the phonon bath at $T = 8\,\text{K}$[16].

Figure 4.2 | Optical Rabi oscillations - power dependence. a, Rabi oscillations for $P = 38\,\mu W$, $P = 19\,\mu W$ and $P = 4.7\,\mu W$. The lowest dataset indicates the shape of the excitation pulse. **b,** Rabi frequency plotted versus square root of excitation power.

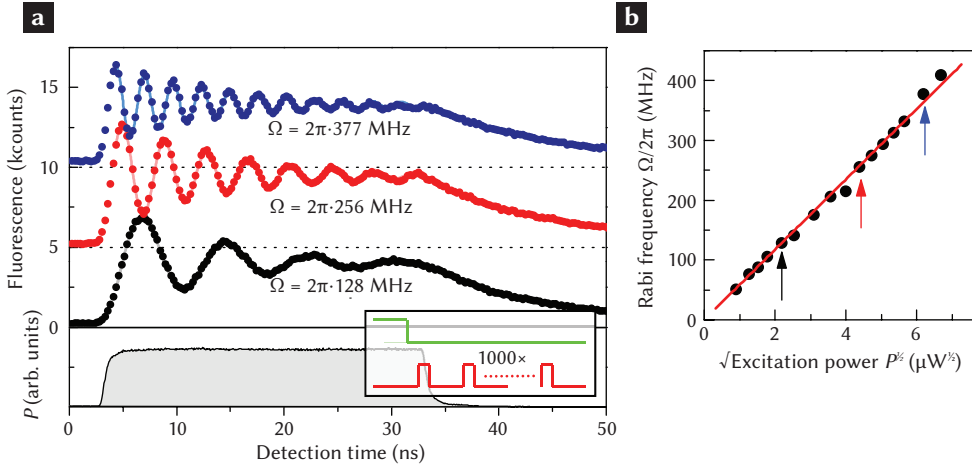## 4.4 Optical Rabi oscillations

In order to achieve coherent control, we apply resonant pulses. The sequence consists of a $10\,\mu s$ green pulse to initialize the NV^- charge and spin state, followed by 1000 repetitions of a 30 ns resonant laser pulse and a 70 ns off-time to allow the NV center to relax to its ground state before the next excitation cycle starts. We use a time-resolved single-photon counter to histogram the photon detection time relative to the start of the resonant laser pulse with a bin-size of $\Delta t_{bin} = 256\,ps$. To build up statistics we sum over typically 10^9 pulses. The number of counts during a time-bin is then proportional to the probability to occupy the excited state [17].

During a resonant laser pulse, we observe coherent oscillations between the NV orbital states (Fig. 4.2a). On resonance, the oscillation frequency is given by $\Omega_0 = \vec{\mu} \cdot \vec{E}/\hbar$, with $\vec{\mu}$ denoting the NV zero-phonon-line dipole moment and $\vec{E}$ the electric field vector. The resulting square root dependence of oscillation frequency on excitation power is clearly observed (Fig. 4.2b). For the largest applied driving power, we can resolve > 10 oscillations. The obtained Rabi frequency of $\Omega = 2\pi \cdot 410\,MHz$ corresponds to a π-pulse in only $t_\pi = 1.2\,ns$.

The oscillations are damped due to spontaneous emission and additional dephasing, such as phonon scattering. Experimental data fits excellent to an exponentially damped harmonic oscillation $\cos(\Omega \cdot (t - t_0)) \cdot \exp(-(t - t_0)/\tau)$. On resonance, the exponential damping constant τ of the Rabi oscillations is determined by the pure dephasing time T_2^* via $1/\tau = 3/(4\,T_1) + 1/(2\,T_2^*)$ [18]. After turning off the driving field, the fluorescence decays
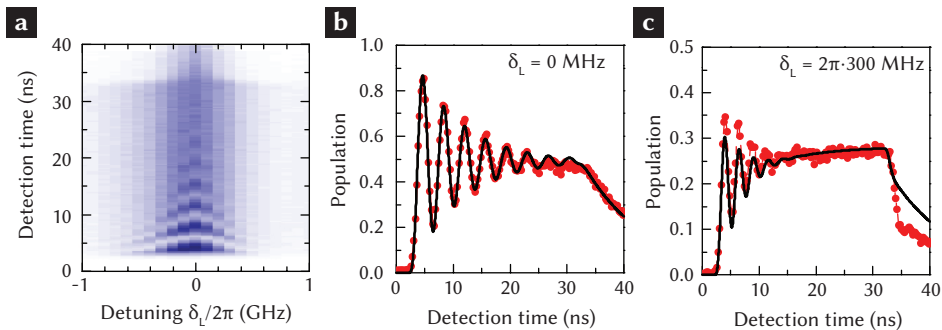
Figure 4.3 | Optical Rabi oscillations - detuning dependence. a, Rabi oscillations as function of detuning for $\Omega_0 = 2\pi \cdot 272$ MHz. **b-c,** Comparison of measured Rabi oscillations on resonance **b** and 300 MHz detuned **c**, and numerical data obtained from numerically integrating the optical Bloch equations.

exponentially due to spontaneous emission $\propto \exp(-t/T_1)$ with a lifetime T_1 of 10.9 ns.

In Fig. 4.3a we show Rabi oscillations for NV2 as function of laser detuning δ_L. For detuned excitation the oscillation frequency increases to the generalized Rabi frequency $\Omega = \sqrt{\Omega_0^2 + \delta_L^2}$, while the oscillation amplitude decreases $\propto \Omega_0^2/(\Omega_0^2 + \delta_L^2)$ [19]. To accurately reproduce our experimental transients we numerically integrate the optical Bloch equations (Fig. 4.3b, c) [19], taking into account finite rise- and fall times of the driving field, and applying a spectral average over a Gaussian distribution of detuning values of FWHM $b = 2\pi \cdot 40$ MHz. We assume a pure dephasing time of $T_2^* = 10$ ns, consistent with the observed linewidth of $\Delta = 46$ MHz. The same simulation parameters are used to model the on-resonance as well as the 300 MHz detuned transient. This simulation reproduces features for the detuned transients beyond the exponentially damped cosine, such as (i) the offset of the oscillations which increases with a negative exponential, (ii) the pronounced kink arising from the state vector adiabatically following the detuned field vector during the finite fall-time of our excitation pulses and (iii) an increased damping rate [19].

4.5 Decoherence mechanisms

In Fig. 4.4a we show the observed damping constant of Rabi oscillations on NV1 and NV2 as function of the Rabi frequency. Coherence of Rabi oscillations is ultimately limited by fast dephasing processes on a nanosecond timescale, such as phonon scattering [16]. However, for measurements that sum over several excitation cycles, such as the one in Fig. 4.2a, we expect to be limited by slow processes such as the spectral jumps observed in Fig. 4.1c. The total measurement represents an average over different detuning values and thus different Rabi frequencies, which leads to a faster damping of the observed oscillations. Consequently, for
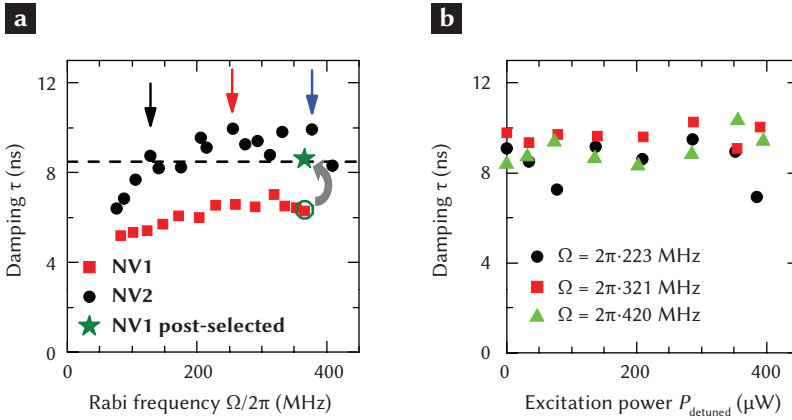
Figure 4.4 | Coherence of Rabi oscillations. a, Damping constant τ of Rabi oscillations as function of Rabi frequency. The dashed line indicates limit of τ for T_2 set by the single-scan linewidth $\Delta = 48$ MHz. Coherence is limited by spectral jumps (note difference between NV1 and NV2). Postselection can remove deteriorating effects of spectral jumps and enhance τ to the value expected from the linewidth. **b,** An additional laser field at λ=640 nm is applied: This detuned laser has no influence on coherence.

NV2 we observe a better coherence than for NV1. For Rabi frequencies much larger than the spectral width of the distribution of resonances, the deteriorating effect of spectral jumps vanishes, since the Rabi frequency always largely exceeds the detuning. This is apparent in the initial increase of τ for NV2 which quickly settles to about 9 ns for $\Omega > 2\pi \cdot 200$ MHz. This value is close to the coherence expected from the linewidth (dashed line in Fig. 4.4a).

Previous research[7] suggested a decrease of coherence with increasing driving power. To investigate possible influence of the red laser on the coherence which is not related to the NV center resonance, we measured the damping of Rabi oscillations while also shining a detuned ($\lambda = 640$ nm) red laser onto the same NV center (Fig. 4.4b). Even at an excitation power one order of magnitude larger than used for driving optical Rabi oscillations, we see no significant effect of the off-resonant laser. We conclude that for NV centers, optical coherence is not intrinsically limited by off-resonant effects of the driving field itself.

4.6 Prolonging coherence by resonance probing

Summarizing these findings, the contrast of two-photon interference using NV centers will primarily be limited by frequency fluctuations of the emitted photons. We make use of the slow timescale of these fluctuations to show that even for NV centers suffering from unstable lines, the spectral stability (i.e. the coherence time) set by the single-scan linewidth can be reached. For that purpose we modify our measurement protocol: after each green
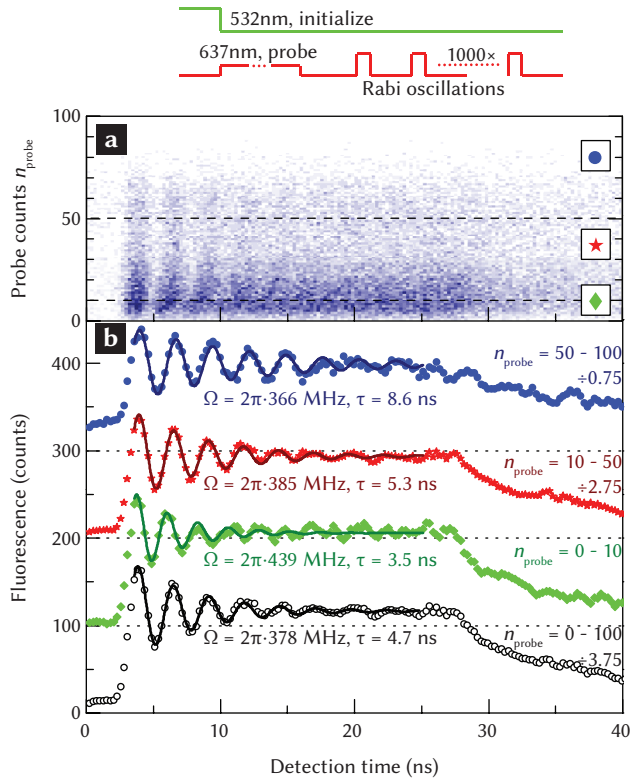
Figure 4.5 | Retrieving coherence. a, Detuning-resolved Rabi oscillations: detuning from resonance is derived from fluorescence counts during a 20 ms weak resonant probe pulse. Subsequently measured Rabi oscillations are plotted as function of this count rate. Total data is obtained from $3 \cdot 10^7$ excitation cycles. **b,** Data from plot (a) is summed within three ranges. On resonance (high counts during probe pulse) oscillations show lower Rabi frequency and increased coherence. Transients have been scaled by the indicated factor for better comparison.

initialization pulse we introduce an additional (weak) resonant laser pulse of t = 20 ms and count the photons n_{probe} detected during that interval. These counts n_{probe} now serve as a measure of the laser detuning during that specific interval. For large detuning we expect low n_{probe}, while resonance is identified by a large value of n_{probe}. We then record the time-resolved fluorescence during the strong (Rabi) pulses as a function of n_{probe} (Fig. 4.5a). The measured data is divided into three regions of n_{probe} and each of them is summed (Fig. 4.5b). For low n_{probe} we identify the characteristic features of detuned excitation, as already observed in Fig. 4.3c: increased Rabi frequency, increased damping, and a kink at the falling edge of the driving pulse. Post-selecting on-resonance events in turn leads to improved coherence: Already the damping time of the intermediate region of n_{probe} outperforms the value for the overall data. Strikingly, selecting only the events with highest n_{probe}, the damping time is nearly doubled, and reaches the value expected from single-sweep linewidth measurements (Fig. 4.4a). This scheme therefore allows for heralded two-photon interference for emitters with unstable resonances, provided that spectral jumps happen on a timescale which is slow compared to the photon detection rate. Compared to an interference experiment based on spectral filtering of the emission lines of both emitters to ensure resonance, this scheme yields higher interference contrast as detector dark counts only need to be accumulated while emitters are resonant to the driving field.

4.7   Conclusions

In summary, we demonstrated coherent control over the NV center's orbital state. Rabi frequencies $\Omega > 2\pi\cdot400\,\mathrm{MHz}$ with more than 10 oscillations have been observed. Damping of Rabi oscillations is dominated by slow spectral jumps of the NV's resonance frequency, which however can be overcome by a detuning sensitive stage prior to coherent control. This result highlights the good prospects for quantum information processing based on probabilistic entanglement of distant NV centers using two-photon interference.

4.8 Bibliography

[1] S. Olmschenk *et al.* Quantum Teleportation Between Distant Matter Qubits. *Science* **323**, 486 (2009).

[2] D. L. Moehring *et al.* Entanglement of single-atom quantum bits at a distance. *Nature* **449**, 68 (2007).

[3] C. K. Hong, Z. Y. Ou and L. Mandel. Measurement of subpicosecond time intervals between two photons by interference. *Physical Review Letters* **59**, 2044 (1987).

[4] K. Sanaka, A. Pawlis, T. Ladd, K. Lischka and Y. Yamamoto. Indistinguishable Photons from Independent Semiconductor Nanostructures. *Physical Review Letters* **103**, 053601 (2009).

[5] R. B. Patel *et al.* Postselective Two-Photon Interference from a Continuous Nonclassical Stream of Photons Emitted by a Quantum Dot. *Physical Review Letters* **100**, 207405 (2008).

[6] T. H. Stievater *et al.* Rabi Oscillations of Excitons in Single Quantum Dots. *Physical Review Letters* **87**, 133603 (2001).

[7] A. Batalov *et al.* Temporal Coherence of Photons Emitted by Single Nitrogen-Vacancy Defect Centers in Diamond Using Optical Rabi-Oscillations. *Physical Review Letters* **100**, 77401 (2008).

[8] C. Santori, D. Fattal, J. Vučković, G. S. Solomon and Y. Yamamoto. Indistinguishable photons from a single-photon device. *Nature* **419**, 594 (2002).

[9] A. Högele *et al.* Voltage-controlled optics of a quantum dot. *Physical Review Letters* **93**, 217401 (2004).

[10] F. Jelezko *et al.* Single spin states in a defect center resolved by optical spectroscopy. *Applied Physics Letters* **81**, 2160 (2002).

[11] S. Kummer, S. Mais and T. Basché. Measurement of Optical Dephasing of a Single Terrylene Molecule with Nanosecond Time Resolution. *The Journal of Physical Chemistry* **99**, 17078 (1995).

[12] N. B. Manson, J. P. Harrison and M. Sellars. Nitrogen-vacancy center in diamond: Model of the electronic structure and associated dynamics. *Physical Review B* **74**, 104303 (2006).

[13] P. Tamarat *et al.* Spin-flip and spin-conserving optical transitions of the nitrogen-vacancy centre in diamond. *New Journal of Physics* **10**, 045004 (2008).

[14] P. Neumann *et al.* Single-Shot Readout of a Single Nuclear Spin. *Science* **329**, 542 (2010).

[15] F. J. Heremans, G. D. Fuchs, C. F. Wang, R. Hanson and D. D. Awschalom. Generation and transport of photoexcited electrons in single-crystal diamond. *Applied Physics Letters* **94**, 152102 (2009).

[16] K.-M. C. Fu *et al.* Observation of the Dynamic Jahn-Teller Effect in the Excited States of Nitrogen-Vacancy Centers in Diamond. *Physical Review Letters* **103**, 256404 (2009).

[17] I. Gerhardt *et al.* Coherent state preparation and observation of Rabi oscillations in a single molecule. *Physical Review A* **79**, 011402 (2009).

[18] T. Basché, W. E. Moerner, M. Orrit and U. P. Wild (editors). *Single-Molecule Optical Detection, Imaging and Spectroscopy.* Wiley-VCH, Weinheim (1996).

[19] L. Allen and J. H. Eberly. *Optical resonance and 2-level atoms.* Dover, New York (1987).

Spin dynamics in the optical cycle of single nitrogen-vacancy centres in diamond

L. Robledo, H. Bernien, T. van der Sar, and R. Hanson

We investigate spin-dependent decay and intersystem crossing in the optical cycle of single negatively-charged nitrogen-vacancy (NV) centres in diamond. We use spin control and pulsed optical excitation to extract both the spin-resolved lifetimes of the excited states and the degree of optically-induced spin polarization. By optically exciting the centre with a series of picosecond pulses, we determine the spin-flip probabilities per optical cycle, as well as the spin-dependent probability for intersystem crossing. This information, together with the independently measured decay rate of singlet population provides a full description of spin dynamics in the optical cycle of NV centres. The temperature dependence of the singlet population decay rate provides information on the number of singlet states involved in the optical cycle.

5.1 Introduction

Nitrogen-vacancy (NV) centres in diamond are well-defined quantum systems in the solid state, with excellent spin coherence properties[1]. Even at ambient conditions, NV centres have successfully been used in the field of quantum information processing[2–8], magnetic sensing[9–13] and photonic devices[14–19]. However, despite the rapid experimental progress the understanding of the optically-induced spin-dynamics of the NV centre is still incomplete. In particular, the spin-dependent intersystem crossing (ISC) rates as well as the number of singlet states involved in the optical cycle are still debated. These parameters are responsible for optical spin initialization and readout, and are important for a correct estimation of photon emission rates. We extract these values by a series of room-temperature experiments, where we perform spin-resolved fluorescence lifetime measurements using picosecond optical excitation pulses. The lifetime of the singlet manifold is measured by analyzing the initial fluorescence rate for consecutive microsecond optical pulses with variable delay. The temperature dependence of this lifetime yields insight into the number of involved singlet states.

5.2 Experimental methods

We investigate individual NV centres contained in a high-temperature high-pressure (HTHP) grown type IIa diamond sample from Element Six ($\langle 111 \rangle$ oriented). The sample is studied in a scanning confocal microscope setup operated at $T = 10 \dots 300$ K. Spin control is achieved via microwave (MW) fields applied to an Au-waveguide that is lithographically defined on the diamond surface[6,8]. For optical excitation we use a continuous-wave (CW) laser at $\lambda = 532$ nm, equipped with an acousto-optic modulator (AOM) with 20 ns rise-time, as well as a frequency-doubled diode laser at $\lambda = 532$ nm with a pulse length of 62 ps (max. pulse energy: 25 nJ) and variable repetition rate. For photon detection we use an avalanche photo diode in the single-photon counting regime with a timing jitter of 450 ps. Time-resolved data are acquired using a time-correlated single photon counting module with a jitter of 10 ps, using a bin size of 512 ps. An arbitrary waveform generator (channel-to-channel jitter < 100 ps) is used as timing source of the experiment.

5.3 Model

The photo-dynamics of the NV centre (figure 5.1a) are determined by six electrons, which in the ground state form a triplet occupying an orbital of $^3A_2$ symmetry. The centre can be excited via a dipole-allowed transition to a ^3E triplet state. This level also has a spin-dependent probability to undergo ISC to a series of singlet states[20]. We use a five-level model to describe the spin dynamics of the NV centre (figure 5.1b). Spin-spin interaction splits the $^3A_2$ ground state by $D_{GS} = 2.87$ GHz into a state with spin projection $m_s = 0$ ($|1\rangle$) and a doublet with $m_s = \pm 1$ (summarized in $|2\rangle$). Correspondingly, the excited ^3E state is labelled
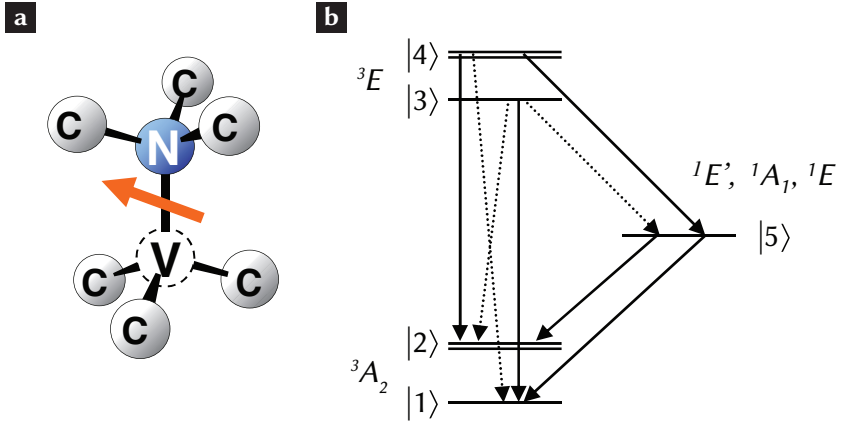
Figure 5.1 | Lattice structure and energy structure of the NV centre. a, A substitutional nitrogen atom N next to a vacancy V in the diamond lattice C. **b,** We consider spin-conserving (k_{31}, k_{42}) and spin-flip (k_{32}, k_{41}) transitions between triplets (states with spin projection $m_s = \pm 1$ are merged into states $|2\rangle$, $|4\rangle$). Spin-dependent ISC rates connect triplets to the singlet states (summarized as $|5\rangle$), and described by rates $k_{35}, k_{45}, k_{51}, k_{52}$. As discussed in section 6, we assume $k_{32}, k_{41} \ll k_{31}, k_{42}$ and find that $k_{35} \ll k_{45}$, but $k_{51} \approx k_{52}$.

$|3\rangle$ ($m_s = 0$, associated with a lifetime $T_{1,|3\rangle}$, where $T_{1,|n\rangle}$ denotes the relaxation time of state $|n\rangle$)) and $|4\rangle$ ($m_s = \pm 1$, lifetime $T_{1,|4\rangle}$), and split by $D_{ES} = 1.43\,\text{GHz}$[21,22].

Two singlet states with a splitting of $\Delta E = 1.189\,\text{eV}$ have been identified experimentally[23,24], but recent theoretical studies[25] and also data obtained in this work suggest the presence of a third singlet state between $^3A_2$ and ^3E. For the analysis of spin dynamics, however, we summarize the singlet states in $|5\rangle$, and the corresponding lifetimes are summed and denoted as $T_{1,|5\rangle}$. Rates from state $|m\rangle$ to state $|n\rangle$ are denoted by k_{mn}, and we only consider relaxation rates indicated in figure 5.1b. Population in state $|n\rangle$ is denoted by P_n, and the spin polarization in ground and excited state are denoted by $\mathbb{P}_{GS} = P_1/(P_1 + P_2)$ and $\mathbb{P}_{ES} = P_3/(P_3 + P_4)$.

5.4 Spin-dependent lifetime

Pulsed optical excitation and time-resolved detection of fluorescence provides a simple and direct way to determine the lifetime of the excited state in an optical transition. If the excitation pulse is short compared to the lifetime T_1, the detected time-resolved fluorescence (averaged over many excitation cycles) decays exponentially $I \propto \exp(-t/T_1)$. However, if the system under consideration is excited into a mixture of n excited states with different

lifetimes, the detected fluorescence decays according to a multi-exponential function:

$$I \propto \sum_n a_n \exp(-t/T_{1,|n\rangle}).$$

(5.1)

This situation is present in the case of NV centres in diamond, where the excited state is composed of a spin triplet. Population in this state decays radiatively to the triplet ground state, where we assume the different spin projections to have identical oscillator strength, based on the observation that the initial fluorescence rate is independent of the spin state as observed by [26] and as shown at a later point in this section. However, because of spin-dependent ISC [20], the effective lifetime of the excited state is significantly different for states $|3\rangle$ and $|4\rangle$. In literature [22,26,27] the NV centre's lifetime generally is obtained by fitting the time-resolved fluorescence to a single-exponential decay, leading to values of $T_{1,|3\rangle} \approx 12 - 13$ ns and $T_{1,|4\rangle} \approx 8$ ns in bulk diamond. Since optically induced spin polarization in NV centres is limited [28,29], in fact we expect such a lifetime measurement to yield a bi-exponential decay curve with time constants set by the sums of rates out of states $|3\rangle$ and $|4\rangle$ [$T_{1,|3\rangle} = 1/(k_{31} + k_{32} + k_{35})$ and $T_{1,|4\rangle} = 1/(k_{41} + k_{42} + k_{45})$], and amplitudes a_n determined by the initial spin polarization. Such a bi-exponential decay has been observed in [29], where a polarization of $\mathbb{P}_{ES} = 0.84 \pm 0.08$ % has been obtained. These data are based on fluorescence lifetime measurements with MW spin manipulation in the excited state, where the duration of the MW pulse was neglected, and the pulse was assumed to be perfect.

Here we present a simple and reliable way to obtain the spin-dependent lifetimes, without any assumptions on the MW pulse and spin polarization. For that purpose we drive Rabi oscillations in a conventional fashion, i.e. we apply a $1.3\,\mu$ s long off-resonant laser pulse to polarize the electron spin, followed by a MW pulse of variable duration, resonant with the zero-field splitting of $D = 2.87$ GHz. After the MW, we apply a ps laser pulse. The fluorescence as function of MW pulse duration is shown in figure 5.2b. For comparison we also plot the result of a conventional spin readout (figure 5.2c), i.e. the fluorescence integrated over the first 300 ns of the subsequent polarization laser pulse [30]. The data in figure 5.2b clearly reveal the oscillations in decay time which are in phase with oscillations of the electron spin. We note that the maximum amplitude changes by less than 1% as function of the spin state, consistent with our initial assumption on the oscillator strength. To accurately fit these data to a bi-exponential decay we sum over all MW pulse durations, which gives similar contribution from each spin state. From the fit we obtain the two time constants $T_{1,|3\rangle} = 13.7 \pm 0.1$ ns and $T_{1,|4\rangle} = 7.3 \pm 0.1$ ns (figure 5.2d). By using these values as constants for a fit to the individual decay curves, we can determine the relative contributions of states $|3\rangle$ and $|4\rangle$ to the minima and maxima of the Rabi oscillation data from the relative amplitudes of the two exponentials. For this particular centre, we find $\mathbb{P}_{ES,max} = 72.1 \pm 0.9\%$ and $\mathbb{P}_{ES,min} = 12.2 \pm 0.5\%$ (figure 5.2e). The value of $\mathbb{P}_{GS,max}$ may be larger due to a non-perfect spin conservation in optical excitation (see section 5.6). For other centres, we find values for $\mathbb{P}_{ES,max}$ of $72.4 \pm 0.9\%$, $79.4 \pm 0.2\%$ and $81.7 \pm 0.9\%$. The optically induced spin polarization may also depend on the probability of the NV centre to occupy the neutral charge state NV^0. When switching from neutral to the negative charge state under optical
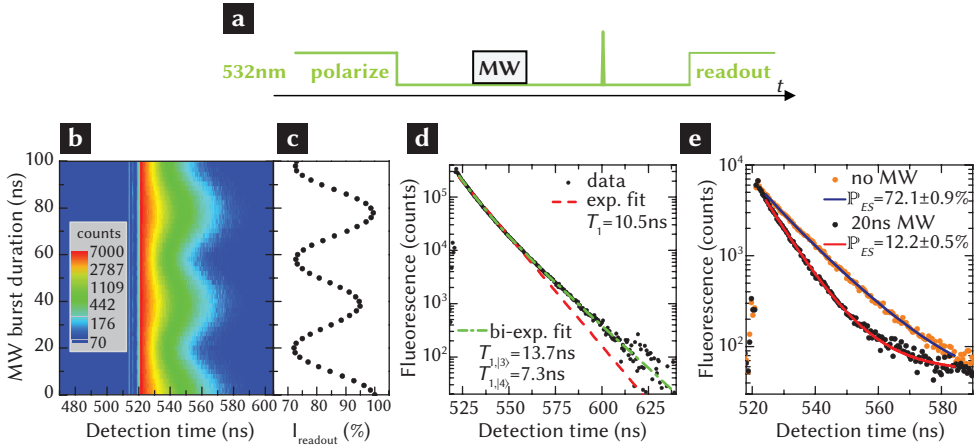
Figure 5.2 | Spin-dependent lifetime. a, We first polarize the spin by applying a 1.3 μs laser pulse at $\lambda = 532$ nm. After 800 ns we turn on a MW field at 2.87 GHz for a variable duration. 200 ns after begin of the MW we excite the NV centre by a 62 ps laser pulse at $\lambda = 532$ nm and measure the time-resolved emission. The first 300 ns of the subsequent polarization pulse is used for spin readout. The experiment was performed at $T = 300$ K. **b,** Fluorescence decay as function of MW burst duration (fluorescence counts are encoded in a logarithmic colour scale). The decay time oscillates with the $m_s = 0$ amplitude, as confirmed by **c,** conventional spin readout. **d,** Fluorescence decay curve, integrated over all applied MW burst durations (a constant background has been subtracted). A fit using a bi-exponential function, yields the lifetime of states $|3\rangle$ and $|4\rangle$. A single-exponential function (shown for comparison) cannot accurately fit the experimental data. **e,** Degree of spin polarization $\mathbb{P}_{ES} = P_3/(P_3 + P_4)$ with no MW applied and after a 20 ns MW pulse, obtained from the relative amplitudes of a bi-exponential fit.

excitation, the spin state will likely be random, thus lowering the observed spin polarization of NV$^-$. Here, we took care to work with centres with an NV^0 contribution of less than 5% of the overall emission.

The discrepancy between $\mathbb{P}_{ES,max}$ and $1 - \mathbb{P}_{ES,min}$ is a consequence of the $S = 1$ nature of the NV ground state: For a spin $S = 1$ system with degenerate levels $m_s = \pm 1$ (i.e. for NV centres in absence of magnetic field), the effect of resonant MW driving starting from a pure $|m_s = 0\rangle$ state is to cause coherent oscillations between $|m_s = 0\rangle$ and the symmetric superposition $|m_s = +1\rangle + |m_s = -1\rangle$. In a more realistic scenario we need to consider an only partially polarized state, where the density matrix subspace spanned by $|m_s = +1\rangle$ and $|m_s = -1\rangle$ has equal population of the symmetric and antisymmetric superposition state. Only the symmetric state will be transferred back to $|m_s = 0\rangle$, so the effect of a half-oscillation is to transfer the full $m_s = 0$ population into $m_s = \pm 1$, while only half of the incoherent

population in $m_s = -1$ and $m_s = +1$ is transferred back into $m_s = 0$. As a consequence, when driving Rabi oscillations, the maximum population in $m_s = 0$ will only reach half the value of the maximum population in $m_s = \pm 1$ (figure 5.2e: $\mathbb{P}_{ES,min} \approx (1 - \mathbb{P}_{ES,max})/2$).

In summary, the presented method allows for accurate determination of the lifetime of the pure states $|3\rangle$ and $|4\rangle$, without the need of assumptions on the quality of spin manipulation. The knowledge of these lifetimes can then be used to quantify the spin polarization.

5.5 Temperature dependence of singlet decay

An important parameter for the spin dynamics of the NV centre under optical excitation is the time population spends in the singlet manifold before it decays back to the triplet ground state. This time scale is long compared to the excited state lifetime, and since ISC into the singlet states occurs more likely out of the $m_s = \pm 1$ than out of the $m_s = 0$ excited state, this leads to a reduced fluorescence rate for $m_s = \pm 1$. This fact is routinely used for non-resonant spin readout[30].

The temperature dependence of this decay rate yields information on the energy splitting involved in this relaxation process, and adds further evidence for the number of singlet states contributing to the optical cycle of NV centres. Recently an infrared (IR) emission channel was observed, and attributed to a dipole-allowed transition between two singlet levels with an energy splitting of $\Delta E = 1.189\,\text{eV}$[23,24]. In the same publications it was shown that the IR emission follows the same time dependence as the visible transition, implying a short lifetime of the upper singlet state. Therefore the previously observed long-lived singlet state was attributed to the ground state of this IR transition.

The temperature dependence of this singlet state lifetime has been reported for an ensemble of NV centres based on IR absorption measurements[24]. Here, we present data obtained on single NV centres. Since the oscillator strength of the IR transition is very weak, we use an indirect way to obtain this timescale, following the method used in[20]: We first apply a green pulse (500 ns) to reach a significant population of the singlet states. This population manifests itself in reduced steady-state fluorescence with respect to the beginning of the pulse. After a variable delay we apply a second 500 ns pulse (figure 5.3a, b). During the delay between the pulses, population stored in the singlet states decays back to the triplet ground state. The fluorescence at the beginning of the second pulse is proportional to the population in the triplet ground state and thus we can attribute its dependence on inter-pulse delay to the population decay out of the singlet state. In figure 5.3c we integrate the photons emitted during the first 30 ns of the second pulse for each inter-pulse delay and fit these data to an exponential function. Figure 5.3d summarizes the timescales we obtained in this way, for temperatures ranging from $T = 13\,\text{K}$ to $T = 300\,\text{K}$ for three different NV centres.

We model the lifetime τ of the singlet state as a combination of temperature-independent spontaneous decay rate τ_0^{-1} and a rate accounting for stimulated emission of phonons of energy ΔE with an occupation given by Bose-Einstein statistics: $\tau = \tau_0[1 - \exp(-\Delta E / k_B T)]$.
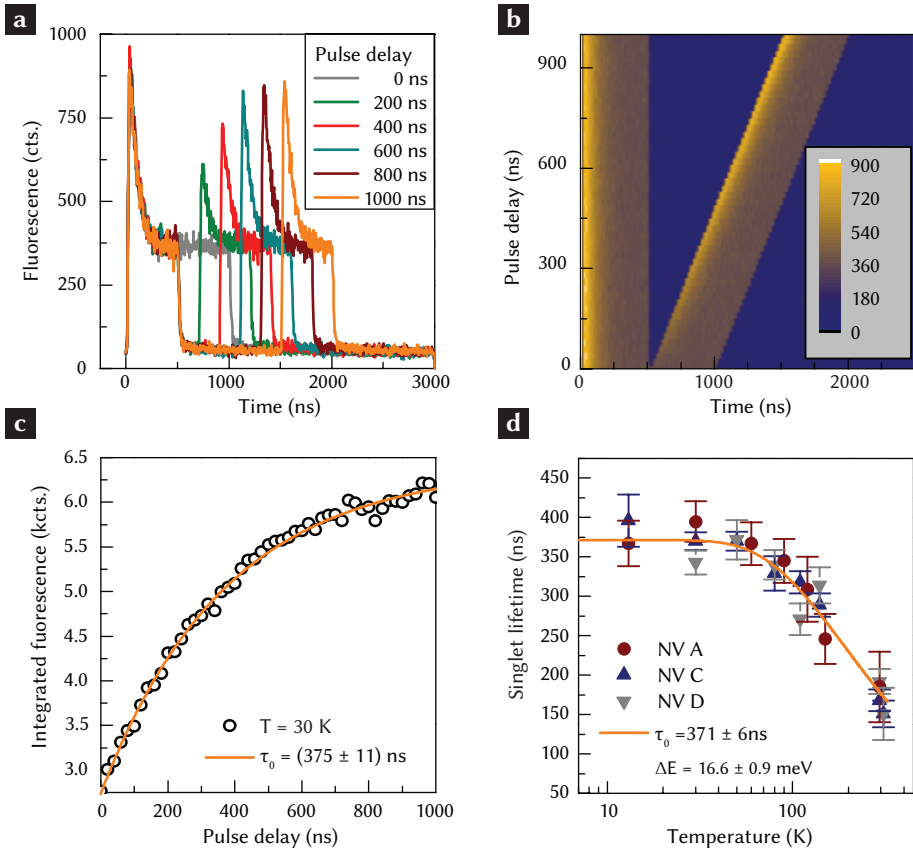
Figure 5.3 | Singlet lifetime. Decay of population from singlet states leads to recovery of fluorescence: **a,** individual traces and **b** full data set of NV fluorescence with two excitation pulses and variable delay. **c,** Fluorescence counts integrated over first 30 ns of second pulse as function of inter-pulse delay. The exponential increase is caused by decay out of singlet states. **d,** Temperature dependence of singlet decay rate. The fit assumes a phonon-assisted decay process.

The fit yields a spontaneous emission lifetime of $\tau_0 = 371 \pm 6$ ns and a phonon energy of $\Delta E = 16.6 \pm 0.9$ meV, in reasonable agreement with ensemble data obtained in [24].

This result suggests that, apart from the 1.189 eV splitting, a third level ΔE below the IR transition's ground state is involved in the optical cycle of the NV centre. We can exclude that this third level is the triplet ground state, just 16.6 meV below the lowest singlet, as this would imply phonon-assisted spin relaxation on a sub-microsecond time scale at room temperature. This scenario clearly contradicts experimentally observed spin lifetimes on a millisecond timescale [5,8]. Consequently the third level is likely to be another singlet state. The presence of three singlet states in between the triplet $^3A_2$ and ^3E states was recently predicted by an ab-initio calculation of the excited states in the NV centre [25], however, there a larger energy splitting between the lowest singlet states was obtained.

5.6   Polarization probability

Polarizing the electron spin by off-resonant optical excitation is a key technique for room-temperature spin manipulation of NV centres. Although this effect already has been identified to be caused by a spin-dependent ISC rate [20,31–33], little is known about the relative contributions of spin-flip transitions between triplet states (k_{32}, k_{41}), and ISC rates ($k_{35}, k_{45}, k_{51}, k_{52}$). We address this question by determining the polarization change due to a single excitation cycle.

For that purpose we first initialize the NV spin by a 2 μs polarization pulse. After a waiting time of 1 μs we excite the NV centre by a reference ps-pulse and measure the spin polarization by analyzing the relative contributions of the amplitudes in a bi-exponential fit to the fluorescence decay curve, as outlined in the previous section. This polarization corresponds to the steady-state value after CW excitation. To determine the change in polarization per excitation cycle we now apply a MW pulse to transfer the $m_s = 0$ population into the $m_s = \pm 1$ states and then drive individual excitation cycles by applying 10 consecutive ps-pulses separated by 2 μs. For each excitation cycle, we again determine the spin polarization (figure 5.4c). All these bi-exponential fits use the same two time constants, obtained from a fit to the sum of all decay curves. From a power dependence measurement of the NV fluorescence rate we determine an excitation probability per ps-pulse of $\alpha = 0.95 \pm 0.05$.

The effect of a single excitation cycle on the spin polarization can be described by two counter-acting probabilities: a spin-flip from $|1\rangle$ to $|2\rangle$ (p_{12}) and the opposite process (p_{21}). Here, we consider only optically induced effects, i.e. the time between excitation pulses Δ_t is assumed to be much shorter than the spin-lattice relaxation time (this assumption is substantiated by the constant polarization P_{ES} for the 10 consecutive reference pulses in case of NV C [figure 5.4c]). For state $|m\rangle$, population just before pulse n is denoted by $P_{m,n}$, and just after the excitation pulse by $P'_{m,n}$. The steady state value $P_{m,n=\infty}$ is abbreviated by P_m. The pulse separation Δ_t is much larger than the singlet decay time, such that $P_{1,n} + P_{2,n} = 1$ and therefore $\mathbb{P}_{GS,n} = P_{1,n}/(P_{1,n} + P_{2,n}) = P_{1,n}$.
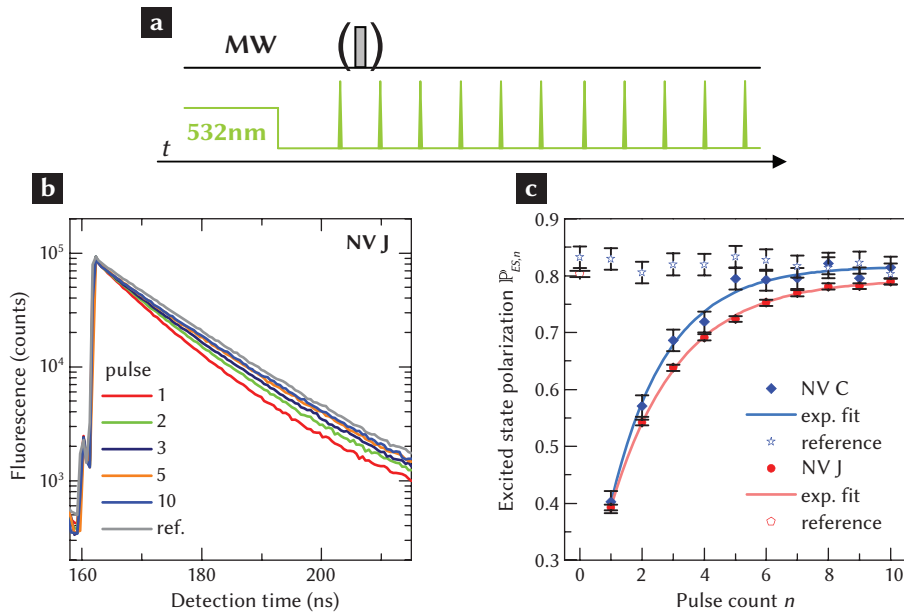
Figure 5.4 | Spinflips in the optical excitation cycle. a, We first polarize the spin by means of a 2 μs laser pulse at $\lambda = 532$ nm. After a delay of 1 μs we apply a sequence of 11 pulses of 62 ps duration at $\lambda = 532$ nm. For NV J, we apply a MW pulse 1 μs after the first ps-pulse to invert the spin state (for NV C we alternately run sequences with and without MW pulse). For each ps-pulse we measure the time-resolved emission. The experiment was performed at $T = 300$ K. **b,** Fluorescence decay for consecutive ps-excitation pulses. The decay follows a bi-exponential function. A reference ps-pulse after a green 2 μs spin polarization pulse yields the initial optically induced spin polarization. A subsequent MW pulse transfers polarization to $|2\rangle$. **c,** Change in polarization between consecutive pulses yields spin-flip probabilities $p_{12}(|1\rangle \rightarrow |2\rangle)$ and $p_{21}(|2\rangle \rightarrow |1\rangle)$ per optical excitation cycle.

Experimentally, we obtain spin polarization in the excited state. This differs from the ground state polarization due to a fraction $\epsilon = k_{23}/k_{13} = k_{14}/k_{24}$ of spin non-conserving transitions. The populations for the $(n + 1)^{th}$ excitation pulse are then given by:

$$P_{1,n+1} = \alpha p_{21} P_{2,n} + (1 - \alpha p_{12}) P_{1,n} \tag{5.2}$$

$$P_{2,n+1} = \alpha p_{12} P_{1,n} + (1 - \alpha p_{21}) P_{2,n} \tag{5.3}$$

$$P'_{3,n+1} = \alpha \left(\frac{\epsilon}{1+\epsilon} P_{2,n+1} + \frac{1}{1+\epsilon} P_{1,n+1} \right) \tag{5.4}$$

$$P'_{4,n+1} = \alpha \left(\frac{\epsilon}{1+\epsilon} P_{1,n+1} + \frac{1}{1+\epsilon} P_{2,n+1} \right). \tag{5.5}$$

The asymptotic value of the polarization is $\mathbb{P}_{GS} = p_{21}/(p_{12} + p_{21})$, and the excited state $\mathbb{P}_{ES,n} = P'_{3,n}/(P'_{3,n}+P'_{4,n}) = \left[P_{1,n} (1 - \epsilon) + \epsilon \right] / (1 + \epsilon) \approx P_{1,n}$ closely follows the ground state spin polarization for small ϵ. In [20] an upper bound of $\epsilon \leq 0.02$ is used, based on the maximum spin polarization of 80%. By comparison with a numerical solution of the rate equations of the five-level-model outlined in section 2, we also find that the experimentally observed contrast in spin readout (figure 5.5) is best reproduced by $\epsilon \leq 0.02$. The change in polarization per pulse (figure 5.4c) can be fitted by an exponential function $\mathbb{P}_{ES}(n) = \mathbb{P}_{ES} + a \exp(-n/c)$. From the steady-state polarization $\mathbb{P}_{ES}$ and the polarization rate c we can extract the spin-flip probabilities p_{21} and p_{12} per optical cycle. The values we obtain for p_{21} and p_{12} only weakly depend on ϵ in the range $\epsilon \leq 0.02$. Results are summarized in table 5.1.

Table 5.1 | Summary of parameters at T=300 K. We take $\alpha = 0.95 \pm 0.05$, $\epsilon = 0.01 \pm 0.01$ and use $T_{1,|5\rangle} = 178 \pm 6\,ns$ from section 5.5. p_{12} and p_{21} are the total spin-flip probabilities per optical cycle. p_{35}, p_{45}, p_{51} and p_{52} are the spin-dependent ISC probabilities for population in state $|3\rangle$, $|4\rangle$ and $|5\rangle$.

	NV J	NV C
p_{12}	0.078 ± 0.002	0.079 ± 0.004
p_{21}	0.315 ± 0.011	0.372 ± 0.017
$T_{1,|3\rangle}(ns)$	13.26 ± 0.03	13.1 ± 0.1
$T_{1,|4\rangle}(ns)$	6.89 ± 0.06	7.0 ± 0.2
p_{35}	0.14 ± 0.02	0.17 ± 0.03
p_{45}	0.55 ± 0.01	0.56 ± 0.02
p_{51}/p_{52}	1.15 ± 0.05	1.6 ± 0.4

Based on the relations $T_{1,|3\rangle} = 1/(k_{31} + k_{32} + k_{35})$, $T_{1,|4\rangle} = 1/(k_{41} + k_{42} + k_{45})$ and $T_{1,|5\rangle} = 1/(k_{51} + k_{52})$ [rates as indicated in figure 5.1b], we numerically solve the system of equations defining the five unknown rates $k_{31}, k_{35}, k_{45}, k_{51}, k_{52}$ using the measured parameters p_{12}, $p_{21}, T_{1,|3\rangle}, T_{1,|4\rangle}, T_{1,|5\rangle}$ and assuming a fixed $\epsilon = 0.01 \pm 0.01$. This way we obtain the spin-dependent ISC probabilities $p_{45} = k_{45}/(k_{41} + k_{42} + k_{45})$ and $p_{35} = k_{35}/(k_{31} + k_{32} + k_{35})$, and for the reverse process $p_{51}/p_{52} = k_{51}/k_{52}$. The results are summarized in Table 5.1. The
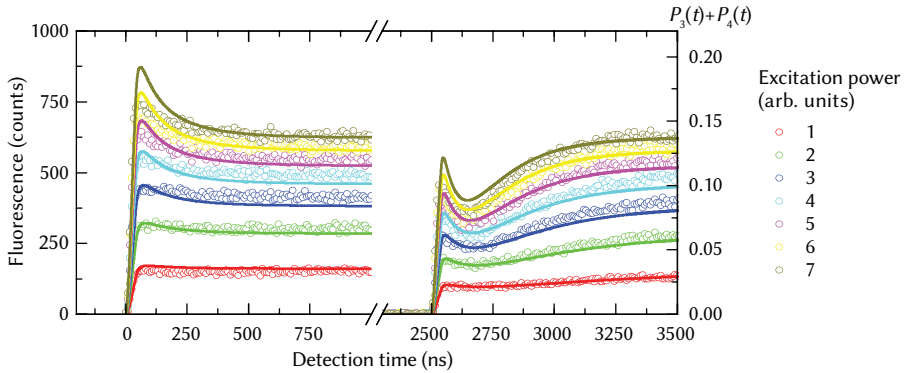
Figure 5.5 | Time-resolved excitation-power dependence. We measure and model the NV fluorescence excited by off-resonant 1 μs pulses. The first pulse displays the fluorescence of NV centres that are optically polarized into $m_s = 0$. The second pulse is obtained after applying a MW π-pulse, representing the fluorescence of a NV centre polarized in $m_s = \pm 1$. The model shows the population in states $|3\rangle$ and $|4\rangle$. The calculations are based on parameters from NV J, assuming $\epsilon = 0.01$ and $\alpha = 1$ (no fit is applied). Excitation rates are taken as integer multiples of 4 MHz.

low values of p_{51}/p_{52} are in contrast to the current picture of the singlet relaxation process, where $p_{52} = 0$ was used [20]. This gives another hint that an additional ^1E state needs to be considered for the relaxation process. The temperature dependence of p_{51}/p_{52} could give further insight into this topic.

We note that this set of parameters can be used to calculate the spin- and power dependence of time-resolved NV centre emission using μs excitation pulses at $\lambda = 532$ nm within the framework of this five-level model. The numerical result qualitatively agrees with experimental data (figure 5.5), however for higher excitation rates the model overestimates the initial fluorescence rate. This could be caused by a higher spin polarization of the centre from which we obtained the experimental data in figure 5.5 compared to parameters of NV J as used in the simulation.

5.7   Summary

We have experimentally determined the spin-dependent lifetime of the NV centre's excited state, whose difference is dominated by a spin-dependent ISC rate. Knowledge of these lifetimes allows us to determine the degree of spin polarization. In a second experiment, we identified the total lifetime of the singlet states, and, by analyzing its temperature dependence, the energy splitting of the long lived singlet transition. The measured energy of ≈ 16 meV indicates that at least three singlet states are involved in the optical cycle of the NV centre.

Finally, we determined the spin-dependent ISC probabilities by analyzing the change of spin polarization induced by a single excitation cycle, without making assumptions on number and nature of the singlet states. The results indicate that spin polarization is dominated by a preferential ISC out of the excited $m_s = \pm 1$ states instead of a selective decay out of the singlets into the $m_s = 0$ ground state. The obtained rates are consistent with spin-dependent NV fluorescence dynamics based on a five-level model.

5.8 Bibliography

[1] G. Balasubramanian *et al.* Ultralong spin coherence time in isotopically engineered diamond. *Nature Materials* **8**, 383 (2009).

[2] F. Jelezko *et al.* Observation of Coherent Oscillation of a Single Nuclear Spin and Realization of a Two-Qubit Conditional Quantum Gate. *Physical Review Letters* **93**, 130501 (2004).

[3] L. Childress *et al.* Coherent Dynamics of Coupled Electron and Nuclear Spin Qubits in Diamond. *Science* **314**, 281 (2006).

[4] M. V. G. Dutt *et al.* Quantum Register Based on Individual Electronic and Nuclear Spin Qubits in Diamond. *Science* **316**, 1312 (2007).

[5] P. Neumann *et al.* Multipartite entanglement among single spins in diamond. *Science* **320**, 1326 (2008).

[6] G. D. Fuchs, V. V. Dobrovitski, D. M. Toyli, F. J. Heremans and D. D. Awschalom. Gigahertz Dynamics of a Strongly Driven Single Quantum Spin. *Science* **326**, 1520 (2009).

[7] P. Neumann *et al.* Single-Shot Readout of a Single Nuclear Spin. *Science* **329**, 542 (2010).

[8] G. de Lange, Z. H. Wang, D. Riste, V. V. Dobrovitski and R. Hanson. Universal Dynamical Decoupling of a Single Solid-State Spin from a Spin Bath. *Science* **330**, 60 (2010).

[9] C. L. Degen. Scanning magnetic field microscope with a diamond single-spin sensor. *Applied Physics Letters* **92**, 243111 (2008).

[10] J. M. Taylor *et al.* High-sensitivity diamond magnetometer with nanoscale resolution. *Nature Physics* **4**, 810 (2008).

[11] J. R. Maze *et al.* Nanoscale magnetic sensing with an individual electronic spin in diamond. *Nature* **455**, 644 (2008).

[12] G. Balasubramanian *et al.* Nanoscale imaging magnetometry with diamond spins under ambient conditions. *Nature* **455**, 648 (2008).

[13] G. de Lange, D. Riste, V. V. Dobrovitski and R. Hanson. Single-Spin Magnetometry with Multipulse Sensing Sequences. *Physical Review Letters* **106**, 080802 (2011).

[14] K.-M. C. Fu *et al.* Coupling of nitrogen-vacancy centers in diamond to a GaP waveguide. *Applied Physics Letters* **93**, 234107 (2008).

[15] T. M. Babinec *et al.* A diamond nanowire single-photon source. *Nature Nanotechnology* **5**, 195 (2010).

[16] J. P. Hadden *et al.* Strongly enhanced photon collection from diamond defect centers under microfabricated integrated solid immersion lenses. *Applied Physics Letters* **97**, 241901 (2010).

[17] T. van der Sar *et al.* Deterministic nanoassembly of a coupled quantum emitter–photonic crystal cavity system. *Applied Physics Letters* **98**, 193103 (2011).

[18] P. Siyushev *et al.* Monolithic diamond optics for single photon detection. *Applied Physics Letters* **97**, 241902 (2010).

[19] D. Englund *et al.* Deterministic coupling of a single nitrogen vacancy center to a photonic crystal cavity. *Nano Letters* **10**, 3922 (2010).

[20] N. B. Manson, J. P. Harrison and M. Sellars. Nitrogen-vacancy center in diamond: Model of the electronic structure and associated dynamics. *Physical Review B* **74**, 104303 (2006).

[21] G. D. Fuchs *et al.* Excited-State Spectroscopy Using Single Spin Manipulation in Diamond. *Physical Review Letters* **101**, 117601 (2008).

[22] P. Neumann *et al.* Excited-state spectroscopy of single NV defects in diamond using optically detected magnetic resonance. *New Journal of Physics* **11**, 013017 (2009).

[23] L. Rogers, S. Armstrong, M. Sellars and N. B. Manson. Infrared emission of the NV centre in diamond: Zeeman and uniaxial stress studies. *New Journal of Physics* **10**, 103024 (2008).

[24] V. M. Acosta, A. Jarmola, E. Bauch and D. Budker. Optical properties of the nitrogen-vacancy singlet levels in diamond. *Physical Review B* **82**, 201202 (2010).

[25] Y. Ma, M. Rohlfing and A. Gali. Excited states of the negatively charged nitrogen-vacancy color center in diamond. *Physical Review B* **81**, 041204 (2010).

[26] A. Batalov *et al.* Temporal Coherence of Photons Emitted by Single Nitrogen-Vacancy Defect Centers in Diamond Using Optical Rabi-Oscillations. *Physical Review Letters* **100**, 77401 (2008).

[27] A. T. Collins, M. F. Thomaz and M. I. B. Jorge. Luminescence decay time of the 1.945 eV centre in type Ib diamond. *Journal of Physics C: Solid State Physics* **16**, 2177 (1983).

[28] J. P. Harrison, M. Sellars and N. B. Manson. Measurement of the optically induced spin polarisation of N-V centres in diamond. *Diamond and Related Materials* **15**, 586 (2006).

[29] G. D. Fuchs *et al.* Excited-state spin coherence of a single nitrogen–vacancy centre in diamond. *Nature Physics* **6**, 668 (2010).

[30] F. Jelezko and J. Wrachtrup. Read-out of single spins by optical spectroscopy. *Journal of Physics: Condensed Matter* **16**, R1089 (2004).

[31] A. P. Nizovtsev *et al.* NV centers in diamond: spin-selective photokinetics, optical ground-state spin alignment and hole burning. *Physica B: Condensed Matter* **340**, 106 (2003).

[32] J. P. Harrison, M. Sellars and N. B. Manson. Optical spin polarisation of the N-V centre in diamond. *Journal of luminescence* **107**, 245 (2004).

[33] A. P. Nizovtsev *et al.* A quantum computer based on NV centers in diamond: Optically detected nutations of single electron and nuclear spins. *Optics and Spectroscopy* **99**, 233 (2005).

High-fidelity projective readout of a solid-state spin quantum register

L. Robledo*, L. Childress*, H. Bernien*, B. Hensen, M. Markham, D.J. Twitchen, P.F.A. Alkemade, and R. Hanson

Initialization and readout of coupled quantum systems are essential ingredients for the implementation of quantum algorithms [1,2]. If the state of a multi-qubit register can be read out in a single shot, this enables further key resources such as quantum error correction and deterministic quantum teleportation [1], as well as direct investigation of quantum correlations (entanglement). While spins in solids are attractive candidates for scalable quantum information processing, thus far single-shot detection has only been achieved for isolated qubits [3–6]. Here, we demonstrate preparation and measurement of a multi-spin quantum register by implementing resonant optical excitation techniques originally developed in atomic physics. We achieve high-fidelity readout of the electronic spin associated with a single nitrogen-vacancy (NV) centre in diamond at low temperature, and exploit this readout to project up to three nearby nuclear spin qubits onto a well-defined state [7]. Conversely, we can distinguish the state of the nuclear spins in a single shot by mapping it onto and subsequently measuring the electronic spin [5,8]. Finally, we show compatibility with qubit control by demonstrating initialization, coherent manipulation, and single-shot readout in a single experiment on a two-qubit register, using techniques suitable for extension to larger registers. These results pave the way for the first test of Bell's inequalities on solid-state spins and the implementation of measurement-based quantum information protocols.

6.1 Introduction

The electronic spin of the NV centre in diamond constitutes an exceptional solid state system for investigating quantum phenomena, combining excellent spin coherence [9–12] with a robust optical interface [13–16]. Furthermore, the host nitrogen nuclear spin (typically ^{14}N, $I = 1$) and proximal isotopic impurity ^{13}C nuclei ($I = \frac{1}{2}$) exhibit hyperfine interactions with the NV electronic spin ($S = 1$), enabling development of few-spin quantum registers that have been envisioned as building blocks for quantum repeaters [17], cluster state computation [18], and distributed quantum computing [19]. All of these applications require high-fidelity preparation, manipulation, and measurement of multiple spins. While there have been significant advances in coherent control over few-spin systems in diamond [20,21], no method exists for simultaneous preparation [22,23] and single-shot readout [5] of multi-spin registers, impeding progress towards multi-qubit protocols. Here, we remove this roadblock by exploiting resonant excitation techniques, as pioneered in atomic physics [24,25], in micro-structured diamond devices that enable high photon collection efficiency (Fig. 6.1a). These new methods enable us to initialize multiple nuclear spin qubits, and to perform single-shot readout of a few-qubit register, clearing the way towards implementation of quantum algorithms with solid-state spins.

6.2 Resonant excitation of spin-selective optical transitions

Our preparation and readout techniques rely on resonant excitation of spin-selective optical transitions of the NV centre, which can be spectrally resolved at low temperatures [26]. We use the E_x and A_1 transitions in our experiments (see Fig. 6.1b): A_1 connects the ground states with $m_s = \pm 1$ spin projection to an excited state with primarily $m_s = \pm 1$ character, whereas E_x connects states with $m_s = 0$. A typical spectrum from NV A, one of the two NVs we study, is shown in Fig. 6.1c (see also Supporting Material). Under resonant excitation of a single transition, the fluorescence decays with time owing to a slight spin mixing within the excited states that induces shelving into the other spin state (Fig. 6.1d). This optical pumping mechanism enables high-fidelity spin state initialization [24,27]: from the data in Fig. 6.1d we estimate a preparation error into the $m_s = 0$ ground state of $0.3 \pm 0.1 \%$, which is a drastic reduction of the $11 \pm 3 \%$ preparation error observed with conventional off-resonant initialization (see Supporting Material).
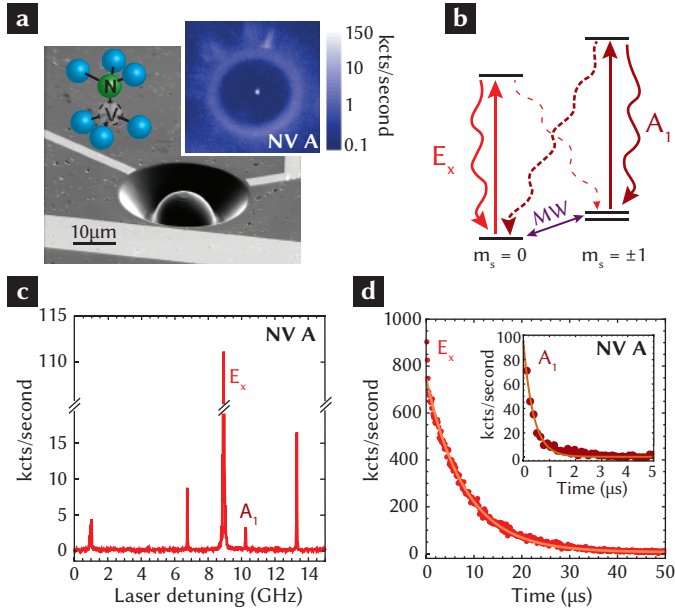
Figure 6.1 |Resonant excitation and electronic spin preparation of an NV centre.
a, Scanning electron microscope image of a solid immersion lens (SIL) representative of those used in the experiments. The overlayed sketch shows the substitutional nitrogen and adjacent vacancy that form the NV centre. Inset: Scanning confocal microscope image of NV A (log. colour scale). **b**, Energy levels used to prepare and read out the NV centre's electronic spin ($S = 1$ in the ground and optically excited states); transitions are labelled according to the symmetry of their excited state. Dashed lines indicate spin-non-conserving decay paths. **c**, Photoluminescence excitation spectrum of NV A, frequency is given relative to 470.443 THz. **d**, Fluorescence time trace of NV A, initially prepared in $m_s = 0$ (E_x excitation, $P = 4.8$ nW) and $m_s = \pm 1$ (A_1 excitation, $P = 7.4$ nW, inset), saturation power $P_{sat.} \approx 6$ nW. Spin flips in the excitation cycle lead to nearly exponential decay of fluorescence, with a fitted spin-flip time of $1/\gamma_0 = 8.1 \pm 0.1\,\mu s$ ($0.39 \pm 0.01\,\mu s$) for E_x (A_1), and an initial intensity of 740 ± 5 (95 ± 2) kcounts per second, giving a lower limit to the $m_s = 0$ and $m_s = \pm 1$ preparation fidelity of $99.7 \pm 0.1\,\%$ and $99.2 \pm 0.1\,\%$, respectively. The low initial counts on A_1 are associated with a fast intersystem crossing to metastable singlet states.

6.3 Single-shot readout of the electronic spin

Spin-dependent resonant excitation also allows single-shot electronic spin readout: the presence or absence of fluorescence under E_x excitation reveals the spin state. By working with low-strain NVs at low temperature ($T = 8.6$ K), we suppress spin-mixing[26,28] and phonon-induced transitions[29] within the excited states, extending the spin relaxation time under E_x excitation to several microseconds. Together with a high collection efficiency due to the use of solid immersion lenses[30] fabricated around pre-selected, low-strain NVs, and efficient rejection of resonant excitation from the measured phonon-sideband emission, this highly spin-preserving transition allows the detection of several photons before the spin flips.
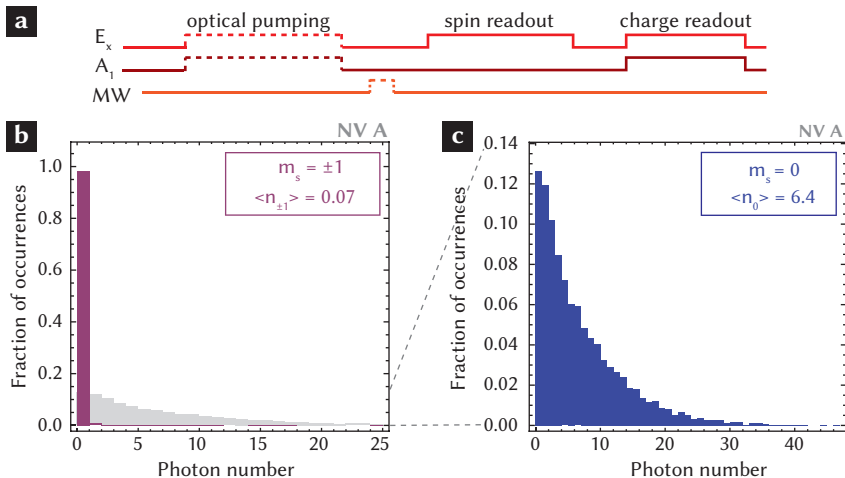
Figure 6.2 |Single-shot readout of the NV electronic spin. a, Pulse sequence used for electronic spin readout: after charge initialization (532 nm, not shown) the electron is pumped into $m_s = 0$ (A_1, dark red) or $m_s = \pm1$ (E_x, bright red), followed by optional microwave (MW) spin manipulation and the spin readout pulse resonant with E_x. Conditioning on simultaneous resonance during the final charge and detuning sensing stage eliminates effects of local electric field fluctuations or ionization. **b**, Statistics of photon counts detected during a $t_{ro} = 100\,\mu$s electronic spin readout after initialization into $m_s = \pm1$ (red) and $m_s = 0$ (superimposed light gray and **c**), obtained from 10000 measurement repetitions.

We demonstrate single-shot readout by initializing the electronic spin into $m_s = \pm1$ or $m_s = 0$, followed by resonant excitation on the E_x readout transition for $t_{ro} = 100\,\mu$s (Fig. 6.2a). The resulting histograms of the number of detected photons are given in Fig. 6.2b and c. As expected, for $m_s = \pm1$ we observe negligible excitation, with a 98.3 % probability to not measure any photon during the probe interval. In stark contrast, after initialization

into $m_s = 0$ we detect on average $\langle n_0 \rangle = 6.4$ photons per shot. We assign the state $m_s = 0$ to detection of one or more photons, and $m_s = \pm 1$ otherwise. After truncating our integration window to the optimal duration of $40\,\mu\text{s}$, we find an average fidelity $F_{\text{avg}} = \frac{1}{2}(F_{m_s=0} + F_{m_s=\pm 1}) = 93.2 \pm 0.5\%$; here F_{m_s} is the probability to obtain the measurement outcome m_s after optical pumping into m_s.
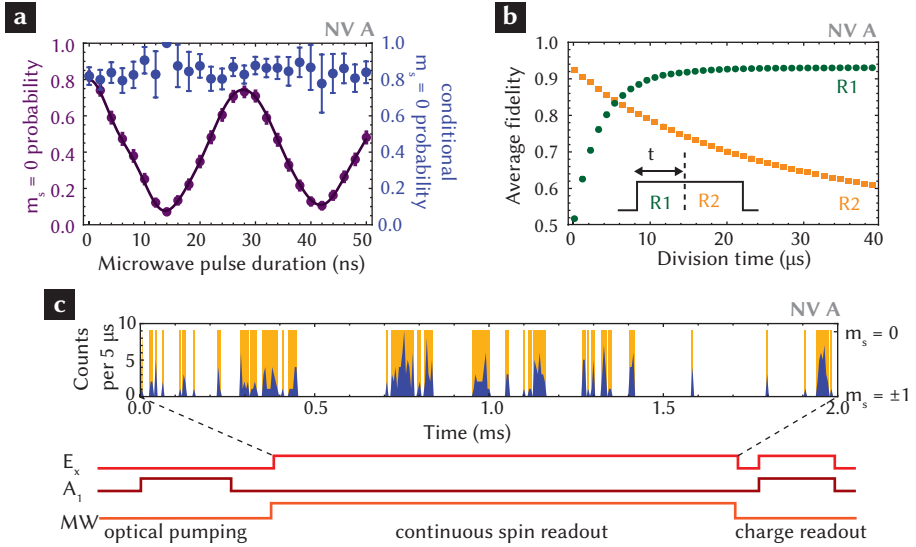
Figure 6.3 |Projective readout and quantum jumps. a, Electronic spin Rabi oscillations between $m_s = 0$ and $m_s = -1$ at $B_z \approx 15\,\text{G}$ (purple): each data point is obtained from 1000 single-shot readout repetitions. The fit, which includes the detailed hyperfine level structure, yields a visibility of $78 \pm 8\%$, where a maximum of 84% can be expected. Blue data points show the measurement outcome after projection into $m_s = 0$ by selecting only readout events with photons detected within the first 400 ns (see Supporting Material). All errors and error bars are 2 SE. **b**, When the $100\,\mu\text{s}$ readout pulse is divided into two readout segments R1 and R2 with variable division point, the fidelity of two consecutive segments reaches $83.4 \pm 0.5\%$ for an optimal division time of $5.5\,\mu\text{s}$; the probability of identical sequential outcomes is $82.0 \pm 0.7\%$. 2 SE error bars (n = 10000) are smaller than the symbols. **c**, Quantum jumps in the fluorescence time-trace during continuous spin readout. Durations of dark periods depend on the MW Rabi frequency (see Supporting Material). Blue data indicates the counts per readout bin of $5\,\mu\text{s}$, and the deduced spin state is shown in orange.

To verify that these measurement outcomes indeed correspond to the electronic spin states, we use single-shot readout to observe spin Rabi oscillations and microwave-induced quantum jumps [25] (see Fig. 6.3a,c).

While the full readout optically pumps the spin, shorter readout durations can be non-

destructive, albeit at lower fidelity. By optimizing integration windows, we obtain a fidelity of $83.4 \pm 0.5\%$ for each of two successive readout segments (Fig. 6.3b). Correlations between measurement outcomes indicate that the readout is projective. Following preparation of a superposition of spin states, we condition on detection of at least one photon (i.e., measurement outcome $m_s = 0$) during a first short readout pulse, and probe the resulting spin state with a second readout (Fig. 6.3a, blue data points). Regardless of the initial spin state, we observe a constant high probability to obtain $m_s = 0$ in the second readout. This shows that the readout method is strongly projective and well suited for application in measurement-based quantum protocols.

6.4 Nuclear spin initialization by measurement

We exploit projective readout of the electron spin in combination with quantum gate operations for initialization and readout of a nuclear spin few-qubit register. We first demonstrate the concept of measurement-based preparation on a single nuclear qubit. The electronic spin resonance (ESR) spectrum for NV B (Fig. 6.4a, green trace) reveals the coupling to the host $I = 1$ ^{14}N nuclear spin: two partially overlapping sets of three hyperfine lines correspond to the $m_s = 0 \leftrightarrow -1$ and $m_s = 0 \leftrightarrow +1$ electronic spin transitions, Zeeman-split by $\sim 2\,\text{MHz}$ in the earth's magnetic field. The outermost transitions are associated with a specific nuclear spin state m_I, e.g. $(m_s, m_I) = (0, -1) \leftrightarrow (-1, -1)$ at $2.874\,\text{GHz}$. Our initialization procedure works as follows (Fig. 6.4a, circuit diagram): first, we prepare the electronic spin in $m_s = \pm 1$. We then perform a nuclear-spin-controlled NOT gate on the electronic spin by applying a π-pulse at $2.874\,\text{GHz}$; this operation rotates the electronic spin into $m_s = 0$ only when $m_I = -1$. Finally, we read out the electronic spin for $400\,\text{ns}$. If one or more photons are detected during this interval, the two-spin system is projected into $(m_s, m_I) = (0, -1)$. Alternatively, if we run the same protocol with initial electronic spin state $m_s = 0$, we prepare the nuclear spin into $m_I = \{0, +1\}$.

The efficiency of the nuclear spin initialization is evidenced by its dramatic effect on the ESR spectrum (Fig. 6.4a). Whereas before preparation the depths of the different hyperfine lines indicate an equal mixture of the nuclear spin states (green trace), after preparation only the hyperfine lines corresponding to the prepared states are visible ($m_I = -1$ for cyan trace and $m_I = \{0, +1\}$ for the orange trace).

The same nuclear spin initialization scheme can be applied to multi-qubit registers. Figure 6.4b displays the ESR spectrum of NV A (green trace), whose electronic spin is coupled to both the host ^{14}N nuclear spin and two nearby ^{13}C nuclei (see Supporting Material). The lowest-frequency line corresponds to a single state of the three nuclear spins. A π-pulse on this transition therefore implements a triple-controlled-NOT gate on the electronic spin (circuit diagram in Fig. 6.4b), enabling the initialization of all three nuclear spins (Fig. 6.4b, orange trace). The initialization can be further improved by repeating the preparation step (Fig. 6.4b, red data points).
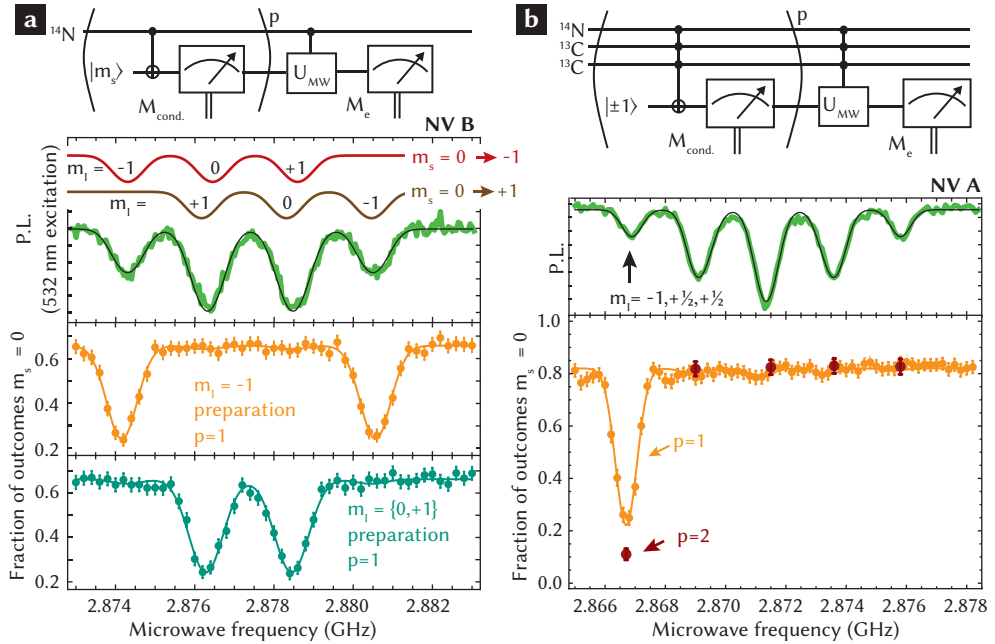
Figure 6.4 |Nuclear spin preparation. a, Measurement-based preparation of a single ^{14}N nuclear spin. In the ambient Earth magnetic field of ≈ 0.5 G, without nuclear spin polarization, we observe four resonances in the hyperfine spectrum (green trace) for NV B; the outer two correspond to the nuclear spin state $m_I = -1$ and the central two are combinations of $m_I = \{0, +1\}$. Circuit diagram: To initialize the nuclear spin we entangle it with the electronic spin and then read out the latter. Data for $m_I = -1$ preparation is shown in orange, preparation in $m_I = \{0, +1\}$ in cyan (below). Fits to Gaussian spectra show an amplitude ratio of $96 \pm 4\%$ in the desired nuclear spin state. **b**, Measurement-based preparation of a three nuclear spin register. Using a similar sequence (circuit diagram) we prepare a well-defined state for all three nuclear spins. A portion of the un-initialized hyperfine spectrum (green) contains 12 partially superposed lines, of which we prepare the single line corresponding to $m_I = (-1, \frac{1}{2}, \frac{1}{2})$ (orange, below). Gaussian fits constrained to known hyperfine splittings yield an amplitude ratio of $88 \pm 10\%$. The observed visibility can be improved by performing two preparation steps and electronic spin repumping ($p = 2$, five red data points), increasing the contrast to 82% of the expected visibility from known readout fidelity. Uncertainties and error bars are 2 SE (n = 1000 for **a, b**, $p = 1$; selected from 10000 measurement runs for **b**, $p = 2$).

6.5 Single-shot nuclear spin readout

The nuclear qubits can be read out in a single shot by applying a nuclear-controlled-NOT on the electronic spin and subsequently reading out the electronic spin (see Fig. 6.5a,b insets). Because the electronic spin measurement only has weak back-action on the nuclear spin, we can repeat the process to obtain higher readout fidelity[5,8]. Figure 6.5a compares the resulting photon statistics for NV B after initialization into the single nuclear spin state $m_I = -1$ to those obtained for $m_I = \{0, +1\}$, indicating an average readout fidelity of $92 \pm 2\%$. This number is a lower bound to the true readout fidelity, as it includes errors in the state preparation.

A straightforward extension of this scheme can be used to read out the complete state of a multi-nuclear-spin register. Using a multiply-controlled-NOT gate in the readout sequence, we can measure in a single shot whether the register is in a particular configuration. We demonstrate this procedure on NV A, where we identify the 3-nuclear-spin state $m_I = (-1, \frac{1}{2}, \frac{1}{2})$ (see Fig. 6.5b). The other possible configurations can be probed by sequential application of this readout scheme on different spectrally-resolved hyperfine transitions, or, alternatively, by systematically flipping the nuclear spin qubits and repeating the readout on the same hyperfine transition.
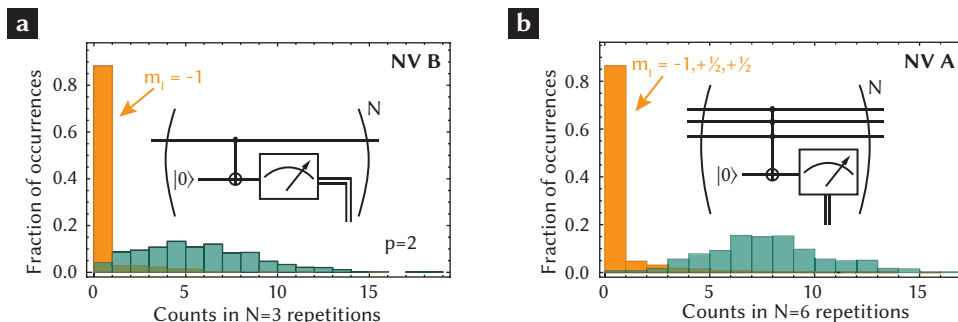
Figure 6.5 |Nuclear spin readout. a, Single-shot measurement of the ^{14}N nuclear spin, preceded by two preparation steps ($p = 2$). Readout (3 repetitions) conditioned on successful preparation distinguishes $m_I = -1$ (orange, threshold < 1 count) from $m_I = \{0, +1\}$ (cyan) with an average fidelity of $92 \pm 2\%$. **b**, Multiple nuclear spin readout. Using a similar sequence (inset) we distinguish one of the 12 hyperfine states associated with NV A. To prepare nuclear spin states, we perform the readout procedure 7 times and keep only data with zero total counts (identified as $(-1, \frac{1}{2}, \frac{1}{2})$) or ≥ 2 counts per initialization step (other states). Subsequent readout with 6 repetitions (($-1, \frac{1}{2}, \frac{1}{2}$) threshold < 3 total counts) achieves a $96.7 \pm 0.8\%$ average fidelity for preparation and detection of the nuclear spin configuration.

Electron-nuclear flip-flop processes in the optically excited state, which reduce the nuclear spin readout fidelity, pose a major hurdle for scaling the readout to more qubits. Critically, resonant readout allows selection of which states undergo optical excitation. By starting with the electronic spin in $m_s = \pm 1$, optical excitation will only occur when the register is in the state being probed; therefore, no optically-induced nuclear spin flips will occur during measurement of any of the other states. Thus, in contrast to schemes depending on off-resonant excitation where each additional readout step degrades the fidelity, resonant excitation enables scaling of high-fidelity readout to larger registers.

6.6 Initialization, control and single-shot readout of a quantum register

Finally, we demonstrate the compatibility of all the different techniques by implementing them in a single experiment: we initialize, coherently manipulate, and then read out a two-qubit register consisting of the electronic spin and ^{14}N nuclear spin of NV B. After initialization in $(m_s, m_I) = (0, -1)$, we rotate the nuclear spin using a radiofrequency (RF) pulse and subsequently rotate the electronic spin with a microwave (MW) pulse. We then read out the electronic spin, followed by readout of the ^{14}N nuclear spin state (Fig. 6.6a, circuit diagram). The left panel in Fig. 6.6a displays the readout results for the electronic spin qubit, showing the Rabi oscillations as a function of MW pulse length (vertical axis). In contrast, the readout results for the nuclear spin qubit (right panel of Fig. 6.6a) exhibit Rabi oscillations as a function of the RF pulse length (horizontal axis).

To quantify crosstalk, we closely examine correlations between the two measurement outcomes. We observe that the contrast in the electronic spin Rabi oscillations depends on the outcome of the nuclear readout (Fig. 6.6b), but this discrepancy can be fully accounted for by the finite MW power used in this experiment. The observed correlations thus arise from imperfect manipulation rather than measurement crosstalk. In the other direction, however, true measurement crosstalk appears: nuclear Rabi oscillation amplitudes decrease when the electronic spin is measured to be in $m_s = 0$ (Fig. 6.6c) because optical excitation during electronic spin readout (which only succeeds for $m_s = 0$) induces nuclear spin relaxation. This effect can be mitigated by improving the collection efficiency (thus reducing the readout duration), e.g. by integrating the NV centre in an optical cavity. Also, application of moderate magnetic fields can cut the optically-induced nuclear spin relaxation rate by orders of magnitude [5].
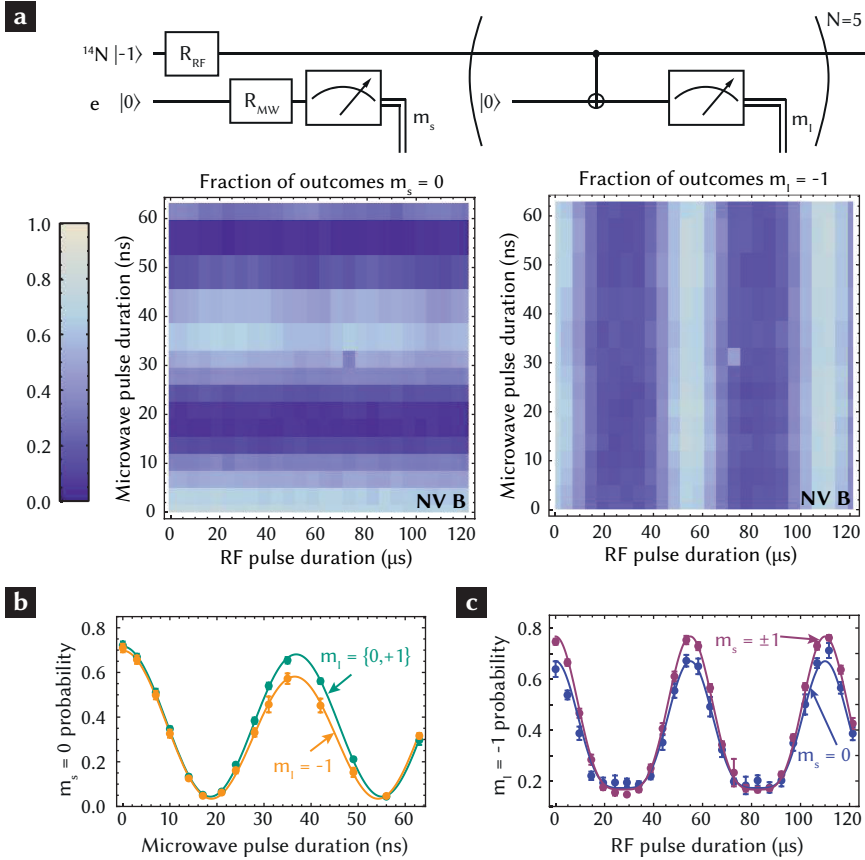
Figure 6.6 |Initialization, manipulation and readout of a two-qubit register. a, After initialization of NV B into $(m_s, m_I) = (0, -1)$, we use radio-frequency excitation (RF, 4.9464 MHz) to drive the nuclear spin and then microwaves (MW, 2.8774 GHz) to drive the electronic spin. The electronic spin state is subsequently measured for 15 μs, followed by 5 readout steps (each 10 μs) of the ^{14}N nuclear spin state. **b**, Probabilities to observe $m_s = 0$ conditional on the measured nuclear spin state and averaged over all RF pulse durations, as a function of MW pulse duration. **c**, Probabilities for observing $m_I = -1$ conditional on the observed electronic spin state and averaged over all MW pulse durations, as a function of RF pulse duration. All error bars and uncertainties are 2 SE; data based on 1000 measurements per pixel.

6.7 Outlook

Our results have implications for a broad range of spin-based applications. Single-shot electron spin readout can drastically improve NV-based sensors by enabling fast, quantum projection limited detection, creating opportunities in low-temperature magnetometry[31,32]. Extension of nuclear spin preparation techniques to remote nuclei in the spin bath may permit line-narrowing for enhanced sensitivity to d.c. magnetic fields. Furthermore, preparation, manipulation, and single-shot readout of two spins open the door to exploration of two-particle quantum correlations, such as Bell's inequalities, and elementary quantum information processing protocols. Importantly, the techniques we describe are extendable to larger spin registers, and can be combined with precise spin qubit control and dynamical decoupling for coherence protection[10–12]. The preparation and readout fidelities reported here are sufficient for demonstrating measurement-based entanglement generation and quantum teleportation of spin qubits, and exploring elementary quantum error correction schemes[1]. Ultimately, integration of multi-spin registers with quantum optical channels via spin-photon entanglement[13] may enable their application as few-qubit nodes in long-distance quantum communication protocols or distributed quantum information processing networks.

6.8   Supporting Material

6.8.1   Electron readout and initialization

Excited state structure

Single-shot readout via resonant excitation and fluorescence detection requires both high collection efficiency and a long-lived cycling transition. While we can enhance collection efficiency by nanofabrication of the diamond crystal, the degree of cycling of the optical transitions is set by the spin projections of the excited states, which in turn strongly depend on strain[26,33,34]. For strain in the range of $\delta \approx 0 - 10$ GHz, E_x has sufficiently low $m_s = \pm 1$ contribution to allow for single-shot readout (Fig. 6.7a). However, at $\delta \approx 3$ GHz, the spin splitting in the ground state equals the $E_x - A_1$ splitting, causing a spectral overlap of transitions coupling to $m_s = 0$ and $m_s = \pm 1$ and thus rendering optical pumping and resonant spin readout impossible. These restrictions limit the range of strain for which single-shot spin readout can be achieved.

Furthermore, at temperatures above around 10 K, phonon scattering in the excited state leads to a significant redistribution of population between E_x and E_y[29]. Because the E_y state exhibits a level anticrossing with the other ($m_s = \pm 1$) E states around 7 GHz strain, phonon mixing into E_y can dramatically shorten the spin flip time under optical excitation of E_x. Except for extremely low-strain NVs, low temperatures are thus critical to achieve high single-shot readout fidelity.
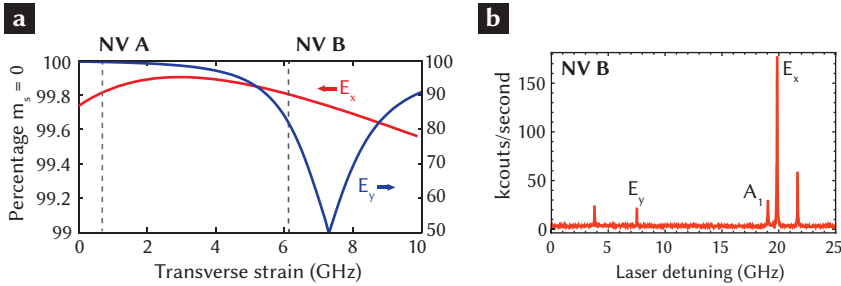
Figure 6.7 | Spin-mixing and energy-splitting dependent of strain. a, $m_s = 0$ projection of E_x and E_y excited states as function of transverse strain (following analysis in[33]). Values for the discussed NV centres are indicated. **b,** Photoluminescence excitation spectrum for NV B. Transitions to E_x and A_1 used in pulsed experiments are shown, along with the strain-split E_y transition 12.3 GHz below the E_x transition. Laser frequency is given as a detuning from 470.435 THz.
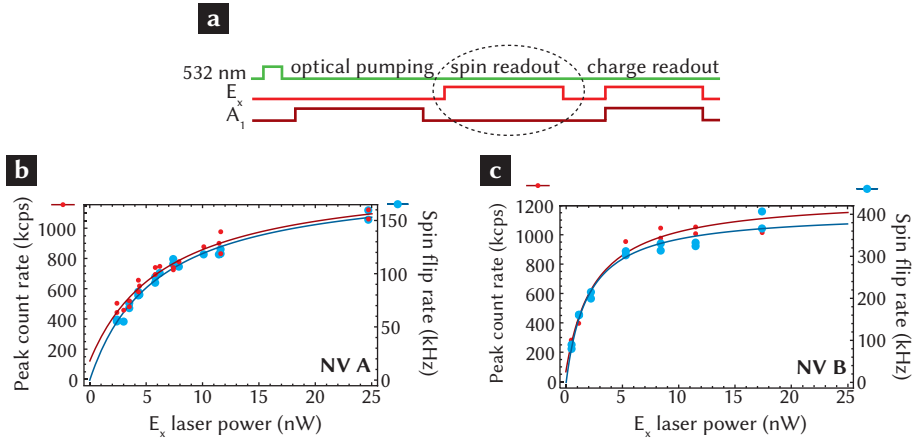
Figure 6.8 | Saturation under resonant excitation. a, Pulse sequence. Data shown in **b** and **c** is extracted from phonon sideband fluorescence during the spin readout pulse on the E_x transition. Data is conditioned on high count rates during the charge readout section to ensure that the NV centre transitions are close to resonance (i.e. using the first technique described in the text). **b,** Saturation curves for NV A. Each data point shows the maximum count rate obtained at the start of the fluorescence time trace (red) or spin relaxation rate obtained by fitting the fluorescence time trace to a single exponential (blue). Peak count rate and spin flip rate saturate as the laser power is increased, with similar saturation powers of 7 ± 4 nW and 5.9 ± 0.8 nW respectively. **c,** Saturation curves for NV B. Saturation powers from fit are 2.5 ± 1.2 nW and 1.9 ± 0.4 nW for peak count rate and spin flip rate respectively.

Comparison of NV A and NV B

The main text presents single-shot readout data for two NV centres, NV A and NV B. The approximate transverse strain for NV A and NV B is indicated in Fig. 6.7, and is found from half the splitting between the E_x and E_y transitions (see Fig. 6.1c in the main text and Fig. 6.7b) in the PLE spectra. While the E_x state itself exhibits a similar degree of spin-mixing at both strain values, phonon-induced transitions into E_y lead to increased spin-flip rates for NV B, for which E_y is significantly mixed with other spin states.

We can directly observe the different behavior of NV A and NV B under resonant excitation by examining the spin flip rate as a function of laser power. While higher peak count rates and lower saturation powers indicate a better SIL placement for NV B, strain leads to faster spin flip rates (see Fig. 6.8). Under resonant E_x excitation we thus do not detect very many photons from NV B (2.6 on average) before a spin flip occurs, leading to a less accurate single-shot readout than observed for NV A (see Fig. 6.9).

For both NV A and NV B, the average readout fidelity is primarily limited by the error in

reading out $m_s = 0$. Figure 6.9 shows the fidelity for $m_s = 0$ and $m_s = \pm 1$ readout individually as a function of the readout duration. The $m_s = 0$ fidelity grows with readout duration as we are more likely to detect a photon the longer we integrate; conversely, the $m_s = \pm 1$ fidelity decreases with readout duration owing to increased likelihood of background counts or off-resonantly induced spin flips (see discussion below of photon statistics). The optimal readout duration (maximizing average fidelity) represents the tradeoff between the two; its precise value depends sensitively on the power used to excite the readout transition, with shorter durations better at higher powers. Owing to increased background at higher powers, the best readout fidelities are achieved for readout laser intensity well below a saturation power.

Electronic spin preparation

To estimate the optical pumping efficiency for NV A, we examine the time dependence of the fluorescence during optical pumping. In particular, following nominal preparation into $m_s = 0$ ($m_s = \pm 1$), we fit the fluorescence time trace under E_x (A_1) excitation to a single exponential with an offset, $Ae^{-t/t_1} + B$ (see Fig. 6.1e of the main text); this yields information about the preparation fidelity into $m_s = \pm 1$ ($m_s = 0$). Owing to possibly imperfect preparation, the amplitude A of the exponential is less than or equal to the fluorescence rate that would result from a perfectly-prepared $m_s = 0$ ($m_s = \pm 1$) state. Because of background counts from ambient light and detector dark counts, the offset B is greater than or equal to the fluorescence rate from remaining undesired population in $m_s = 0$ ($m_s = \pm 1$) following optical pumping. The ratio $B/(A + B)$ is thus greater than or equal to the fraction of optically active population remaining in the $m_s = 0$ ($m_s = \pm 1$) state – in other words, an overestimate of error in optical pumping. The precise value of the preparation error depends on the laser intensity, but typical values (from e.g. data presented in Fig. 6.1e in the main text) are in the range of $0.35 \pm 0.06\%$ for $m_s = 0$ preparation and $0.8 \pm 0.1\%$ for $m_s = \pm 1$ preparation after subtraction of detector dark counts at 50 counts/second.

The above analysis neglects population of the singlet levels, which contributes a small bi-exponential character to the fluorescence decay[13]. Specifically, there is an initial fast decay as the singlet state is populated (leading to a steady state fraction of optically active population in the singlet states) followed by a slow decay as the spin relaxation occurs. Under the assumption that the fraction of optically active population in the singlet states remains constant after the initial fast decay, the relevant amplitude for estimating optical pumping efficiency is the amplitude of the slower decay. In the case of $m_s = \pm 1$ preparation the two exponentials can be fit, and yield an optical pumping error estimate of $0.7 \pm 0.1\%$ – equal, within uncertainty, to the simpler estimate above. The intersystem crossing to the singlets also explains the low count rates observed from excitation of the A1 transition. Current understanding suggests that the A1 excited state relaxes into the singlet states at a rate comparable to the radiative decay rate.[14,28] This decay rate is too fast to observe in our data, but it has an impact on the maximum count rates. Since decay out of the singlets is more than an order of magnitude slower than the radiative decay rate[28,35,36], the (non-fluorescing)
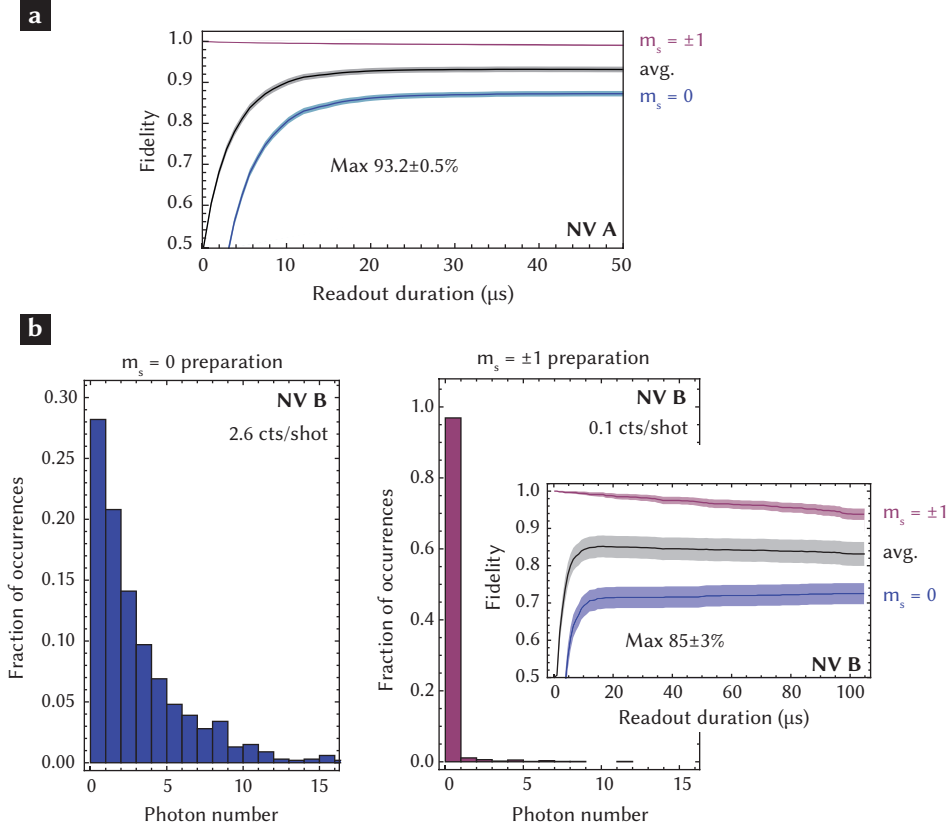
Figure 6.9 | Single-shot electron readout. a, Fidelity as a function of readout duration for NV A, analysis of data shown in Fig. 6.2a and b of the main text. The $m_s = \pm 1$ ($m_s = 0$) fidelity is calculated as the probability to identify the system as $m_s = \pm 1$ ($m_s = 0$) following optical pumping on transitions to the E_x (A_1) state. **b,** Photon count histograms (recorded during a 50 μs readout with 0.5 nW E_x excitation power) for NV B following optical pumping into the $m_s = 0$ (left) and $m_s = \pm 1$ (right) states. Inset shows fidelity as a function of readout duration. Shaded areas indicate the error margins.

equilibrium population in the singlets is significant, leading to the observed low fluorescence from A1 excitation.

We use these estimates of optical pumping efficiency to quantify spin polarization with green (532 nm) excitation. By comparing fluorescence statistics during readout after green initialization with those after A_1 initialization, we extract the fraction of $m_s = 0$ after green initialization to be 89 ± 3%. Resonant optical pumping thus decreases the error in spin preparation by more than a factor of 30.

Photon statistics during readout

The probability distribution of photon counts from electronic spin readout of the bright ($m_s = 0$) state is essentially set by three contributions: a) the spin flip rate γ_0, limiting the total number of scattered photons, which in the limit of long integration time ($t_{int} \gg \gamma_0^{-1}$) yields a geometric distribution of emitted photons, b) the photon detection efficiency, which selects emitted photons according to a binomial distribution, and c) low background counts following a Poissonian distribution. Given the few-percent collection efficiencies present in our setup, the expected distribution is very close to a geometric distribution, in agreement with our data.

While we can calibrate background counts (approximately 100 counts/second) from ambient light and detector dark counts, we observe a significantly higher fluorescence rate during readout after preparation into $m_s = \pm 1$ than would be expected solely from background. This fluorescence depends on the readout power and exhibits a geometric photon distribution; the autocorrelation of the background decays at the characteristic spin-flip rate. Since the averaged time trace of the background is flat, we attribute this fluorescence to laser-induced spin flips from $m_s = \pm 1$ to the bright $m_s = 0$ state during the readout. Such a process could occur, for example, through off-resonant excitation of the $m_s = \pm 1 \leftrightarrow A_1$ transition followed by spin mixing in the excited states or coupling to the singlets. This effect represents the dominant readout error of $m_s = \pm 1$, resulting in a decrease in average readout fidelity for increasing integration times (Fig. 6.9). Moreover, the same process limits the spin preparation fidelity for both spin states. As a consequence, we observe the highest optical pumping efficiencies and readout fidelities for excitation intensity well below saturation power.

Quantum jumps

Continuous resonant excitation of the $m_s = 0 \rightarrow E_x$ transition pumps the system into the dark $m_s = \pm 1$ state. To excite the spin out of this state, in Fig. 6.3c of the main text we apply weak MW repumping at 2.8715 GHz, resonant with the hyperfine transitions corresponding to four out of twelve nuclear spin configurations in NV A (see next section). Provided the nuclear spins are in one of those four configurations, the MW excitation drives the system back into the bright $m_s = 0$ state, enabling the observation of quantum jumps. We verify the effect of the MW by dividing a fluorescence time trace of 8 s duration into bins of 3.3 μs, and plotting average durations of bright and dark periods as function of MW power (Fig. 6.10).

To reduce the bias towards long dark periods due to non-driven nuclear spin states, we only include dark periods shorter than $100\,\mu s$ in this analysis (without this filter, we observe dark periods of up to 12 ms). We find that the duration of dark periods scales with the MW power, as expected for the rate of MW induced spin-flips $m_s = \pm1 \to m_s = 0$. The optical pumping rate from $m_s = 0 \to m_s = \pm1$ however is larger than the MW induced spin-flip rate, explaining the bright periods of $4.9\,\mu s$ average duration, independent of MW power. Although we do not provide a full quantitative model to this data, the dependence of dark period duration on MW power confirms that the observed intensity fluctuations can be attributed to a discrete evolution of the spin state.
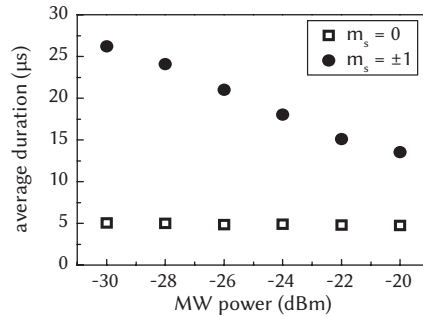
Figure 6.10 | Analysis of quantum jumps. Average duration of bright ($m_s = 0$) and dark ($m_s = \pm1$) periods in an 8 s fluorescence time trace of E_x excitation as function of power of MW excitation driving the spin transition (bin size $3.3\,\mu s$).

Projective readout and measurement based state preparation

An ideal quantum measurement would project an initial superposition state onto a spin eigenstate, reveal which projection occurs, and leave the system in the same eigenstate. In our system, projection of the spin happens either when the NV centre emits the first photon or, in the case of $m_s = \pm1$, as failure to emit a photon exponentially reduces the probability amplitude for occupation of the fluorescent state. While projection occurs on the timescale of a few optical cycles, the time required to detect a signal is considerably longer. As a result, there is a tradeoff between the fidelity with which we measure the projected spin state and the probability to leave it undisturbed, so that our readout only partially fulfills the requirements of ideal quantum measurement.

Nevertheless, a probabilistic preparation protocol that detects only $m_s = 0$ spin projections can be used to obtain both a high correlation between the projected and detected states and a low probability to flip the spin during measurement. Detection of a photon during a short readout pulse is very strongly correlated with an initial $m_s = 0$ spin projection (the error is given by 1-$F_{\pm1}$ in Fig. 6.9), and this correlation improves as the readout duration
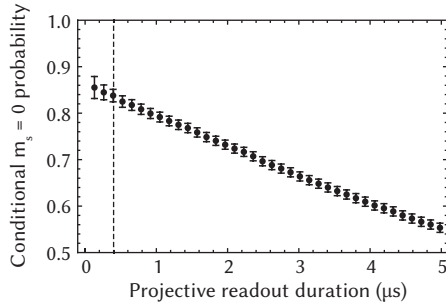
Figure 6.11 | Projective readout. Combining data for all microwave pulse durations shown in Fig. 6.3a of the main text, we show the probability to measure $m_s = 0$ during readout segment (2) after conditioning on detection of $m_s = 0$ during readout segment (1). The duration of the projective readout (1) is varied, while the duration of readout (2) is kept constant at 8.3 μs. The dashed line indicates the readout duration used in the projective state preparation for Fig. 6.3a of the main text (blue data points) and nuclear spin preparation.

decreases. Similarly, the probability to flip the spin during measurement vanishes in the limit of decreasing readout time.

To demonstrate high fidelity projective state preparation, we prepare a set of spin superpositions using microwaves (including all data from Fig. 6.3b of the main text), and perform two successive readouts. The first readout ((1), variable duration) projects the spin state, which we then detect during a second readout ((2), fixed duration 8.3μs). In Fig. 6.11 we show the conditional probability $P(0^{(2)}|0^{(1)})$ to measure $m_s = 0$ during the readout (2) conditioned on obtaining the outcome $m_s = 0$ in readout (1). As the first readout duration decreases, the conditional probability to measure $m_s = 0$ increases, approaching the bare $m_s = 0$ readout fidelity following optical pumping (87% for our best data sets, 82% for data taken under the same conditions as Fig. 6.3a main text). For short readout durations our measurement-based preparation is, within statistical uncertainties, indistinguishable from optical pumping into $m_s = 0$. Ultimately, in the limit of short readout duration the fidelity for preparation by measurement is constrained only by spin-mixing in the excited E_x state, which for low strain is less than 0.5%.

6.8.2 Hyperfine structure

The electronic spin associated with the nitrogen-vacancy centre in diamond couples to a variety of spins in its environment. While interactions with the bulk electronic[37] or nuclear[38] spin bath lead to dephasing and decoherence, the NV centre can interact coherently with sufficiently proximal nuclear spins[39]. In particular, the $I = 1$ ^{14}N (or $I = \frac{1}{2}$ ^{15}N) nuclear spin of the host nitrogen atom always couples to the NV centre spin, leading to a characteristic three- (or two-) line electron spin resonance (ESR) spectra with 2.166 MHz (3.03 MHz)[40,41]

splittings. Additionally, NV centres in natural isotopic concentration diamond can also interact strongly with $I = \frac{1}{2}$ ^{13}C nuclear spins located on nearby lattice sites; the resulting hyperfine structure depends critically on the locations of the nearest ^{13}C isotopic impurities. In this paper, we consider two NV centres with very different isotopic environments.

NV B does not couple strongly to any ^{13}C nuclei, though detailed electron spin resonance (ESR) scans do reveal weak (0.46 MHz) interactions with an isolated two-level system, likely also a ^{13}C nuclear spin. Because changes in the state of this weakly-coupled ^{13}C spin only slightly perturb NV B, we can address the electronic and ^{14}N nuclear spin states regardless of the other spin state. Indeed, the ESR spectra presented in the main text show no evidence of this spin because we use sufficient microwave power to drive ESR transitions unconditional on the ^{13}C spin state. Nevertheless, the presence of this extra spin limits the fidelity with which selective π pulses can drive a single ^{14}N hyperfine line.

In contrast, NV A exhibits significant hyperfine interactions with two ^{13}C isotopic impurities. Combined with hyperfine structure from the host ^{14}N nuclear spin, these interactions lead to a complex ESR spectrum where each line corresponds to one or more of the twelve nuclear spin states. We identify the spins as ^{13}C nuclear spins by comparison of measured hyperfine splittings to known ^{13}C interaction strengths[42] and verification of expected coherent dynamics in electron spin echo envelope modulation measurements[39]. Because of the small electronic Zeeman splitting in Earth's magnetic field, there is some redundancy in the ESR spectrum, and all of the nuclear spin states are contained in half of the spectrum. We indicate in detail which nuclear spin configurations contribute to the observed lines in the lower half of the spectrum (shown in Fig. 6.4b of the main text), using positive values for the hyperfine interaction for the ^{13}C nuclear spins[42] and a negative value for the ^{14}N nuclear spin[41]. To demonstrate nuclear spin preparation it thus suffices to examine half of the lines, and show that a line corresponding to a single 3-nuclear-spin configuration (here labelled transition 1) is enhanced at the expense of the others.

Transition	1		2			3				4			5
^{14}N:	-1		-1	0	1	1	0	1	0	-1	0	1	-1
^{13}C:	½		-½	½	-½	½	-½	½	-½	-½	½	-½	½
^{13}C:	½		½	½	-½	½	½	-½	-½	-½	-½	½	-½
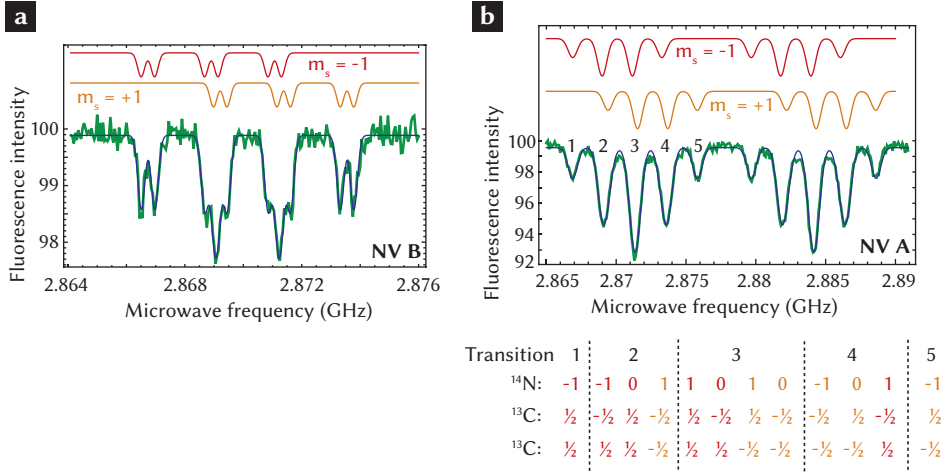
Figure 6.12 | Hyperfine spectra. a, ESR for NV B in ambient magnetic field. ESR data are recorded without nuclear preparation and using standard green excitation for the spin detection, for which the fluorescence intensity is a proxy for the polarization of the electronic spin into $m_s = 0$. Microwaves are applied in a 5 μs pulse with a Rabi frequency of approximately 100 kHz prior to fluorescence detection of the electronic spin. Upper traces illustrate the contributions from transitions to the $m_s = +1$ and $m_s = -1$ branches as determined by a fit to 12 Gaussian components constrained to have the same amplitude, with positions determined by two two-fold (Zeeman and ^{13}C) splittings and one three-fold (^{14}N) splitting. Hyperfine parameters extracted from the fit are: 2.169(7) MHz for ^{14}N and 0.46(1) MHz for ^{13}C. **b,** ESR for NV A in ambient magnetic field. Separate contributions from $m_s = \pm 1$ transitions are illustrated above using components of the fit to 24 Gaussian lines constrained to have the same amplitude, with three two-fold (Zeeman and two ^{13}C) splittings and one three-fold (^{14}N) splitting. Hyperfine parameters extracted from the fit are: 2.18(3) MHz for ^{14}N, 2.53(4) MHz for the first ^{13}C and 12.78(1) MHz for the second ^{13}C. Transitions 1-5 marked on the plot correspond to nuclear spin configurations tabulated in columns below. Numbers $-1, 0, 1$ indicate the projection of the ^{14}N nuclear spin on the NV axis, while $\pm \frac{1}{2}$ indicates the projections of the ^{13}C nuclear spins on their respective principal hyperfine axes.

6.9 Bibliography

[1] A. N. Nielsen and I. L. Chuang. *Quantum Computation and Quantum Information.* Cambridge University Press (2000).

[2] R. Raussendorf, D. E. Browne and H. J. Briegel. Measurement-based quantum computation on cluster states. *Physical Review A* **68**, 022312 (2003).

[3] J. M. Elzerman *et al.* Single-shot read-out of an individual electron spin in a quantum dot. *Nature* **430**, 431 (2004).

[4] A. N. Vamivakas *et al.* Observation of spin-dependent quantum jumps via quantum dot resonance fluorescence. *Nature* **467**, 297 (2010).

[5] P. Neumann *et al.* Single-Shot Readout of a Single Nuclear Spin. *Science* **329**, 542 (2010).

[6] A. Morello *et al.* Single-shot readout of an electron spin in silicon. *Nature* **467**, 687 (2010).

[7] G. Giedke, J. M. Taylor, D. D'Alessandro, M. D. Lukin and A. Imamoglu. Quantum measurement of a mesoscopic spin ensemble. *Physical Review A* **74**, 032316 (2006).

[8] L. Jiang *et al.* Repetitive Readout of a Single Electronic Spin via Quantum Logic with Nuclear Spin Ancillae. *Science* **326**, 267 (2009).

[9] G. Balasubramanian *et al.* Ultralong spin coherence time in isotopically engineered diamond. *Nature Materials* **8**, 383 (2009).

[10] B. Naydenov *et al.* Dynamical decoupling of a single-electron spin at room temperature. *Physical Review B* **83**, 081201 (2011).

[11] G. de Lange, Z. H. Wang, D. Riste, V. V. Dobrovitski and R. Hanson. Universal Dynamical Decoupling of a Single Solid-State Spin from a Spin Bath. *Science* **330**, 60 (2010).

[12] C. A. Ryan, J. S. Hodges and D. G. Cory. Robust Decoupling Techniques to Extend Quantum Coherence in Diamond. *Physical Review Letters* **105**, 200402 (2010).

[13] E. Togan *et al.* Quantum entanglement between an optical photon and a solid-state spin qubit. *Nature* **466**, 730 (2010).

[14] A. Batalov *et al.* Temporal Coherence of Photons Emitted by Single Nitrogen-Vacancy Defect Centers in Diamond Using Optical Rabi-Oscillations. *Physical Review Letters* **100**, 77401 (2008).

[15] B. B. Buckley, G. D. Fuchs, L. C. Bassett and D. D. Awschalom. Spin-Light Coherence for Single-Spin Measurement and Control in Diamond. *Science* **330**, 1212 (2010).

[16] L. Robledo, H. Bernien, I. van Weperen and R. Hanson. Control and Coherence of the Optical Transition of Single Nitrogen Vacancy Centers in Diamond. *Physical Review Letters* **105**, 177403 (2010).

[17] L. Childress, J. M. Taylor, A. S. Sørensen and M. D. Lukin. Fault-Tolerant Quantum Communication Based on Solid-State Photon Emitters. *Physical Review Letters* **96**, 070504 (2006).

[18] S. Barrett and P. Kok. Efficient high-fidelity quantum computation using matter qubits and linear optics. *Physical Review A* **71**, 060310 (2005).

[19] L. Jiang, J. M. Taylor and M. D. Lukin. Fast and robust approach to long-distance quantum communication with atomic ensembles. *Physical Review A* **76**, 012301 (2007).

[20] M. V. G. Dutt *et al.* Quantum Register Based on Individual Electronic and Nuclear Spin Qubits in Diamond. *Science* **316**, 1312 (2007).

[21] P. Neumann *et al.* Multipartite entanglement among single spins in diamond. *Science* **320**, 1326 (2008).

[22] G. D. Fuchs *et al.* Excited-State Spectroscopy Using Single Spin Manipulation in Diamond. *Physical Review Letters* **101**, 117601 (2008).

[23] V. Jacques *et al.* Dynamic Polarization of Single Nuclear Spins by Optical Pumping of Nitrogen-Vacancy Color Centers in Diamond at Room Temperature. *Physical Review Letters* **102**, 057403 (2009).

[24] W. Happer. Optical Pumping. *Reviews of Modern Physics* **44**, 169 (1972).

[25] R. Blatt and P. Zoller. Quantum jumps in atomic systems. *European Journal of Physics* **9**, 250 (1988).

[26] P. Tamarat *et al.* Spin-flip and spin-conserving optical transitions of the nitrogen-vacancy centre in diamond. *New Journal of Physics* **10**, 045004 (2008).

[27] M. Atature. Quantum-Dot Spin-State Preparation with Near-Unity Fidelity. *Science* **312**, 551 (2006).

[28] N. B. Manson, J. P. Harrison and M. Sellars. Nitrogen-vacancy center in diamond: Model of the electronic structure and associated dynamics. *Physical Review B* **74**, 104303 (2006).

[29] K.-M. C. Fu *et al.* Observation of the Dynamic Jahn-Teller Effect in the Excited States of Nitrogen-Vacancy Centers in Diamond. *Physical Review Letters* **103**, 256404 (2009).

[30] J. P. Hadden *et al.* Strongly enhanced photon collection from diamond defect centers under microfabricated integrated solid immersion lenses. *Applied Physics Letters* **97**, 241901 (2010).

[31] C. L. Degen. Scanning magnetic field microscope with a diamond single-spin sensor. *Applied Physics Letters* **92**, 243111 (2008).

[32] J. M. Taylor *et al.* High-sensitivity diamond magnetometer with nanoscale resolution. *Nature Physics* **4**, 810 (2008).

[33] M. W. Doherty, N. B. Manson, P. Delaney and L. C. L. Hollenberg. The negatively charged nitrogen-vacancy centre in diamond: the electronic solution. *New Journal of Physics* **13**, 025019 (2011).

[34] J. R. Maze *et al.* Properties of nitrogen-vacancy centers in diamond: the group theoretic approach. *New Journal of Physics* **13**, 025025 (2011).

[35] V. M. Acosta, A. Jarmola, E. Bauch and D. Budker. Optical properties of the nitrogen-vacancy singlet levels in diamond. *Physical Review B* **82**, 201202 (2010).

[36] L. Robledo, H. Bernien, T. van der Sar and R. Hanson. Spin dynamics in the optical cycle of single nitrogen-vacancy centres in diamond. *New Journal of Physics* **13**, 5013 (2011).

[37] R. Hanson, V. V. Dobrovitski, A. E. Feiguin, O. Gywat and D. D. Awschalom. Coherent Dynamics of a Single Spin Interacting with an Adjustable Spin Bath. *Science* **320**, 352 (2008).

[38] J. R. Maze, J. M. Taylor and M. D. Lukin. Electron spin decoherence of single nitrogen-vacancy defects in diamond. *Physical Review B* **78**, 94303 (2008).

[39] L. Childress *et al.* Coherent Dynamics of Coupled Electron and Nuclear Spin Qubits in Diamond. *Science* **314**, 281 (2006).

[40] M. Steiner, P. Neumann, J. Beck, F. Jelezko and J. Wrachtrup. Universal enhancement of the optical readout fidelity of single electron spins at nitrogen-vacancy centers in diamond. *Physical Review B* **81**, 35205 (2010).

[41] S. Felton *et al.* Hyperfine interaction in the ground state of the negatively charged nitrogen vacancy center in diamond. *Physical Review B* **79**, 75203 (2009).

[42] B. Smeltzer, L. Childress and A. Gali. 13C hyperfine interactions in the nitrogen-vacancy centre in diamond. *New Journal of Physics* **13**, 025021 (2011).

Two-photon quantum interference from separate nitrogen vacancy centers in diamond

H. Bernien, L. Childress, L. Robledo, M. Markham, D. Twitchen, and R. Hanson

We report on the observation of quantum interference of the emission from two separate nitrogen vacancy (NV) centers in diamond. Taking advantage of optically induced spin polarization in combination with polarization filtering, we isolate a single transition within the zero-phonon line of the non-resonantly excited NV centers. The time-resolved two-photon interference contrast of this filtered emission reaches 66%. Furthermore, we observe quantum interference from dissimilar NV centers tuned into resonance through the dc Stark effect. These results pave the way towards measurement-based entanglement between remote NV centers and the realization of quantum networks with solid-state spins.

7.1 Introduction

The nitrogen vacancy (NV) center in diamond is an attractive candidate for construction of quantum networks[1–3]. It is a highly stable single photon emitter[4], whose optical transitions are linked[5] to a long-lived electronic spin with excellent coherence properties[6]. The electronic spin can be coherently manipulated with high fidelity with pulsed microwave fields[7,8]. By extending these techniques to proximal nuclear spins, a controllable multi-qubit quantum register can be realized[9–11].

Optical schemes based on photon interference provide a way to establish quantum interactions over a distance. When two photons that are indistinguishable simultaneously impinge on a beamsplitter they coalesce into the same output port[12]. If these two photons are each entangled with the spin of the emitter, their interference can be exploited to generate entanglement between two distant emitters[13–15]. This type of measurement-based entanglement has recently been achieved between two remote single ions[16]. While spin-photon entanglement has been realized using NV centers[5], two-photon quantum interference (TPQI) with NV centers has so far not been observed.

Here we capitalize on recent advances in the understanding of the NV center's excited states[17–22] and a drastic improvement of the photon collection efficiency[11,23], and demonstrate TPQI from two separate NV centers. Furthermore, we show that even dissimilar NV centers can exhibit TPQI when their emission lines are brought into resonance using dc Stark tuning[22,24]. This latter technique greatly facilitates a scaling to larger networks.

7.2 Experimental methods

We perform our experiments on naturally occurring NV centers in high purity type IIa chemical-vapor deposition grown diamond[25] with a $\langle 111 \rangle$ crystal orientation obtained by cleaving a $\langle 100 \rangle$ substrate. Because a TPQI measurement involves coincidence detection of photons emitted from two centers, high collection efficiency is essential. To this end, we deterministically fabricate solid immersion lenses (SILs)[23,26] around preselected centers by focused ion beam milling. Figure 7.1a shows an optical microscope image of the device being used; the inset is an SEM picture of a similar device. In the confocal scans (Fig. 7.1b) the NV centers appear as bright spots inside the lenses. To enable spin manipulation and Stark tuning of the optical transition energies, we lithographically define a gold microwave stripline and gates around the SILs. A dual path confocal setup allows us to individually address two NV centers within the same diamond (Fig. 7.1c). The sample is mounted inside a flow cryostat and experiments are performed at a temperature of 9 K.
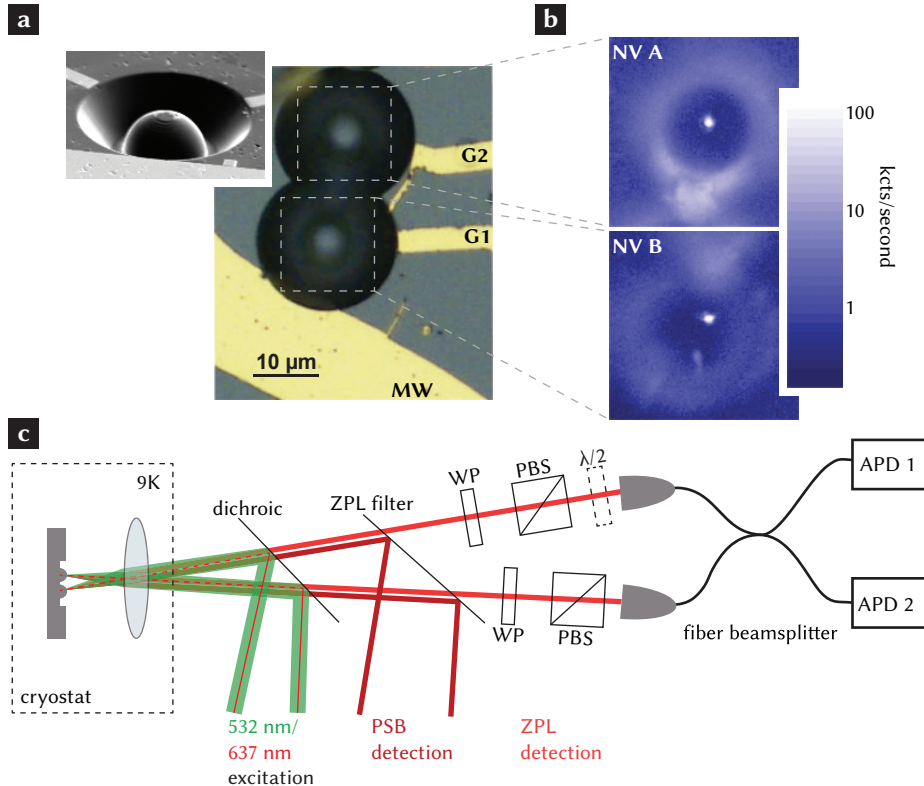
Figure 7.1 | Device and experimental setup. a, Optical microscope image of the sample. The microwave stripline (MW) is used for spin manipulation and the gates (G1 and G2) are used for Stark tuning of the optical transition energies. Inset: SEM picture of a similar device. **b,** Confocal microscope image showing NV A and NV B (logarithmic color scale). **c,** Experimental setup. The two NV centers inside the same diamond are simultaneously excited with either a resonant (637 nm) or an non-resonant (532 nm) laser. Two separate paths allow detection of photons emitted into the zero phonon line (ZPL) or the phonon side band (PSB). A variable retardance waveplate (WP) aligns the polarization of the desired transition to the polarizing beamsplitter (PBS) while compensating for ellipticity introduced by other optical components.

7.3 Spectral properties of single NV centers

The optical emission spectrum of the NV center (Fig. 7.2a) consists of both direct transitions between the ground and the excited state (the so-called zero phonon line, ZPL, that contributes 4% to the total emission) and transitions that additionally involve the emission of phonons (phonon side band, PSB). At low temperatures, the ZPL emission spectrum exhibits several narrow lines which, for low-strain centers, correspond to spin selective transitions between the ground and excited state [17,18]. Observation of TPQI requires indistinguishable photons which we produce by isolating a single transition within the ZPL. Appropriate band-pass filters remove the incoherent fraction of the emission (PSB). Non-resonant excitation, as used in this experiment, polarizes the NV electronic spin into the $m_s = 0$ state, hence only transitions between the E_x and E_y excited states ($m_s = 0$) and the $m_s = 0$ ground state level occur. The dipoles associated with these two transitions are orthogonal to each other and to the N-V axis; by working with NV centers oriented along the $\langle 111 \rangle$ direction we ensure that collected ZPL photons remain linearly polarized, with orthogonal polarizations for E_x and E_y [20,21]. Consequently, for a center that is spin-polarized into $m_s = 0$, we can isolate the E_x or E_y emission line by placing a polarizer in the detection path. Furthermore, we maximize the signal by using the polarization selectivity to excite predominantly one dipole.

To characterize the ZPL fine structure, we use photoluminescence excitation (PLE) to probe the ZPL absorption spectrum and a scanning Fabry-Perot (FP) cavity to analyze the ZPL emission spectrum. PLE spectra are obtained by sweeping the frequency of the resonant excitation laser (637 nm, Fig. 7.1c) across the ZPL transitions while recording the red-shifted emission into the PSB. During PLE scans, we ensure the correct charge state and visibility of the $m_s = 0$ transitions by simultaneous weak green excitation [27]. Figure 7.2b shows the PLE spectra of the two selected emitters. While the lower-energy E_y transitions are 2.9 GHz apart from each other, the higher-energy E_x transitions partly overlap. This near-overlap is also observed by using a scanning Fabry-Perot cavity to monitor the ZPL emission under non-resonant (532 nm) excitation (Fig. 7.2c). By setting the filters to transmit only the linearly polarized light associated with the E_x transitions, we observe a single emission line from each NV center with nearly equal frequencies.

Inhomogeneous broadening of the emission linewidths will limit the observability of quantum interference [28]. For individual PLE scans, obtained in the absence of green light, we find narrow 38±7 MHz (36 ± 5 MHz) linewidths for NV A (NV B); however, a 532 nm repump pulse between scans leads to an overall distribution of frequencies with an inhomogeneous linewidth of 263 ± 6 MHz for NV A and 483 ± 5 MHz for NV B [21,29]. The same spectral diffusion is observed in PLE spectra recorded with simultaneous green excitation (Fig. 7.2b) and in the ZPL emission spectrum under 532 nm excitation (Fig. 7.2c). Although the observed inhomogeneous broadening exceeds the radiative linewidth by an order of magnitude, two-photon interference effects can still be detected. Provided that the emission linewidth does not exceed the inverse time resolution of the photon detectors, simultaneous detection of a photon from each NV center erases the which-path frequency information, allowing quantum interference to be observed [30,31].
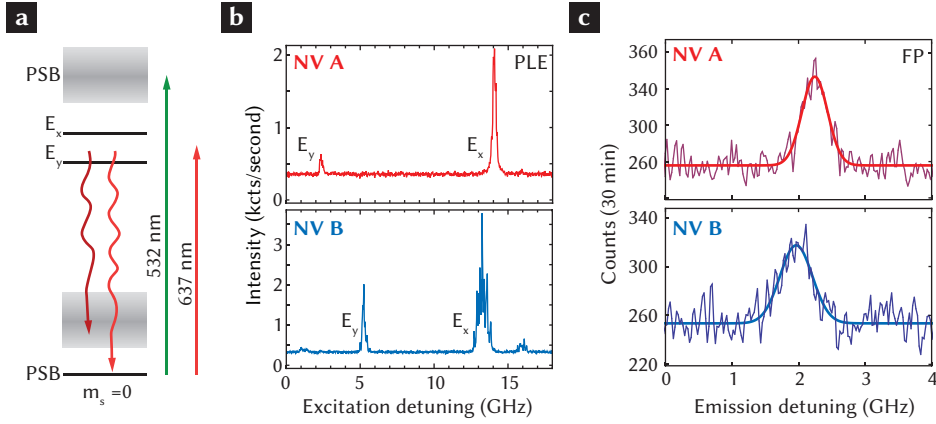
Figure 7.2 | Spectral characterization of NV A and NV B. a, Level structure. The $m_s = 0$ ground state is connected via spin selective transitions to the E_x and E_y ($m_s = 0$) excited state, $m_s = \pm 1$ states are omitted for clarity. Photons that are emitted into the phonon side band (PSB) can be spectrally separated from resonant emission. Also shown are the resonant (637 nm) and the non-resonant laser (532 nm). **b,** Resonant excitation of the ZPL and detection of the PSB. The frequency of the red laser is swept across the resonances while weak green excitation prevents photoionization and optical pumping (see text). The spectra are averaged over 70 scans. **c,** Scanning Fabry-Perot spectrum under non-resonant excitation. Only the E_x transition is visible confirming sufficient suppression of the E_y transition by polarization filtering. The linewidths (450 MHz for NV A and 570 MHz for NV B) include drifts of the cavity during the measurement. The offset is due to detector dark counts.

7.4 Two-photon quantum interference

For the interference measurement, we employ a green (532 nm) pulsed laser (62 ps) with a repetition frequency of 10 MHz both to excite the two NV centers and to initialize the spin state into $m_s = 0$. A combination of spectral filtering (ZPL filter) and polarization rejection (as discussed above) isolates the E_x lines of NV A and B. This emission is then coupled into the two input ports of a polarization-maintaining fiber beamsplitter, ensuring excellent spatial mode overlap. We establish temporal mode overlap by using equidistant excitation and collection paths for the two centers. The output ports of the beam splitter are connected to two avalanche photo diodes (APDs) with sub-ns time resolution; the APD signals trigger the start and the stop of a fast counting module whose jitter is less than 12 ps. By recording the coincidence counts as a function of start-stop delay, we perform a time-resolved measurement.
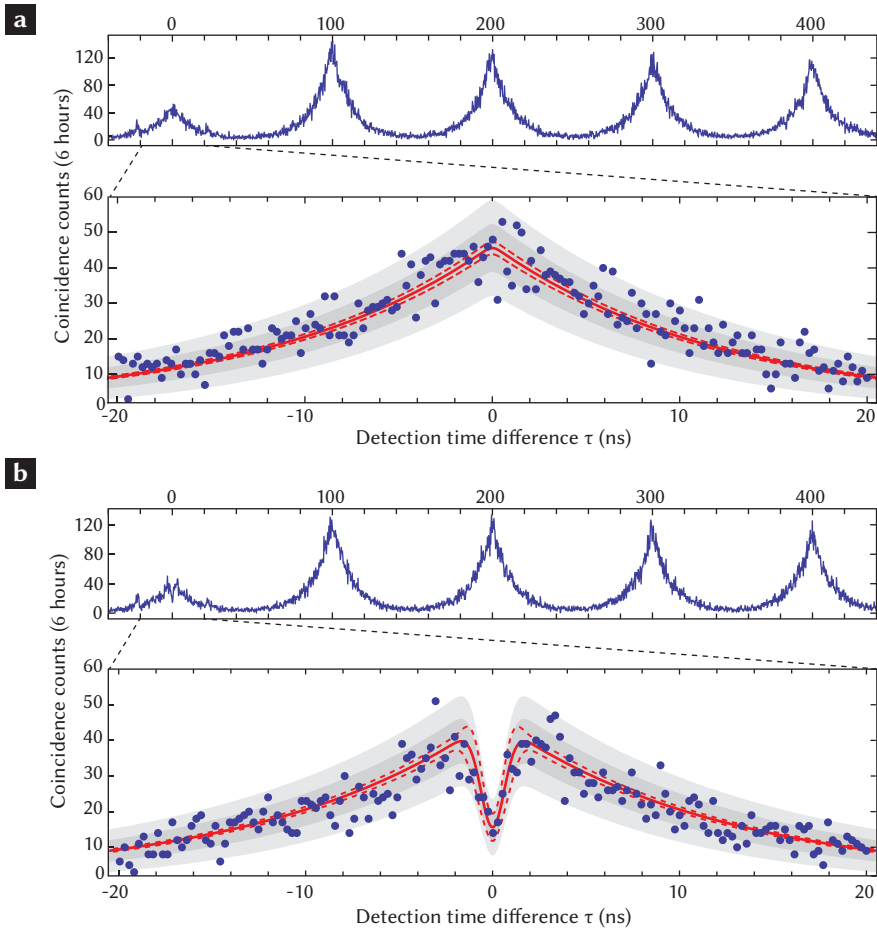
Figure 7.3 | Two-photon quantum interference. a, Orthogonal polarization. Periodic peaks of the coincidence counts correspond to the 10 MHz repetition frequency of the excitation. The coincidence distribution shows typical bunching and anti-bunching features of the two independent NV centers under pulsed excitation[32]. **b,** Parallel polarization. Interference of indistinguishable photons leads to a significant decrease in coincidence events at zero time delay. Simulations (red line) using only independently measured parameters are done according to Legero et al.[28]. The dashed lines show 1 standard error uncertainty in the simulation. The dark and light grey areas illustrate 1 and 2 standard deviations expected scatter. Parameters used for the simulations are: excited state lifetime = 12.0±0.4 ns, detuning between the two centers = 130±150 MHz, frequency jitter between them = 550±80 MHz, APD jitter = 410±10 ps, dark count rate = 60±10 s^{-1}, NV B count rate = 1470±50 s^{-1}, NV A count rate = 2700±50 s^{-1}, background = 15±5 %.

As a calibration experiment, we insert a $\lambda/2$ wave plate into one detection path (Fig. 7.1c) so that the two photons entering the beamsplitter have orthogonal polarization. This makes the two photons distinguishable and no interference can be observed. Therefore the coincidence distribution only reveals the temporal overlap of two independent photon wave packets (see Fig. 7.3a). The situation changes dramatically when the photons enter the beamsplitter with parallel polarization (Fig. 7.3b). For this case two-photon quantum interference is observed: around zero detection time difference ($\tau = 0$) the two photons mainly leave the beamsplitter into the same output port, leading to a significant reduction in coincidence detections. For larger time differences interference is concealed because of averaging over many photons with different frequencies [28]. We thereby observe TPQI as a reduction in coincidence detection events within a time window given by the inverse of the inhomogeneous emission linewidth.

In principle, full visibility interference can be observed even for inhomogeneously broadened and detuned photon sources at the cost of a reduced width of the interference dip [30]. The observed contrast at $\tau = 0$ is limited primarily by NV emission into undesired spectral lines owing to imperfect control over the charge and spin state of the center. Specifically, when the center is in the neutral charge state (NV^0), a portion of its broadband fluorescence lies within the 3 nm bandwidth of our ZPL filters; from independently measured optical spectra, these NV^0 photons contribute approximately 10% to the collected emission. Furthermore, under 532 nm excitation a residual $\sim$10% $m_s = \pm 1$ spin occupation [11] produces circularly polarized emission on several other transitions, contributing $\sim$5% of our polarization-filtered signal. From such a 15% background level we expect at most 72% visibility. Furthermore, finite time resolution in our detection system will average over sharp temporal features, raising the depth of the zero-time-difference minimum.

We observe a quantitative agreement between our data and no-free-parameter simulations of the experiment. Following Legero et al. [28], we model TPQI of exponentially decaying photon wavepackets with gaussian frequency noise and calculate the expected coincidence detections using independently measured parameters. At $\tau = 0$ we observe a contrast of 66±10% which is to our knowledge the highest value reported for two separate solid-state emitters [31,33–35]. This value can be improved by more stringent filtering of the ZPL emission or by increased control over the spin and charge states. We note that for measurement-based entanglement, the visibility determines the fidelity while the width of the interference dip sets the success probability of the entanglement operation.

7.5 Interference of dissimilar sources

To observe TPQI, we selected NV centers with nearly identical E_x frequencies; in general, however, because of their different strain environments, two NV centers are unlikely to exhibit the same emission frequencies [19,36]. Even in high purity type IIa samples, we typically observe a spread of tens of GHz between different centers. Nevertheless, NVs can be tuned into resonance by applying electrical fields to induce dc Stark shifts of the transition energies [24]. The tuning range of our devices reaches several GHz and is enhanced to tens of
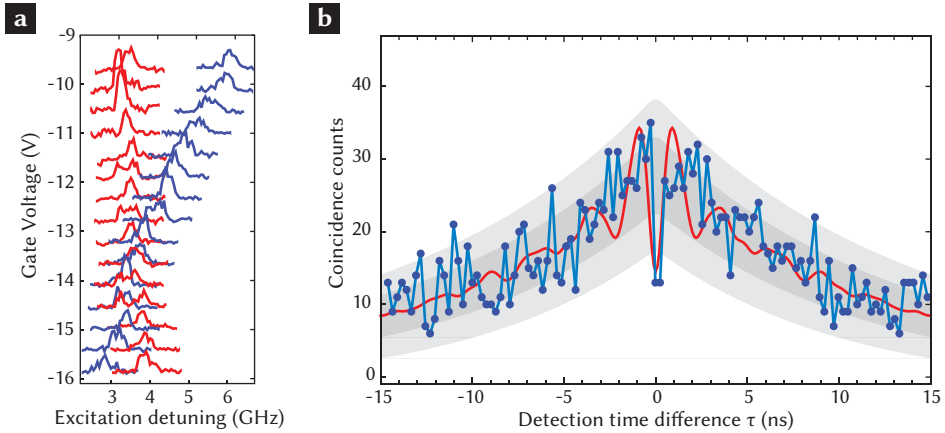
Figure 7.4 | Interference of two dissimilar sources. a, E_y transition energy as a function of applied gate voltage. The two centers show opposite tuning behavior and are brought into resonance at -13.6V. Data is taken under simultaneous green excitation with the same power that is used for the interference measurement. **b,** Two-photon quantum interference. The overall coincidence distribution is the sum of 255 one-minute histograms. Before each interference measurement we perform a PLE scan. We select only histograms for which the relative detuning of the two centers is between 350 and 1200 MHz. The simulation (red line) is based on the measured frequency distribution and shows oscillations that reflect the discrete set of detuning values. The dark and light grey areas illustrate the expected signal for two non-interfering sources with 1 and 2 standard deviations respectively.

GHz in the presence of 532 nm excitation[22]. This enables us to observe TPQI in the general case of dissimilar sources.

In the absence of an external voltage bias, the E_y transitions of NV A and NV B lie far apart in energy so that their TPQI cannot be measured within the time resolution of our detectors. By applying a voltage to gate 1 (Fig. 7.1a) while keeping the microwave stripline and gate 2 on ground, we can tune the E_y transitions into resonance. Because the degree of tuning is strongly affected by the presence of non-resonant excitation[22], we calibrate the Stark tuning under the same pulsed 532 nm excitation conditions as used for the interference measurement: the PLE spectra in Fig.7.4a show the additional fluorescence induced by resonant excitation, revealing the spectral location of the E_y line. Near -13.6 V, we observe overlapping transition energies for the two NV centers, establishing the appropriate setting for observation of TPQI. In addition to shifting the energy of the NV center transitions, applied electric fields can also rotate the axes of the E_x and E_y dipoles; we find that significantly different polarization settings are required to filter the E_y emission at this gate voltage.

Using the calibrated voltage and polarization settings, we measure the time-resolved

interference of photons emitted on the E_y transitions from each NV center. Figure 7.4b shows a significant decrease in coincidence detection events at zero time difference. The width of the interference signal is smaller than what would be expected from earlier measurements of the inhomogeneous linewidth of the emitters. Because the laser intensity changes the effective Stark shift, a drift in sample position directly translates into a spectral shift. To account for the spectral variations, we perform the measurement by alternating PLE spectroscopy and minute-duration coincidence detection, and post-select the data based on their relative detunings. We find our data to agree with a simulation based on the measured frequency distribution (red line in Fig. 7.4b). In contrast, a model without TPQI (shaded area in Fig. 7.4b) fails to reproduce the observed drop in coincidences around $\tau = 0$. Increased control over spatial and laser power fluctuations is expected to greatly enhance the interference contrast in the presence of gate voltage tuning.

7.6 Conclusions

We have demonstrated two-photon quantum interference with separate NV centers in diamond. The observed contrast can be further improved through resonant excitation, which eliminates photon emission from the incorrect charge and spin states. Moreover, the coincidence rates may be enhanced by embedding NV centers into optical cavities [37,38]. When combined with recently-demonstrated spin-photon entanglement [5], our results enable remote entanglement of NV centers, and open the door to applications in quantum information processing and long distance quantum communication.

7.7 Bibliography

[1] H. J. Briegel, W. Dür, J. I. Cirac and P. Zoller. Quantum Repeaters: The Role of Imperfect Local Operations in Quantum Communication. *Physical Review Letters* **81**, 5932 (1998).

[2] H. J. Kimble. The quantum internet. *Nature* **453**, 1023 (2008).

[3] L. Childress, J. M. Taylor, A. S. Sørensen and M. D. Lukin. Fault-Tolerant Quantum Communication Based on Solid-State Photon Emitters. *Physical Review Letters* **96**, 070504 (2006).

[4] C. Kurtsiefer, S. Mayer, P. Zarda and H. Weinfurter. Stable Solid-State Source of Single Photons. *Physical Review Letters* **85**, 290 (2000).

[5] E. Togan *et al.* Quantum entanglement between an optical photon and a solid-state spin qubit. *Nature* **466**, 730 (2010).

[6] G. Balasubramanian *et al.* Ultralong spin coherence time in isotopically engineered diamond. *Nature Materials* **8**, 383 (2009).

[7] F. Jelezko, T. Gaebel, I. Popa, A. Gruber and J. Wrachtrup. Observation of Coherent Oscillations in a Single Electron Spin. *Physical Review Letters* **92**, 76401 (2004).

[8] G. de Lange, Z. H. Wang, D. Riste, V. V. Dobrovitski and R. Hanson. Universal Dynamical Decoupling of a Single Solid-State Spin from a Spin Bath. *Science* **330**, 60 (2010).

[9] M. V. G. Dutt *et al.* Quantum Register Based on Individual Electronic and Nuclear Spin Qubits in Diamond. *Science* **316**, 1312 (2007).

[10] P. Neumann *et al.* Multipartite entanglement among single spins in diamond. *Science* **320**, 1326 (2008).

[11] L. Robledo *et al.* High-fidelity projective read-out of a solid-state spin quantum register. *Nature* **477**, 574 (2011).

[12] C. K. Hong, Z. Y. Ou and L. Mandel. Measurement of subpicosecond time intervals between two photons by interference. *Physical Review Letters* **59**, 2044 (1987).

[13] L. M. Duan, M. D. Lukin, J. I. Cirac and P. Zoller. Long-distance quantum communication with atomic ensembles and linear optics. *Nature* **414**, 413 (2001).

[14] C. Simon and W. Irvine. Robust Long-Distance Entanglement and a Loophole-Free Bell Test with Ions and Photons. *Physical Review Letters* **91**, 110405 (2003).

[15] S. Barrett and P. Kok. Efficient high-fidelity quantum computation using matter qubits and linear optics. *Physical Review A* **71**, 060310 (2005).

[16] D. L. Moehring *et al.* Entanglement of single-atom quantum bits at a distance. *Nature* **449**, 68 (2007).

[17] J. R. Maze *et al.* Properties of nitrogen-vacancy centers in diamond: the group theoretic approach. *New Journal of Physics* **13**, 025025 (2011).

[18] M. W. Doherty, N. B. Manson, P. Delaney and L. C. L. Hollenberg. The negatively charged nitrogen-vacancy centre in diamond: the electronic solution. *New Journal of Physics* **13**, 025019 (2011).

[19] A. Batalov *et al.* Low Temperature Studies of the Excited-State Structure of Negatively Charged Nitrogen-Vacancy Color Centers in Diamond. *Physical Review Letters* **102**, 195506 (2009).

[20] F. Kaiser *et al.* Polarization properties of single photons emitted by nitrogen-vacancy defect in diamond at low temperature. *arXiv:0906.3426* (2009).

[21] K.-M. C. Fu *et al.* Observation of the Dynamic Jahn-Teller Effect in the Excited States of Nitrogen-Vacancy Centers in Diamond. *Physical Review Letters* **103**, 256404 (2009).

[22] L. C. Bassett, F. J. Heremans, C. G. Yale, B. B. Buckley and D. D. Awschalom. Electrical Tuning of Single Nitrogen-Vacancy Center Optical Transitions Enhanced by Photoinduced Fields. *Physical Review Letters* **107**, 266403 (2011).

[23] J. P. Hadden *et al.* Strongly enhanced photon collection from diamond defect centers under microfabricated integrated solid immersion lenses. *Applied Physics Letters* **97**, 241901 (2010).

[24] P. Tamarat *et al.* Stark Shift Control of Single Optical Centers in Diamond. *Physical Review Letters* **97**, 083002 (2006).

[25] J. Isberg *et al.* High Carrier Mobility in Single-Crystal Plasma-Deposited Diamond. *Science* **297**, 1670 (2002).

[26] P. Siyushev *et al.* Monolithic diamond optics for single photon detection. *Applied Physics Letters* **97**, 241902 (2010).

[27] F. Jelezko *et al.* Single spin states in a defect center resolved by optical spectroscopy. *Applied Physics Letters* **81**, 2160 (2002).

[28] T. Legero, T. Wilk, A. Kuhn and G. Rempe. Time-resolved two-photon quantum interference. *Applied Physics B* **77**, 797 (2003).

[29] L. Robledo, H. Bernien, I. van Weperen and R. Hanson. Control and Coherence of the Optical Transition of Single Nitrogen Vacancy Centers in Diamond. *Physical Review Letters* **105**, 177403 (2010).

[30] T. Legero, T. Wilk, M. Hennrich, G. Rempe and A. Kuhn. Quantum Beat of Two Single Photons. *Physical Review Letters* **93**, 070503 (2004).

[31] R. Lettow *et al.* Quantum Interference of Tunably Indistinguishable Photons from Remote Organic Molecules. *Physical Review Letters* **104**, 123605 (2010).

[32] A. Beveratos *et al.* Room temperature stable single-photon source. *The European Physical Journal D* **18**, 191 (2002).

[33] K. Sanaka, A. Pawlis, T. Ladd, K. Lischka and Y. Yamamoto. Indistinguishable Photons from Independent Semiconductor Nanostructures. *Physical Review Letters* **103**, 053601 (2009).

[34] R. B. Patel *et al.* Two-photon interference of the emission from electrically tunable remote quantum dots. *Nature Photonics* **4**, 632 (2010).

[35] E. B. Flagg *et al.* Interference of Single Photons from Two Separate Semiconductor Quantum Dots. *Physical Review Letters* **104**, 137401 (2010).

[36] N. B. Manson, J. P. Harrison and M. Sellars. Nitrogen-vacancy center in diamond: Model of the electronic structure and associated dynamics. *Physical Review B* **74**, 104303 (2006).

[37] I. Aharonovich, A. D. Greentree and S. Prawer. Diamond photonics. *Nature Photonics* **5**, 397 (2011).

[38] A. Faraon, P. E. Barclay, C. Santori, K.-M. C. Fu and R. G. Beausoleil. Resonant enhancement of the zero-phonon emission from a colour centre in a diamond cavity. *Nature Photonics* **5**, 301 (2011).

HERALDED ENTANGLEMENT BETWEEN SOLID-STATE QUBITS SEPARATED BY THREE METRES

H. Bernien, B. Hensen, W. Pfaff, G. Koolstra, M.S. Blok, L. Robledo, T.H. Taminiau,
M. Markham, D.J. Twitchen, L. Childress, and R. Hanson

Quantum entanglement between spatially separated objects is one of the most intriguing phenomena in physics. The outcomes of independent measurements on entangled objects show correlations that cannot be explained by classical physics. Besides being of fundamental interest, entanglement is a unique resource for quantum information processing and communication. Entangled qubits can be used to establish private information or implement quantum logical gates [1,2]. Such capabilities are particularly useful when the entangled qubits are spatially separated [3-5], opening the opportunity to create highly connected quantum networks [6] or extend quantum cryptography to long distances [7,8]. Here we present a key experiment towards the realisation of long-distance quantum networks with solid-state quantum registers. We have entangled two electron spin qubits in diamond that are separated by a three-metre distance. We establish this entanglement using a robust protocol based on local creation of spin-photon entanglement and a subsequent joint measurement of the photons. Detection of the photons heralds the projection of the spin qubits onto an entangled state. We verify the resulting non-local quantum correlations by performing single-shot readout [9] on the qubits in different bases. The long-distance entanglement reported here can be combined with recently achieved initialisation, readout and entanglement operations [9-13] on local long-lived nuclear spin registers, enabling deterministic long-distance teleportation, quantum repeaters and extended quantum networks.

8.1 Introduction

A quantum network can be constructed by using entanglement to connect local processing nodes, each containing a register of well-controlled and long-lived qubits[6]. Solids are an attractive platform for such registers, as the use of nano-fabrication and material design may enable well-controlled and scalable qubit systems[14]. The potential impact of quantum networks on science and technology has recently spurred research efforts towards generating entangled states of distant solid-state qubits[15–21].

A prime candidate for a solid-state quantum register is the nitrogen-vacancy (NV) defect centre in diamond. The NV centre combines a long-lived electronic spin (S=1) with a robust optical interface, enabling measurement and high-fidelity control of the spin qubit[15,22–24]. Furthermore, the NV electron spin can be used to access and manipulate nearby nuclear spins[9–13], thereby forming a multi-qubit register. To use such registers in a quantum network requires a mechanism to coherently connect remote NV centres.

Here we demonstrate the generation of entanglement between NV centre spin qubits in distant setups. We achieve this by combining recently established spin initialisation and single-shot readout techniques[9] with efficient resonant optical detection and feedback-based control over the optical transitions, all in a single experiment and executed with high fidelity. These results put solid-state qubits on par with trapped atomic qubits[3–5] as highly promising candidates for implementing quantum networks.

Our experiment makes use of two NV spin qubits located in independent low-temperature setups separated by 3 metres (Fig. 8.1a). We encode the qubit basis states $|\uparrow\rangle$ and $|\downarrow\rangle$ in the NV spin sub-levels $m_s = 0$ and $m_s = -1$, respectively. Each qubit can be independently read out by detecting spin-dependent fluorescence in the NV phonon side band (non-resonant detection)[9]. The qubits are individually controlled with microwave pulses applied to on-chip strip-lines[23]. Quantum states encoded in the qubits are extremely long-lived: using dynamical decoupling techniques[23] we obtain a coherence time exceeding 10 ms (Fig. 8.6), the longest coherence time measured to date for a single electron spin in a solid.

8.2 Protocol

We generate and herald entanglement between these distant qubits by detecting the resonance fluorescence of the NV centres. The specific entanglement protocol we employ is based on the proposal of S. Barrett and P. Kok[25], and is schematically drawn in figure 8.2b. Both centres NV A and NV B are initially prepared in a superposition $1/\sqrt{2}(|\uparrow\rangle + |\downarrow\rangle)$. Next, each NV centre is excited by a short laser pulse that is resonant with the $|\uparrow\rangle$ to $|e\rangle$ transition, where $|e\rangle$ is an optically excited state with the same spin projection as $|\uparrow\rangle$. Spontaneous emission locally entangles the qubit and photon number, leaving each setup in the state $1/\sqrt{2}(|\uparrow 1\rangle + |\downarrow 0\rangle)$, where 1 (0) denotes the presence (absence) of an emitted photon; the joint qubit-photon state of both setups is then described by $1/2(|\uparrow_A\uparrow_B\rangle |1_A1_B\rangle + |\downarrow_A\downarrow_B\rangle |0_A0_B\rangle + |\uparrow_A\downarrow_B\rangle |1_A0_B\rangle + |\downarrow_A\uparrow_B\rangle |0_A1_B\rangle)$. The two photon modes, A and B, are directed to the input
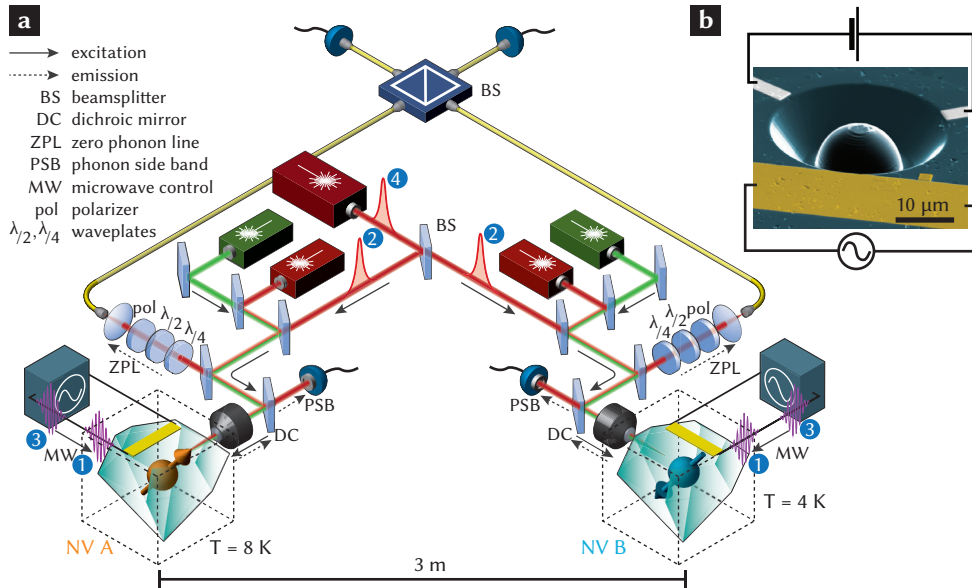
Figure 8.1 | Experimental setup. a, Each nitrogen vacancy (NV) centre resides in a synthetic ultra-pure diamond oriented in the ⟨111⟩ direction. The two diamonds are located in two independent low-temperature confocal microscope setups separated by 3 metres. The NV centres can be individually excited resonantly by a red laser and off-resonantly by a green laser. The emission (dashed arrows) is spectrally separated into an off-resonant part (phonon side band, PSB) and a resonant part (zero-phonon line, ZPL). The PSB emission is used for independent single-shot readout of the spin qubits[9]. The ZPL photons from the two NV centres are overlapped on a fiber-coupled beamsplitter. Microwave pulses for spin control are applied via on-chip microwave strip-lines. An applied magnetic field of 17.5 G splits the $m_s = \pm 1$ levels in energy. The optical frequencies of NV B are tuned by a d.c. electric field applied to the gate electrodes (**b,** scanning electron microscope image of a similar device). To enhance the collection efficiency, solid immersion lenses have been milled around the two NV centres[9].
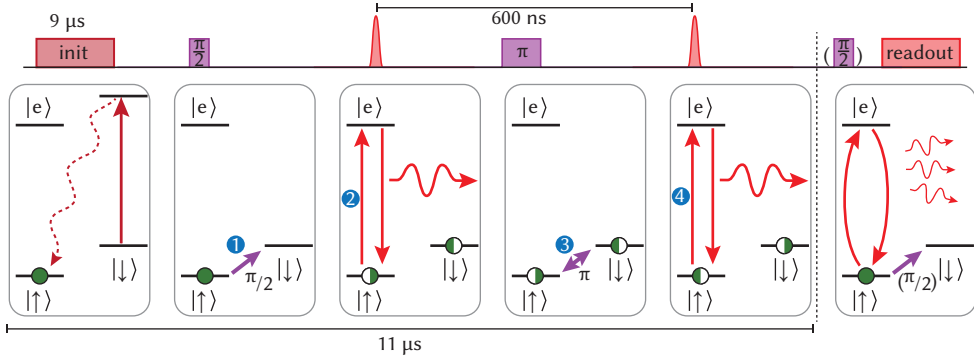
Figure 8.2 | Entanglement protocol. Both NV centres are initially prepared in a super-position $1/\sqrt{2}(|{\uparrow}\rangle + |{\downarrow}\rangle)$. A short 2 ns spin-selective resonant laser pulse creates spin-photon entanglement $1/\sqrt{2}(|{\uparrow}\,1\rangle + |{\downarrow}\,0\rangle)$. The photons are overlapped on the beamsplitter and detected in the two output ports. Both spins are then flipped, and the NV centres are excited a second time. The detection of one photon in each excitation round heralds the entanglement and triggers individual spin readout.

ports of a beamsplitter (see Fig. 8.1a), so that fluorescence observed in an output port could have originated from either NV centre. If the photons emitted by the two NV centres are indistinguishable, detection of precisely one photon on an output port would correspond to measuring the photon state $|1_A 0_B\rangle \pm e^{-i\varphi} |0_A 1_B\rangle$ (where φ is a phase that depends on the optical path length). Such a detection event would thereby project the qubits onto the maximally entangled state $|\psi\rangle = 1/\sqrt{2}(|{\uparrow}_A{\downarrow}_B\rangle \pm e^{-i\varphi} |{\downarrow}_A{\uparrow}_B\rangle)$.

Any realistic experiment, however, suffers from photon loss and imperfect detector efficiency; detection of a single photon is thus also consistent with creation of the state $|{\uparrow}{\uparrow}\rangle$. To eliminate this possibility, both qubits are flipped and optically excited for a second time. Since $|{\uparrow}{\uparrow}\rangle$ is flipped to $|{\downarrow}{\downarrow}\rangle$, no photons are emitted in the second round for this state. In contrast, the states $|\psi\rangle$ will again yield a single photon. Detection of a photon in both rounds thus heralds the generation of an entangled state. The second round not only renders the protocol robust against photon loss, but it also changes φ into a global phase, making the protocol insensitive to the optical path length difference[25] (see Supporting Material). Furthermore, flipping the qubits provides a refocusing mechanism that counteracts spin dephasing during entanglement generation. The final state is one of two Bell states $|\psi^\pm\rangle = 1/\sqrt{2}(|{\uparrow}_A{\downarrow}_B\rangle \pm |{\downarrow}_A{\uparrow}_B\rangle)$, with the sign depending on whether the same detector (+), or different detectors (−) clicked in the two rounds.

8.3 Implementation

A key challenge for generating remote entanglement with solid-state qubits is obtaining a large flux of indistinguishable photons, in part because local strain in the host lattice can induce large variations in photon frequency. The optical excitation spectra of the NV centres (Fig. 8.3a) display sharp spin-selective transitions. Here we use the E_y transition (spin projection $m_s = 0$) in the entangling protocol and for qubit readout; we use the A_1 transition for fast optical pumping into $|{\uparrow}\rangle$[9]. Due to different strain in the two diamonds, the frequencies of the E_y transitions differ by 3.5 GHz, more than 100 line-widths. By applying a voltage to an on-chip electrode (Fig. 8.1b) we tune the optical transition frequencies of one centre (NV B) through the d.c. Stark effect[18,26] and bring the E_y transitions of the two NV centres into resonance (Fig. 8.3a bottom).

Charge fluctuations near the NV centre also affect the optical frequencies. To counteract photo-ionisation we need to regularly apply a green laser pulse to re-pump the NV centre into the desired charge state. This re-pump pulse changes the local electrostatic environment, leading to jumps of several line-widths in the optical transition frequencies[27]. To overcome these effects, we only initiate an experiment if the number of photons collected during a two-laser probe stage (Fig. 8.3b) exceeds a threshold, thereby ensuring that the NV centre optical transitions are on resonance with the lasers (see chapter 3.3). The preparation procedure markedly improves the observed optical coherence: as the probe threshold is increased, optical Rabi oscillations persist for longer times (see Fig. 8.3b). For high thresholds, the optical damping time saturates around the value expected for a lifetime-limited line-width[27], indicating that the effect of spectral jumps induced by the re-pump laser is strongly mitigated.

Besides photon indistinguishability, successful execution of the protocol also requires that the detection probability of resonantly emitted photons exceeds that of scattered laser photons and of detector dark counts. This is particularly demanding for NV centres since only about 3% of their emission is in the zero-phonon line and useful for the protocol. To minimise detection of laser photons, we use both a cross-polarised excitation-detection scheme (Fig. 8.3c inset) and a detection time filter that exploits the difference between the length of the laser pulse (2 ns) and the NV centre's excited state lifetime (12 ns) (Fig. 8.3c). For a typical detection window used, this reduces the contribution of scattered laser photons to about 1%. Combined with micro-fabricated solid-immersion lenses for enhanced collection efficiency (Fig. 8.1b) and spectral filtering for suppressing non-resonant NV emission, we obtain a detection probability of a resonant NV photon of about 4×10^{-4} per pulse — about 70 times higher than the sum of background contributions.

The degree of photon indistinguishability and background suppression can be obtained directly from the second-order autocorrelation function $g^{(2)}$, which we extract from our entanglement experiment (see Supporting Material). For fully distinguishable photons, the value of $g^{(2)}$ would reach 0.5 at zero arrival time difference. A strong deviation from this behaviour is observed (Fig. 8.3d) due to two-photon quantum interference[28] that, for perfectly indistinguishable photons, would make the central peak fully vanish. The remaining
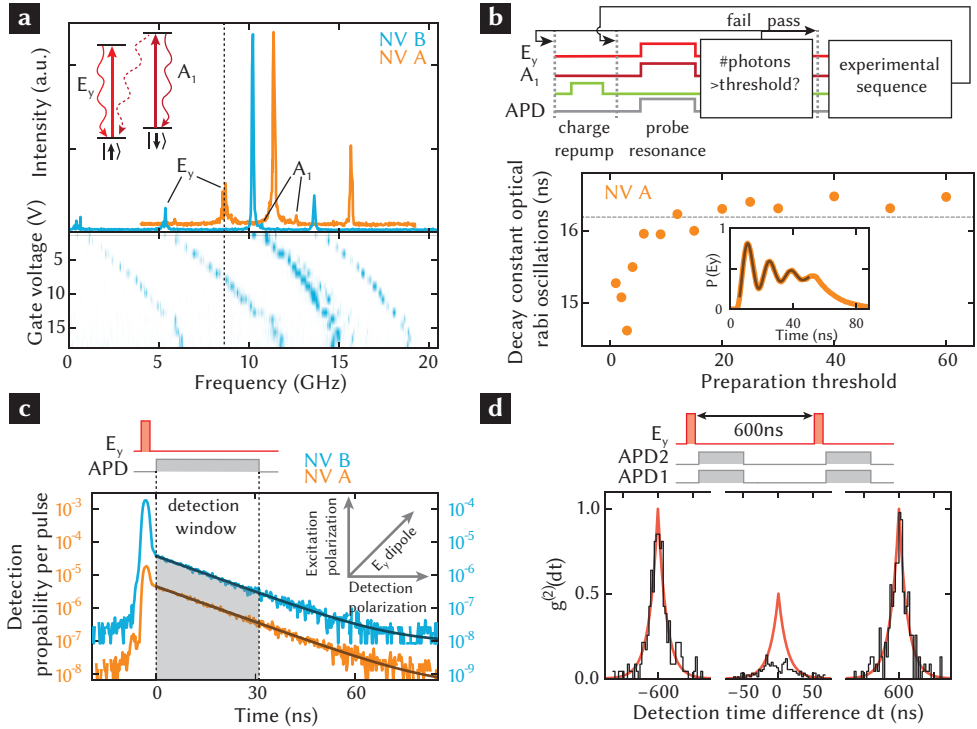
Figure 8.3 | Generating and detecting indistinguishable photons. a, Excitation spectra; frequency relative to 470.4515 THz. By applying a voltage to the gates of NV B the E_y transitions are tuned into resonance. **b,** Dynamical preparation of charge and optical resonance. Top: Preparation protocol. A 10 μs green laser pulse pumps the NV into its negative charge state [9]. The transition frequencies are probed by exciting the E_y and A_1 transitions for 60 μs. Conditional on surpassing a certain number of photons detected the experiment is started (pass) or preparation is repeated (fail). APD, avalanche photodiode. Bottom: Line-narrowing effect of the preparation shown by the dependence of the decay time of optical Rabi oscillations on preparation threshold. Dashed line indicates lifetime-limited damping [27]. **c,** Resonant optical excitation and detection. The polarisation axis of the detection path is aligned perpendicular to the excitation axis. The dipole axis of the E_y transition is oriented in between these two axes (inset). Remaining laser light reflection is time-filtered by defining a photon detection window that starts after the laser pulse. **d,** Two-photon quantum interference using resonant excitation and detection. The $g^{(2)}$ correlation function is obtained from all coincidence detection events of APD 1 and APD 2 during the entanglement experiment (see Supporting Material). The side-peaks are fit to an exponential decay; from the fit values, we obtain the expected central peak shape $g_\perp^{(2)}$ (red line) for non-interfering photons. The visibility of the interference is given by $(g_\perp^{(2)} - g^{(2)})/g_\perp^{(2)}$.

coincidences are likely caused by (temperature-dependent) phonon-induced transitions between optically excited states[29] in NV A. The visibility of the two-photon interference observed here — $(80 \pm 5)\%$ for $|dt| < 2.56$ ns — is a significant improvement over previously measured values[18,19] and key to the success of the entangling scheme.

To experimentally generate and detect remote entanglement, we run the following sequence: First, both NV centres are independently prepared into the correct charge state and brought into optical resonance according to the scheme in figure 8.3b. Then we apply the entangling protocol shown in figure 8.2 using a 600 ns delay between the two optical excitation rounds. We repeat the protocol 300 times before we return to the resonance preparation step; this number is a compromise between maximising the attempt rate and minimising the probability of NV centre ionisation. A fast logic circuit monitors the photon counts in real time and triggers single-shot qubit readout on each setup whenever entanglement is heralded, i.e. whenever a single photon is detected in each round of the protocol. The readout projects each qubit onto the $\{|{\uparrow}\rangle, |{\downarrow}\rangle\}$ states (Z-basis), or on the $\{|{\uparrow}\rangle \pm |{\downarrow}\rangle, |{\uparrow}\rangle \mp |{\downarrow}\rangle\}$ states (X or −X basis). The latter two are achieved by first rotating the qubit by $\pi/2$ using a microwave pulse before readout. By correlating the resulting single-qubit readout outcomes we can verify the generation of the desired entangled states. To obtain reliable estimates of the two-qubit state probabilities, we correct the raw data with a maximum-likelihood method for local readout infidelities. These readout errors are known accurately from regular calibrations performed during the experiment (see Supporting Material).

8.4   Results

Figure 8.4 shows the obtained correlations. When both qubits are measured along Z (readout basis {Z,Z}), the states ψ^+ and ψ^- (as identified by their different photon signatures) display strongly anti-correlated readout results (odd parity). The coherence of the joint qubit state is revealed by measurements performed in rotated bases ({X,X}, {−X,X}), which also exhibit significant correlations. Furthermore, these measurements allow us to distinguish between states ψ^+ and ψ^-. For ψ^+ the {X,X} ({−X,X}), outcomes exhibit even (odd) parity, whereas the ψ^- state displays the opposite behaviour, as expected. The observed parities demonstrate that the experiment yields the two desired entangled states.

We calculate a strict lower bound on the state fidelity by combining the measurement results from different bases (see Supporting Material):

$$F = \langle \psi^{\pm} | \rho | \psi^{\pm} \rangle \geq 1/2(P_{\uparrow\downarrow} + P_{\downarrow\uparrow} + C) - \sqrt{P_{\uparrow\uparrow}P_{\downarrow\downarrow}}, \tag{8.1}$$

where P_{ij} is the probability for the measurement outcome ij in the {Z,Z} basis (i.e. the diagonal elements of the density matrix ρ) and C is the contrast between odd and even outcomes in the rotated bases. We find a lower bound of $(69 \pm 5)\%$ for ψ^- and $(58 \pm 6)\%$ for ψ^+, and probabilities of 99.98% and 91.8%, respectively, that the state fidelity is above the classical limit of 0.5. These values firmly establish that we have created remote entanglement, and are the main result of this paper.
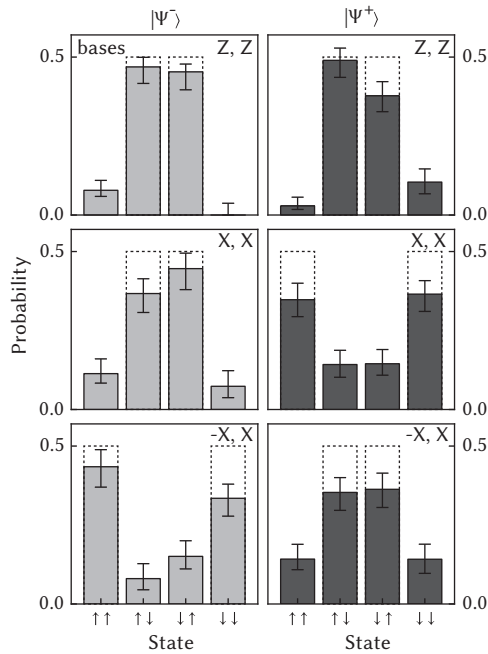
Figure 8.4 | Verification of entanglement by spin-spin correlations. Each time that entanglement is heralded the spin qubits are individually read out and their results correlated. The readout bases for NV A and NV B can be rotated by individual microwave control (see text). The state probabilities are obtained by a maximum-likelihood estimation on the raw readout results (see Supporting Material). Error bars depict 68% confidence intervals; dashed lines indicate expected results for perfect state fidelity. Data is obtained from 739 heralding events. For ψ^-, the detection window in each round is set to 38.4 ns, and the maximum absolute detection time difference $|\delta\tau|$ between the two photons relative to their laser pulses is restricted to 25.6 ns. $\delta\tau = \tau_2 - \tau_1$, where τ_1 is the arrival time of the first photon relative to the first laser pulse and τ_2 the arrival time of the second photon relative to the second laser pulse. For ψ^+ the second detection window is set to 19.2 ns with $|\delta\tau| < 12.8$ ns, in order to reduce the effect of photo-detector after-pulsing.
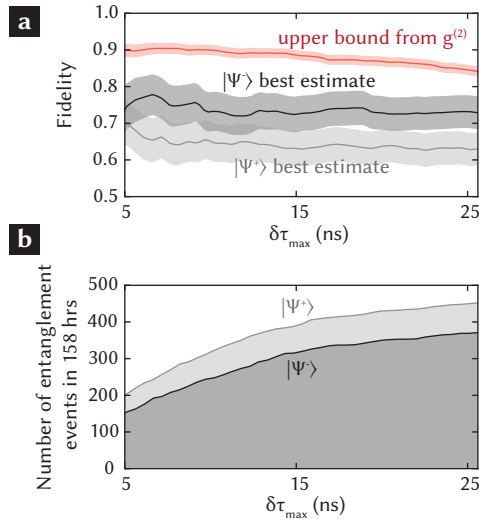
Figure 8.5 | Dependence of the fidelity and number of entanglement events on the detection time difference of the photons. a, Upper bound on the state fidelity from photon interference data (see Supporting Material) and best estimate of the state fidelity from the correlation data as a function of the maximum allowed photon detection time difference ($|\delta\tau| < \delta\tau_{max}$). Detection time windows are chosen as in figure 8.4. Shaded regions indicate 68% confidence intervals. **b,** Number of entanglement events obtained during 158 hours as a function of the maximum allowed photon detection time difference $\delta\tau_{max}$.

The lower bound on the state fidelity given above takes into account the possible presence of coherence within the even-parity subspace $\{|\uparrow\uparrow\rangle, |\downarrow\downarrow\rangle\}$. However, the protocol selects out states with odd parity and therefore this coherence is expected to be absent. To compare the results to the expected value and to account for sources of error, we set the related (square-root) term in Eq. 1 to zero and obtain for the data in figure 8.4 as best estimate $F = (73 \pm 4)\%$ for ψ^- and $F = (64 \pm 5)\%$ for ψ^+.

Several known error sources contribute to the observed fidelity. Most importantly, imperfect photon indistinguishability reduces the coherence of the state. In figure 8.5a we plot the maximum state fidelity expected from photon interference data (Fig. 8.3d) together with the measured state fidelities, as a function of the maximum allowed difference in detection time of the two photons relative to their respective laser pulses. We find that the fidelity can be slightly increased by restricting the data to smaller time differences, albeit at the cost of a lower success rate (Fig. 8.5b).

The fidelity is further decreased by errors in the microwave pulses (estimated at 3.5%), spin

initialisation (2%), spin decoherence (< 1%) and spin flips during the optical excitation (1%) (see Supporting Material). Moreover, ψ^+ is affected by after-pulsing, whereby detection of a photon in the first round triggers a fake detector click in the second round. Such after-pulsing leads to a distortion of the correlations (see for example the increased probability for $|\downarrow\downarrow\rangle$ in figure 8.4) and thereby a reduction in fidelity for ψ^+ (see Supporting Material). Besides these errors that reduce the actual state fidelity, the measured value is also slightly lowered by a conservative estimation for readout infidelities and by errors in the final microwave $\pi/2$ pulse used for reading out in a rotated basis.

The fidelity of the remote entanglement can be significantly increased in future experiments by further improving photon indistinguishability. This may be achieved by more stringent frequency selection in the resonance initialisation step and by working at lower temperatures, which will reduce phonon-mediated excited-state mixing[29]. Also, the microwave errors can be much reduced; for instance by using isotopically purified diamonds[12] and polarising the host nitrogen nuclear spin[9].

The success probability of the protocol is given by $P_\psi = 1/2\eta_A\eta_B$. η_i is the overall detection efficiency of resonant photons from NV i and the factor $1/2$ takes into account cases where the two spins are projected into $|\downarrow\downarrow\rangle$ or $|\uparrow\uparrow\rangle$, which are filtered out by their different photon signature. In the current experiment we estimate $P_\psi \approx 10^{-7}$ from the data in figure 8.5c. The entanglement attempt rate is about 20 kHz, yielding one entanglement event per 10 minutes. This is in good agreement with the 739 entanglement events obtained over a time of 158 hours. The use of optical cavities will greatly enhance both the collection efficiency and emission in the zero-phonon line[30] and increase the success rate by several orders of magnitude.

8.5 Conclusion

Creation of entanglement between distant spin qubits in diamond, as reported here, opens the door to extending the remarkable properties of NV-based quantum registers towards applications in quantum information science. By transferring entanglement to nuclear spins near each NV centre, a nonlocal state might be preserved for seconds or longer[12], facilitating the construction of cluster states[2] or quantum repeaters[8]. At the same time, the auxiliary nuclear spin qubits also provide an excellent resource for processing and error correction. When combined with future advances in nanofabricated integrated optics and electronics, the use of electrons and photons as quantum links and nuclear spins for quantum processing and memory offers a compelling route towards realization of solid-state quantum networks.

8.6 Supporting Material

8.6.1 Setup and sample

Spin coherence

To demonstrate the potential for storing quantum states in the NV electronic spin at low temperatures we perform dynamical decoupling[23]. We find a coherence time that exceeds 10 ms (Fig. 8.6).
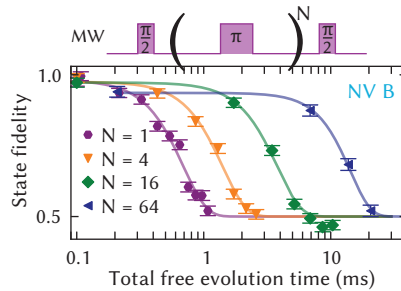
Figure 8.6 | Electron spin coherence at low temperatures. The coherence of the NV B spin qubit as a function of total free evolution time t_{FE} during an N-pulse dynamical decoupling sequence[23]. Curves are fit to $A \exp[-(t/T_{coh})^3] + 0.5$. For N = 64 we find $T_{coh} = 14.3 \pm 0.4$ ms.

Experiment Control

For the experiment to be feasible, a high repetition rate of the entanglement generation sequence is crucial, because the success probability per shot is small, $P_s = 1/2 \times \eta_A \eta_B \approx 10^{-7}$. We achieve a reasonable repetition rate by employing a conditional protocol as follows (Fig. 8.7): We first ensure that both NV centres are in the negative charge state and on resonance. To this end we independently re-set the charge and resonance state of the two NVs with green laser pulses until the resonant excitation lasers are on resonance[9,13]. After this preparation we run the spin-preparation and entanglement generation sequence. In case of successful generation of entanglement we read out both spins in a single shot and return to the charge and resonance (CR) check. Otherwise, we repeat spin-preparation and entanglement generation. After 300 unsuccessful entanglement attempts we start over with the CR check. The success probabilities for passing the CR check, $P_{CR} \approx 2\%$, and for successfully generating entanglement let us predict an entanglement generation rate of $\sim 1/10$ minutes. For comparison, an unconditional protocol in which charge/resonance and entanglement generation are only verified in post-processing would yield an entanglement rate of only $\sim 1/50$ hours.

For sufficiently fast decisions we employ a programmable logic device (CPLD; Altera Max V development kit) that time-filters the signal and recognises a successful entanglement event. If a success occurs, a stop trigger is sent to the AWG within 50 ns to prevent it from running the next entanglement cycle. Furthermore, the logic device triggers both ADwin controllers to start their readout sequence. Further (more selective) time filtering is done in post-processing for the successful events, by combining the time-tagged data and spin readout data.
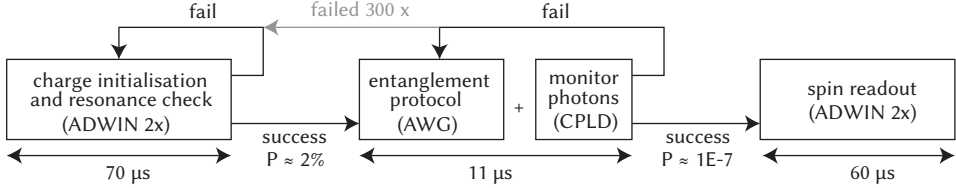
Figure 8.7 | Conditional sequence for implementation of the entanglement protocol. Two ADwins independently initialise each NV centre and perform the charge-resonance check verification. If both checks pass, a trigger is sent to the AWG that executes the entanglement protocol. The protocol is run up to 300 times until it is successful. A successful attempt is recognised by a logic device (CPLD) that looks for a success-signature in the stream of photon clicks produced, and sends a halt trigger to the AWG when it does. The readout is then performed by the ADwins, after which the sequence starts over.

8.6.2 Methods

Spin readout

We perform single-shot readout (SSRO) of the NV spin states by spin-resolved optical excitation as described in chapter 6[9]. The fidelity for reading out $|\uparrow\rangle$ correctly is given by the probability with which at least one photon is detected when $|\uparrow\rangle$ is prepared:

$$\mathcal{F}_\uparrow = 1 - P(0|\uparrow). \tag{8.2}$$

Conversely,

$$\mathcal{F}_\downarrow = P(0|\downarrow), \tag{8.3}$$

after preparation of $|\downarrow\rangle$. The mean fidelity for readout of an unknown spin-state is therefore $\mathcal{F}_{\text{SSRO}} = (\mathcal{F}_\uparrow + \mathcal{F}_\downarrow)/2$. Infidelities are due to photon losses and 'incorrectly' obtained photons (e.g., due to off-resonant excitation or detector dark counts), leading to wrong assignment of the spin-state. The readout result of the two-spin-state

$$|\psi\rangle = c_{\uparrow\uparrow}|\uparrow\uparrow\rangle + c_{\uparrow\downarrow}|\uparrow\downarrow\rangle + c_{\downarrow\uparrow}|\downarrow\uparrow\rangle + c_{\downarrow\downarrow}|\downarrow\downarrow\rangle \tag{8.4}$$

is therefore

$$\mathcal{R} = \begin{pmatrix} p_{\uparrow\uparrow} \\ p_{\uparrow\downarrow} \\ p_{\downarrow\uparrow} \\ p_{\downarrow\downarrow} \end{pmatrix} = E \begin{pmatrix} |c_{\uparrow\uparrow}|^2 \\ |c_{\uparrow\downarrow}|^2 \\ |c_{\downarrow\uparrow}|^2 \\ |c_{\downarrow\downarrow}|^2 \end{pmatrix}, \tag{8.5}$$

where p_{ij} is the probability for measurement outcome $i, j \in \{\uparrow, \downarrow\}$, and the induced error is described by the matrix $E = E^A \otimes E^B$, where $E^{A,B}$ describe the independent readout errors on both NVs.

Single-shot readout calibration

To obtain a characterisation of the electron SSRO we perform a calibration [9] every three hours during the entanglement measurements (Fig. 8.8). We use the statistical mean and standard deviation of the fidelities from all calibration measurements as values and uncertainties for $\mathcal{F}_\uparrow^A$, $\mathcal{F}_\downarrow^A$, $\mathcal{F}_\downarrow^B$ and $\mathcal{F}_\uparrow^B$ as required for state estimation.

For the calibration measurements we take into account imperfect spin-initialisation due to incomplete optical spin pumping [9]. Measuring the probability $p_\uparrow^{\text{init}}$ ($p_\downarrow^{\text{init}}$) that the initialisation into $|\uparrow\rangle$ ($|\downarrow\rangle$) is successful, the readout fidelities then become

$$\mathcal{F}_\uparrow = \frac{1 - p_\uparrow^{\text{init}} - p(0|\uparrow_{\text{init}}) + p_\uparrow^{\text{init}} p(0|\uparrow_{\text{init}}) - p_\downarrow^{\text{init}} p(\geq 1|\downarrow_{\text{init}})}{p(0|\uparrow_{\text{init}}) + p(\geq 1|\downarrow_{\text{init}}) - 1}, \tag{8.6}$$

$$\mathcal{F}_\downarrow = \frac{1 - p_\downarrow^{\text{init}} - p(\geq 1|\downarrow_{\text{init}}) - p_\uparrow^{\text{init}} p(0|\uparrow_{\text{init}}) + p_\downarrow^{\text{init}} p(\geq 1|\downarrow_{\text{init}})}{p(0|\uparrow_{\text{init}}) + p(\geq 1|\downarrow_{\text{init}}) - 1}. \tag{8.7}$$

$p(0|\uparrow_{\text{init}})$ ($p(\geq 1|\downarrow_{\text{init}})$) are the probabilities to measure 0 (≥ 1) photons during the calibration after imperfect initialisation into $|\uparrow\rangle$ ($|\downarrow\rangle$). From independent initialisation measurements we estimate $p_\uparrow^{\text{init,A}} = (99.5 \pm 0.1)\%$, $p_\uparrow^{\text{init,B}} = (98.3 \pm 0.6)\%$, $p_\downarrow^{\text{init,A}} = (99.7 \pm 0.2)\%$, and $p_\downarrow^{\text{init,B}} = (99.6 \pm 0.3)\%$. The results of the calibration measurements shown in Fig. 8.8 include this analysis.

Analysis of the TPQI signature

As a measure of the indistinguishability of the photons from NV A and B we evaluate the difference between the measured $g^{(2)}(dt)$ function and the expected function $g_\perp^{(2)}(dt)$ that would be obtained in the case of perfectly distinguishable photons. We define the visibility as

$$V(dt) = \frac{g_\perp^{(2)}(dt) - g^{(2)}(dt)}{g_\perp^{(2)}(dt)}. \tag{8.8}$$

$g^{(2)}(dt)$ is proportional to the histogram of all coincidences obtained between photons detected on the two APDs after the beam splitter, where $dt = t_1 - t_2$, and t_1 (t_2) is the arrival
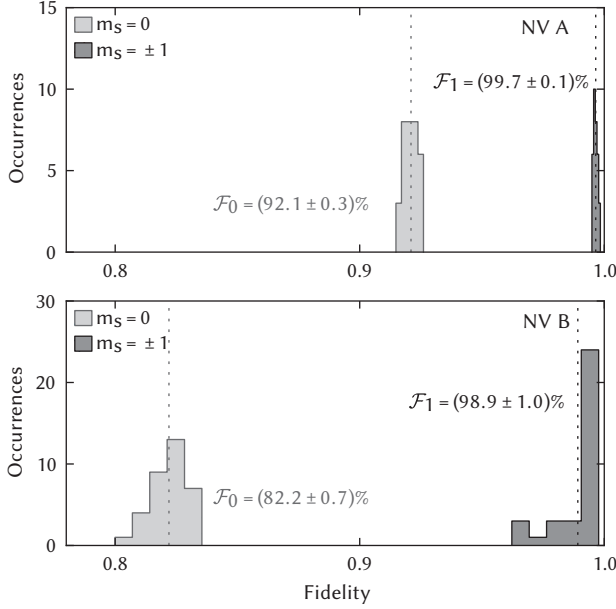
Figure 8.8 | Readout characterisation for both NVs. Histograms and means (red) of the SSRO fidelities, for both NVs, A and B, and both spin states, $m_\mathrm{s} = 0$ and $m_\mathrm{s} = \pm 1$, measured during all entanglement measurements. Imperfect spin-preparation before calibration measurements are taken into account.

time of the photon detected by APD 1 (2). We only take into account photons obtained during the same entanglement attempt. Because our pulse scheme consists of two optical π pulses, coincidence peaks only occur around $dt = 0$ ns (two photons detected after the same excitation pulse) and $dt = \pm 600$ ns (one photon detected after each excitation pulse).

To determine $g_\perp^{(2)}(dt)$ from our measurement we can use the coincidence count-rates of the side peaks around $dt = \pm 600$ ns. The shape of $g_\perp^{(2)}(dt)$ for two single emitters in our pulse scheme is given by

$$g_\perp^{(2)}(dt) = \sum_{i=-1,0,1} A_i \exp(-\Gamma|dt - i \times 600\,\mathrm{ns}|), \qquad (8.9)$$

where the relative amplitudes A_i are determined by the spin-dependent excitation probabilities: The full state of the system after the first excitation round has the form (see main text)

$$|\psi\rangle = \frac{1}{2} \left(|\uparrow\uparrow\rangle \, |11\rangle + |\downarrow\downarrow\rangle \, |00\rangle + |\uparrow\downarrow\rangle \, |10\rangle + |\downarrow\uparrow\rangle \, |01\rangle \right). \qquad (8.10)$$

Neglecting initialisation and microwave errors, the $|00\rangle$, $|11\rangle$ states both contribute to the A_0 peak only, and the $|01\rangle$, $|10\rangle$ states contribute to the $A_{\pm 1}$ peaks only. Because all states occur with equal probability (1/4) and collection efficiency factor ($\eta_A \eta_B$), we have

$$A_0 = A_{-1} + A_{+1}, \text{ and } A_{-1} = A_{+1}. \tag{8.11}$$

The amplitudes $A_{\pm 1}$ can be extracted from the measurement of $g^{(2)}(dt)$, because for the side peaks, $g^{(2)}(dt) = g_\perp^{(2)}(dt)$.

We note that in Fig. 3 of the main text we have renormalised the central peak such that $g_\perp^{(2)}(0\,\text{ns}) = 1/2$, the expected result for a conventional pulsed TPQI experiment, with an infinite pulse sequence and two single emitters, for clarity. As the same normalisation factor is applied to the measured central peak of $g^{(2)}(dt)$, this does not change the visibility.

Maximum likelihood estimation of the spin-spin correlations

To estimate the eigenstate measurement populations $|c_{ij}|^2$ from a number of raw events n_{ij} in which outcome i has been obtained for NV A and outcome j for NV B, we perform a maximum likelihood estimation.

The raw events are distributed according to a multinomial distribution $f(n_{ij})$ with parameters $p_{\uparrow\uparrow}, p_{\uparrow\downarrow}, p_{\downarrow\uparrow}$, and $p_{\downarrow\downarrow} = 1 - p_{\uparrow\uparrow} - p_{\uparrow\downarrow} - p_{\downarrow\uparrow}$, the probabilities for each possible outcome, that are in turn a function of the state probabilities $|c_{ij}|^2$, as defined from Eq. (8.5) above.

The Likelihood function for the probabilities, parametrized by the measurement outcomes $n_{\uparrow\uparrow}, n_{\uparrow\downarrow}, n_{\downarrow\uparrow}, n_{\downarrow\downarrow}$, and $n = n_{\uparrow\uparrow} + n_{\uparrow\downarrow} + n_{\downarrow\uparrow} + n_{\downarrow\downarrow}$, is therefore

$$\mathcal{L}\left[p_{ij}(E, |c_{ij}|^2) \right] = \frac{n!}{n_{\uparrow\uparrow}! n_{\uparrow\downarrow}! n_{\downarrow\uparrow}! n_{\downarrow\downarrow}!} p_{\uparrow\uparrow}^{n_{\uparrow\uparrow}} p_{\uparrow\downarrow}^{n_{\uparrow\downarrow}} p_{\downarrow\uparrow}^{n_{\downarrow\uparrow}} p_{\downarrow\downarrow}^{n_{\downarrow\downarrow}}. \tag{8.12}$$

The values $|c_{ij}|^2$ that maximise the likelihood are the desired populations. We find the global maxima by sampling through the parameter space numerically.

From the Likelihood function we also obtain Bayesian confidence intervals [31] (or credible intervals) by integration. We assume a uniform prior on the intervals $p_{ij} \in (0, 1)$. The error bars in Fig. 8.9 and Fig. 8.4 in the main text correspond to 68% confidence intervals of the marginal probability distributions obtained from integrating over the two other probabilities. We note that the uncertainty originating form the uncertainty in the SSRO fidelities $\mathcal{F}_{\uparrow,\downarrow}^{A,B}$ is negligible compared to the statistical uncertainty.

Maximum likelihood estimation of the Bell state fidelity

From the likelihood for a set of probabilities $p_{ij}^{Z,Z}$ (for both spins measured in the Z-basis), $p_{ij}^{X,X}$ (both spins measured in the X-basis) and $p_{ij}^{-X,X}$ (spins measured in the X and $-$X-basis,
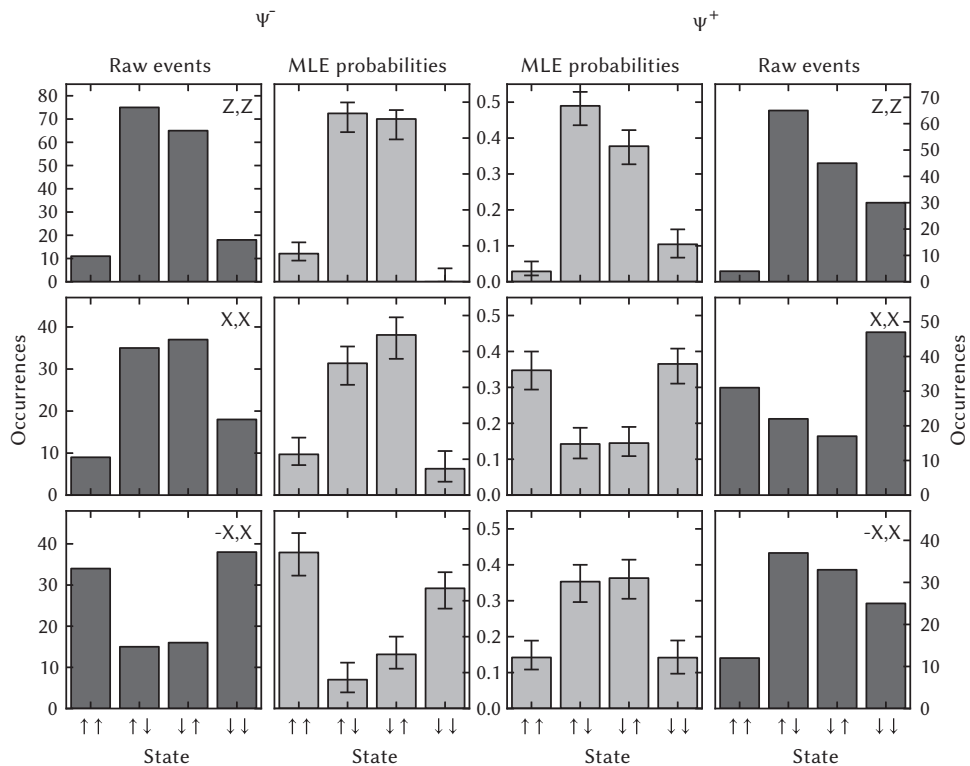
Figure 8.9 | State estimation. Raw events and maximum-likelihood estimation of the state populations $|c_{ij}|^2$, for both prepared states Ψ^-, Ψ^+, and all three measurement bases Z,Z; X,X; and -X,X as described above. Each of the six subplots represents an independent MLE. We note that the MLE for the ZZ-basis measurement of Ψ^- lies on the boundary of the physical space.

respectively), the likelihood for any value of $\mathcal{F}$ can be obtained,

$$\mathcal{L}(\mathcal{F}) = \int_{\mathcal{F}} \left(\prod_{i,j} \mathrm{d}p_{ij}^{Z,Z} \mathrm{d}p_{ij}^{X,X} \mathrm{d}p_{ij}^{-X,X} \right) \mathcal{L}(p_{ij}^{Z,Z}) \mathcal{L}(p_{ij}^{X,X}) \mathcal{L}(p_{ij}^{-X,X}), \qquad (8.13)$$

where the integration is taken over a constant value of $\mathcal{F}_{\mathrm{LB}}$ or $\mathcal{F}$. The expression for $\mathcal{F}_{\mathrm{LB}}$ is given in Eq. (8.1); for our best estimate for the fidelity, $\mathcal{F}$, we set the square-root term in this expression to zero.

We perform this integration numerically (Fig. 8.10) for a set of values for $\mathcal{F}_{\mathrm{LB}}$ and $\mathcal{F}$. Because of the finite resolution of the numerical calculations, we fit the resulting distribution with a normalised Gaussian (free parameters are only the mean and the standard deviation) to obtain the best value and the 68% confidence interval, from the standard deviation of the Gaussian fit. Fig. 8.10 shows that this procedure is justified for our results.
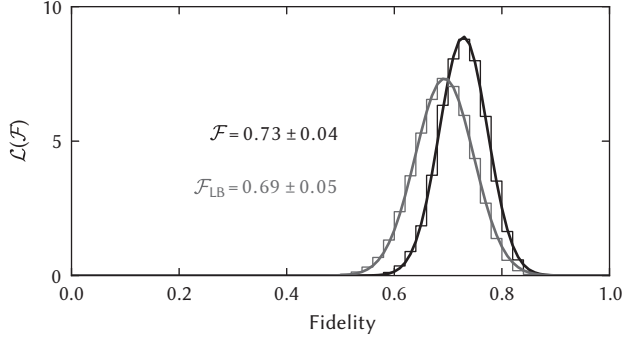
Figure 8.10 | Maximum likelihood estimation for the state fidelity. We plot the likelihood density for resulting fidelities $\mathcal{F}$ and $\mathcal{F}_{\mathrm{LB}}$ for values spaced by 0.02. Thick lines are gaussian fits from which the means and standard deviations are obtained. Here we show the resulting distribution for Ψ^-, with a length of both detection windows of 38.4 ns, and a maximal window for $|\delta\tau|$ of 25.6 ns.

8.6.3 Error analysis

Spin state initialization

We initialise the electron spin of each NV in the $m_{\mathrm{s}} = 0$ ground state by optical spin pumping on the $|m_{\mathrm{s}} = \pm1\rangle \leftrightarrow |A_1\rangle$ transition. The residual population in the $m_{\mathrm{s}} = \pm1$ states can be estimated from the fluorescence time-trace obtained during the pumping as described in chapter 6.8.1. We estimate an initialisation error of $(0.61 \pm 0.05)\%$ for NV A and $(1.46 \pm 0.05)\%$ for NV B.

Spin-flips in the excited state manifold

During the two optical excitations in the entanglement protocol, a spin flip can occur due to spin-spin interactions in the excited state manifold. We can obtain an estimate of the probability of a spin-flip in the excited state from a fluorescence time-trace of the E_y transition used (see Fig. 6.1 for illustration). The time-trace is acquired while driving near saturation. Therefore we can extract both the average number of photons detected $\langle n_{\text{detected}} \rangle = A_1 t_1 + A_2 t_2$, and the detection efficiency $\eta = 2 \frac{A_1 + A_2}{\Gamma}$. Here, A_1, t_1, A_1, t_2 are the maximum amplitudes and decay times obtained from an exponential fit of the data and Γ is the NV optical decay rate. This allows us to calculate the average number of optical cycles $\langle n \rangle$ before a spin-flip occurs:

$$\langle n \rangle = \frac{\langle n_{\text{detected}} \rangle}{\eta}, \tag{8.14}$$

and finally, an estimate for the spin-flip probability per cycle $p_{\text{flip}} = \frac{1}{\langle n \rangle}$ of 0.46% ± 0.01% (0.53% ± 0.01%) for NV A (NV B). We note that p_{flip} corresponds to a crude estimate for the combined probability of a direct spin-flip due to spin mixing and a transition into the meta-stable single state.

Microwave Pulse Errors

The fidelity of the microwave (MW) π and $\pi/2$ pulses is limited by the static magnetic field applied and the hyperfine interaction with the NV host nitrogen nuclear spin. Because the nitrogen spin is not initialized, the MW pulses are randomly either on resonance or detuned by the hyperfine splitting of the ^{14}N (2.2 MHz), depending on the state of the nitrogen spin. The error due to this detuning decreases with higher Rabi frequency. In the applied static magnetic field of 17.5 G, the $m_s = +1$ transition is 98 MHz detuned from the $m_s = -1$ transition. Therefore pulses with too high Rabi frequency will populate the $m_s = +1$ level. We drive Rabi oscillations for NV A of 10 MHz, and 8.6 MHz for NV B. For NV B we apply CORPSE pulses[32] to reduce the effects of the detuning and to limit the population of the $m_s = +1$ level. For NV A we apply conventional pulses to avoid heating of the sample. We simulate the effect of the two errors on the combined state of the two NVs by numerically solving a three level driven system for the pulses used for each NV and calculating the 9×9 density matrix of the joint state. From this simulation we expect to reduce the fidelity of our final Bell State to 96.5% due to pulse errors. From the same simulation we find that the population of the $m_s = +1$ state is less than 0.4% at the end of the protocol. The pulse simulations agree with independently measured π pulse contrasts for both NVs.

Spin Coherence and Dynamical Decoupling

The main source of decoherence of the NV electron spins is the interaction with a spin bath of ^{13}C nuclear spins ($S = 1/2$). We measure a free induction decay time T_2^* of (3.07 ± 0.06) μs for NV A and (0.96 ± 0.03) μs for NV B. The spin echo of the electron spins periodically collapses and revives due to entanglement and disentanglement with the surrounding ^{13}C spins

precessing in the external field[33]. The revival amplitudes decay with a coherence time $T_2 = 687 \, \mu s$ (NV B).

For the dynamical decoupling we use a XY16 sequence[34] and choose the inter pulse delay to be twice the Larmor period of the ^{13}C spins, thus measuring always the amplitude of the revivals. When applying more than 16 pulses, the pulse errors due to off-resonant driving of the $m_s = +1$ level become significant. To circumvent this limitation we initialize the ^{14}N nuclear spin by a projective measurement[9]. This allows for a lower Rabi frequency (1.6 MHz) and therefore suppresses off-resonant driving of the $m_s = +1$ level.

Residual laser photons

After polarisation rejection and time-filtering of the reflected laser photons there is still a finite probability of detecting a laser photon. Figure 8.11 shows the combined count histogram during the first detection window on one APD, as well as the histogram counting only laser reflections, measured under similar conditions. With the chosen detection window settings there remains a $\sim 1\%$ probability that a detected photon comes from the laser instead of from either NV. Counting the possible two click events (NV+NV, NV+laser, laser+NV, laser+laser), this yields a 2% probability for a fake heralding event. Assuming that fake heralding events actually correspond to totally mixed states in the $m_s = 0$, $m_s = -1$ subspace with $\mathcal{F} = 1/4$, this yields a state infidelity of 1.5%.
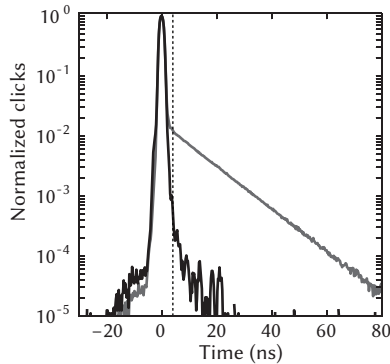
Figure 8.11 |Photon events arising from laser pulses. To estimate the remaining laser photons in the time filtered signal we compare a time trace of the combined laser reflections and NV emission (light), and a time-trace showing only the laser pulse and reflections (dark). The NV data shown corresponds to the summed histogram of a single detector of the first excitation pulse of the whole entanglement dataset. The laser-only data was taken overnight under identical conditions, but with the excitation laser far detuned from the NV resonances. For both traces background is subtracted. The dashed line marks the start of the detection window chosen.

Detector dark counts

Our detectors have been selected for low dark counts, with an average dark count rate of less than 25 Hz. Taking into account the two detection windows and the probability of detecting an NV photon, we estimate a relative probability of 1.3% for detecting a dark count. This yields a state infidelity of 2%.

Off-resonant excitation

The 2 ns optical π pulses applied have a small probability for exciting an off-resonant excited state transition. From Fig. 2a in the main text it can be seen that the nearest transition corresponding to a $m_s = -1$ spin is detuned by ~ 5 GHz. We estimate the off-resonant excitation by simulating a 4-level driven system master equation in the Born-Markov approximation. Starting with an initial superposition of two ground states corresponding to the $m_s = 0$, $m_s = -1$ levels, and two excited states corresponding to the resonantly driven $m_s = 0$ excited state level and the nearest off resonant $m_s = \pm 1$ level, we find a ~ 1% probability to excite the $m_s = -1$ state.

APD after-pulsing

With the APDs used in the experiment we observe after-pulsing, fake events that are triggered some time after the actual registration of a photon. In our entanglement scheme this can lead to fake heralding events: if a photon is detected in the detection window following the first laser pulse, there is a finite chance of obtaining a click on the same detector during the second detection not coming from a photon. Such events lower the fidelity of the produced entanglement.

We perform a control experiment to estimate the chance to detect such fake heralding events (Fig. 8.12). With the excitation laser strongly detuned from resonance we run the entanglement sequence, ideally (i.e., for no after-pulsing occurring) only expecting clicks from the laser reflection and background/dark counts. Identified after-pulsing events triggered by laser pulses are shown in Fig. 8.12a. To identify these events we assume that a click preceded by a click during a laser pulse is due to after-pulsing, neglecting the possibility of accidental double-events due to background/dark counts. This analysis implicitly includes erroneous entanglement heralding due to background/dark counts.

We obtain an estimate for the ratio of probabilities for real and fake heralding of Ψ^+ generation as follows. We compare the probability for detecting an NV photon after excitation by the second laser pulse in the entanglement measurement and the probability for registering during the same window an after-pulsing event triggered by the first laser pulse (Fig. 8.12b). For fake heralding events the after-pulsing event is triggered by an NV photon. Therefore, after-pulsing events are expected later than those triggered by the laser. We neglect this time-difference because the probability for an after-pulsing event during the detection window is almost constant.
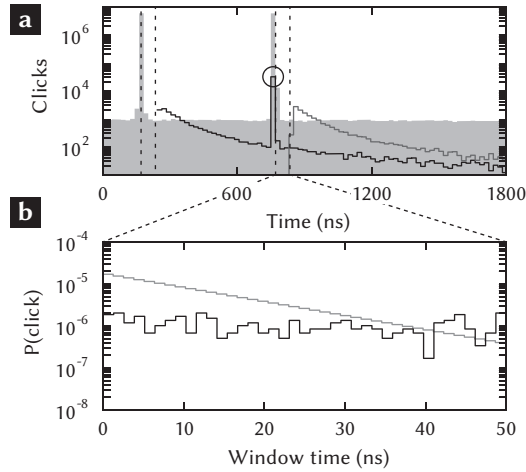
Figure 8.12 | After-pulsing. a, After-pulsing events following laser pulses, measured on one APD after the beam splitter. We identify detection events (black/grey histogram curves) that are registered after a laser photon from the first and second laser pulse, respectively. The shaded curve shows events that are not preceded by another detection event (laser photons and dark/background counts). Dashed lines mark the range used to identify entanglement events. The high probability for a click obtained during the second laser pulse after obtaining a click during the second (data point encircled) is not due to after-pulsing but due to the comparatively high probability of detecting a photon from both pulses in the same run. **b,** Detection probabilities for NV photons and after-pulsing events. The green curve shows the probability to detect in the second detection window an after-pulsing event triggered by the first laser pulse. The grey curve shows for comparison the typical probability for detection of an NV photon.

For the chosen detection window of 19.2 ns after the second excitation we find an 8.8% relative probability to measure an afterpulsing event instead of an NV photon. Assuming that fake heralding events actually correspond to totally mixed states in the $m_s = 0$, $m_s = -1$ subspace with $\mathcal{F} = 1/4$, this leads to an infidelity of 6.5%. Note that this error only applies for the Ψ^+ state.

Dephasing

The largest contribution to the state infidelity is dephasing of the produced Bell state due to distinguishability of the photons emitted by the NV centres. An estimate for the distinguishability of the photons can be gained from the two-photon interference presented in figure 2d of the main text. The interference shows a reduced visibility due to distinguishability of the photons. As explained in more detail in the section on phase evolution below, the

visibility V gives an upper bound for the Bell state fidelity: $\mathcal{F} \leq 1/2 + 1/2V$.

The photon distinguishability is likely caused by phonon-induced transitions between optically excited states, mainly in NV A, which is operated at a higher temperature. Another contribution is the resonance check performed before the entanglement protocol to ensure both NVs are on resonance: to minimise the time necessary for the resonance check, the NVs are excited with a laser power near saturation. This can however decrease the frequency-selectivity of the resonance check as the lines will be power broadened.

8.6.4   Phase evolution during the protocol

Considering all relevant phases, the quantum state of the system after the first excitation before the beam splitter is

$$
\frac{1}{2} \left[(e^{-i\omega_{\downarrow}^A t} \left|\downarrow\right\rangle_A \left|0\right\rangle_A + e^{-i\omega_{\uparrow}^A t} \left|\uparrow\right\rangle_A e^{ik_A x_A - i\omega_A \tau} \left|1\right\rangle_A) \right. \tag{8.15}
$$
$$
\left. \otimes (e^{-i\omega_{\downarrow}^B t} \left|\downarrow\right\rangle_B \left|0\right\rangle_B - e^{-i\omega_{\uparrow}^B t} \left|\uparrow\right\rangle_B e^{ik_B x_B - i\omega_B \tau} \left|1\right\rangle_B) \right],
$$

where $\omega_{\downarrow_i}$ and $\omega_{\uparrow_i}$ correspond to the energy levels for the two ground states $\{\left|\downarrow\right\rangle, \left|\uparrow\right\rangle\}$. ω is the transition frequency from the excited state $\left|e\right\rangle$ to the corresponding ground state and k the corresponding wavenumbers $k = \omega/c$. x is the photon path length from the NV-centre to the beam splitter, the time t corresponds to the time after the first MW $\pi/2$ pulse and time τ to the time after the excitation pulse. The labels $\{A, B\}$ denote the two NV centres. See also Fig. 8.13.

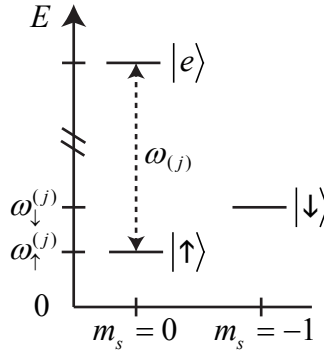**Figure 8.13 | Energy levels.** Schematic showing the energy levels involved in the protocol, and the definitions for the various frequencies ω involved, where j labels the NV centre $j \in \{A,B\}$.

After a single click in one of the output ports of the beam-splitter at a time $\tau_1 > k_A x_A, k_B x_B$ after the excitation (caused by one or two photons in that port), the two NV spins are projected

onto the mixed state

$$|\alpha|^2 \, |\psi^\pm\rangle_{AB} \, \langle\psi^\pm|_{AB} + |\beta|^2 \, |{\uparrow}\rangle_A \, |{\uparrow}\rangle_B \, \langle{\uparrow}\,|_A \langle{\uparrow}\,|_B, \qquad (8.16)$$

with the $(-)$-sign if we detect a click on the detector on output port 1 and a $(+)$ for a click on 2, and amplitudes α, β depending on the collection efficiencies for NV A and B, respectively. $|\psi^\pm\rangle_{AB}$ is an entangled state, with, at time t_{MW} after the first MW $\pi/2$-pulse, the following phase relations:

$$|\psi^\pm\rangle_{AB} = \frac{1}{\sqrt{2}} \left[e^{-i\omega_\downarrow^A t_{MW}} |{\downarrow}\rangle_A \, e^{-i\omega_\uparrow^B t_{MW}} |{\uparrow}\rangle_B \cdot e^{ik_B x_B - i\omega_B \tau_1} \right.$$
$$\left. \pm \quad e^{-i\omega_\uparrow^A t_{MW}} |{\uparrow}\rangle_A \, e^{-i\omega_\downarrow^B t_{MW}} |{\downarrow}\rangle_B \cdot e^{ik_A x_A - i\omega_A \tau_1} \right]. \qquad (8.17)$$

Here we have assumed identical NV-optical lifetimes Γ^{-1} and identical path-lengths from the beam splitter to the two different detectors, for simplicity.

At this time, the MW π-pulse is applied, flipping all $|{\downarrow}\rangle \longleftrightarrow |{\uparrow}\rangle$ in Eqns. (8.16), (8.17). Then the second excitation round proceeds, and after again detecting a single click in one of the output ports of the beam-splitter at a time $\tau_2 > k'_A x'_A, k'_B x'_B$, the two NV spins are projected onto the pure state:

$$\frac{1}{\sqrt{2}} \left[e^{-i\omega_\downarrow^A t_{MW}} e^{-i\omega_\uparrow'^A t_{MW}} |{\uparrow}\rangle_A \, e^{-i\omega_\uparrow^B t_{MW}} e^{-i\omega_\downarrow'^B t_{MW}} |{\downarrow}\rangle_B \right.$$
$$\times \quad e^{ik_B x_B - i\omega_B \tau_1} e^{ik'_A x'_A - i\omega'_A \tau_2}$$
$$\pm \quad e^{-i\omega_\uparrow^A t_{MW}} e^{-i\omega_\downarrow'^A t_{MW}} |{\downarrow}\rangle_A \, e^{-i\omega_\downarrow^B t_{MW}} e^{-i\omega_\uparrow'^B t_{MW}} |{\uparrow}\rangle_B$$
$$\left. \times \quad e^{ik_A x_A - i\omega_A \tau_1} e^{ik'_B x'_B - i\omega'_B \tau_2} \right], \qquad (8.18)$$

at the spin-echo time $t = 2 \times t_{MW}$ after the first MW $\pi/2$-pulse. Here we have denoted variables corresponding to physical quantities during the second round with a prime ('). The $(+)$-sign corresponds to a click in the same detectors, the $(-)$-sign to different detectors.

The phase of the final entangled in Eq. (8.18) contains terms that oscillate with the photon frequency. To produce useful entanglement, a stable phase is required, suggesting that spatial interferometric stability of the setup and prohibitively small detector time jitter are needed.

However, the time T between the two excitation rounds is short ($T = 600$ ns) compared to many environmental drifts of e.g. the optical path lengths and electric and magnetic fields. This suggests we should consider certain assumptions about the relation between the physical quantities in the first and second excitation rounds. In particular, possible assumptions are:

1. $\omega_\uparrow = \omega'_\uparrow$ and $\omega_\downarrow = \omega'_\downarrow$, requiring stability of the magnetic field as felt by the NV centre on the time-scale T. From independent spin-echo measurements in e.g. figure 1b in the main text we know that this assumption satisfied.

2. $x = x'$ requiring stability of the setup on the order of a wavelength (637 nm) on the time-scale T. With T being only 600ns, the setup is expected to be stable.

3. $\omega = \omega'$ (and therefore also $k = k'$). This assumption is harder to justify by independent measurement, and in fact would not be satisfied if phonon-induced transitions occur in the excited state.

If all three assumptions are satisfied, the phase relation in Eq. (8.18) simplifies:

$$\frac{1}{\sqrt{2}} \left(|\downarrow\uparrow\rangle_{AB} \pm e^{i\varphi} |\uparrow\downarrow\rangle_{AB} \right), \tag{8.19}$$

with

$$\varphi(\tau_1, \tau_2) = (\tau_2 - \tau_1)(\omega_A - \omega_B), \tag{8.20}$$

so that the overlap with the wanted Bell states is:

$$F(\varphi) = \frac{1}{2} + \frac{1}{2} \cos(\varphi). \tag{8.21}$$

This analysis shows that whenever the two NV centres are on resonance, perfect state fidelity could be obtained independent of the photon arrival times. Also, if the photon arrival times are identical, no dephasing is present independent of the detuning between the NV centres' optical frequencies.

8.6.5 Relation to TPQI visibility

Following Legero *et al.*[35], we have for the two-photon correlation function $g^{(2)}(t_1, t_2)$ of two photons with identical polarisation exiting from the beam-splitter:

$$g^{(2)}(t_1, t_2) = \frac{1}{4} |\xi_A(t_1)\xi_B(t_2) - \xi_B(t_1)\xi_A(t_2)|, \tag{8.22}$$

where $\xi(t)$ describes the spatio-temporal mode of the state of a single-photon light field, at time t. When these modes are written as the product of a real amplitude and a complex phase, $\xi_i(t) = \epsilon_i(t) \exp[-i\phi_i(t)]$, the correlation above function can be rewritten:

$$g^{(2)}(t_1, t_2) = g^{(2)}_\perp(t_1, t_2) - K(t_1, t_2). \tag{8.23}$$

Here, $g^{(2)}_\perp(t_1, t_2)$ is the correlation function for two fully distinguishable (perpendicularly polarised) single photons,

$$g^{(2)}_\perp(t_1, t_2) = \frac{1}{4} \left((\epsilon_A(t_1)\epsilon_B(t_2))^2 + (\epsilon_A(t_2)\epsilon_B(t_1))^2 \right), \tag{8.24}$$

which is independent of the phases ϕ. $K(t_1, t_2)$, however, does depend on the phase:

$$K(t_1, t_2) = \frac{1}{2}(\epsilon_A(t_1)\epsilon_B(t_2)\epsilon_A(t_2)\epsilon_B(t_1)) \cos(\phi_A(t_1) - \phi_A(t_2) + \phi_B(t_2) - \phi_B(t_1)). \tag{8.25}$$

Finally, the visibility of the two photon interference is given by

$$V(t_1, t_2) = \frac{g_\perp^{(2)} - g^{(2)}}{g_\perp^{(2)}} = K/g_\perp^{(2)}. \tag{8.26}$$

Relating the above to photons emitted by our two NV centres in the situation in our experiment, and assuming the excitation time t_0, we have

$$\epsilon_i(t) = \Gamma \exp[\Gamma(t - t_0 - x_i/c)], \tag{8.27}$$

where we have assumed as before identical optical lifetime Γ^{-1} for the both NV's. Furthermore:

$$\phi_i(t) = (t - t_0)\omega_i - k_i x_i. \tag{8.28}$$

In this case, $V(t_1, t_2)$ above reduces to

$$V(t_1, t_2) = \cos[(t_2 - t_1)(\omega_A - \omega_B)]. \tag{8.29}$$

Comparing this result with Eqns. (8.20),(8.21) above, we have $\frac{1}{2} + \frac{1}{2}V(dt) = F(\varphi(\delta\tau))$, with - as before - $dt = t_2 - t_1$ and $\delta\tau = \tau_2 - \tau_1$. Since rejecting any of the assumptions (1-3) made in the previous section to arrive at the simplified expression for F will in general decrease the fidelity, V sets an upper limit for the fidelity overlap with the Bell states.

8.7 Bibliography

[1]   M. A. Nielsen and I. L. Chuang. *Quantum Computation and Quantum Information.* Cambridge University Press (2000).

[2]   R. Raussendorf and H. J. Briegel. A One-Way Quantum Computer. *Phys. Rev. Lett.* **86**, 5188 (2001).

[3]   D. L. Moehring *et al.* Entanglement of single-atom quantum bits at a distance. *Nature* **449**, 68 (2007).

[4]   S. Ritter *et al.* An elementary quantum network of single atoms in optical cavities. *Nature* **484**, 195 (2012).

[5]   J. Hofmann *et al.* Heralded Entanglement Between Widely Separated Atoms. *Science* **337**, 72 (2012).

[6]   H. J. Kimble. The quantum internet. *Nature* **453**, 1023 (2008).

[7]   L. M. Duan, M. D. Lukin, J. I. Cirac and P. Zoller. Long-distance quantum communication with atomic ensembles and linear optics. *Nature* **414**, 413 (2001).

[8]   L. Childress, J. M. Taylor, A. S. Sørensen and M. D. Lukin. Fault-Tolerant Quantum Communication Based on Solid-State Photon Emitters. *Phys. Rev. Lett.* **96**, 070504 (2006).

[9]   L. Robledo *et al.* High-fidelity projective read-out of a solid-state spin quantum register. *Nature* **477**, 574 (2011).

[10] P. Neumann *et al.* Single-Shot Readout of a Single Nuclear Spin. *Science* **329**, 542 (2010).

[11] P. Neumann *et al.* Multipartite Entanglement Among Single Spins in Diamond. *Science* **320**, 1326 (2008).

[12] P. C. Maurer *et al.* Room-Temperature Quantum Bit Memory Exceeding One Second. *Science* **336**, 1283 (2012).

[13] W. Pfaff *et al.* Demonstration of entanglement-by-measurement of solid-state qubits. *Nature Physics* **9**, 29 (2013).

[14] T. D. Ladd *et al.* Quantum computers. *Nature* **464**, 45 (2010).

[15] E. Togan *et al.* Quantum entanglement between an optical photon and a solid-state spin qubit. *Nature* **466**, 730 (2010).

[16] W. B. Gao, P. Fallahi, E. Togan, J. Miguel-Sanchez and A. Imamoglu. Observation of entanglement between a quantum dot spin and a single photon. *Nature* **491**, 426 (2012).

[17] K. De Greve *et al.* Quantum-dot spin–photon entanglement via frequency downconversion to telecom wavelength. *Nature* **491**, 421 (2012).

[18] H. Bernien *et al.* Two-Photon Quantum Interference from Separate Nitrogen Vacancy Centers in Diamond. *Phys. Rev. Lett.* **108**, 043604 (2012).

[19] A. Sipahigil *et al.* Quantum Interference of Single Photons from Remote Nitrogen-Vacancy Centers in Diamond. *Phys. Rev. Lett.* **108**, 143601 (2012).

[20] R. B. Patel *et al.* Two-photon interference of the emission from electrically tunable remote quantum dots. *Nature Photon.* **4**, 632 (2010).

[21] E. B. Flagg *et al.* Interference of Single Photons from Two Separate Semiconductor Quantum Dots. *Phys. Rev. Lett.* **104**, 137401 (2010).

[22] G. D. Fuchs, V. V. Dobrovitski, D. M. Toyli, F. J. Heremans and D. D. Awschalom. Gigahertz Dynamics of a Strongly Driven Single Quantum Spin. *Science* **326**, 1520 (2009).

[23] G. de Lange, Z. H. Wang, D. Ristè, V. V. Dobrovitski and R. Hanson. Universal Dynamical Decoupling of a Single Solid-State Spin from a Spin Bath. *Science* **330**, 60 (2010).

[24] T. van der Sar *et al.* Decoherence-protected quantum gates for a hybrid solid-state spin register. *Nature* **484**, 82 (2012).

[25] S. D. Barrett and P. Kok. Efficient high-fidelity quantum computation using matter qubits and linear optics. *Phys. Rev. A* **71**, 060310 (2005).

[26] L. C. Bassett, F. J. Heremans, C. G. Yale, B. B. Buckley and D. D. Awschalom. Electrical Tuning of Single Nitrogen-Vacancy Center Optical Transitions Enhanced by Photoinduced Fields. *Phys. Rev. Lett.* **107**, 266403 (2011).

[27] L. Robledo, H. Bernien, I. van Weperen and R. Hanson. Control and Coherence of the Optical Transition of Single Nitrogen Vacancy Centers in Diamond. *Phys. Rev. Lett.* **105**, 177403 (2010).

[28] C. K. Hong, Z. Y. Ou and L. Mandel. Measurement of subpicosecond time intervals between two photons by interference. *Phys. Rev. Lett.* **59**, 2044 (1987).

[29] K.-M. C. Fu *et al.* Observation of the Dynamic Jahn-Teller Effect in the Excited States of Nitrogen-Vacancy Centers in Diamond. *Phys. Rev. Lett.* **103**, 256404 (2009).

[30] I. Aharonovich, A. D. Greentree and S. Prawer. Diamond photonics. *Nature Photon.* **5**, 397 (2011).

[31] J. K. Lindsey. *Parametric Statistical Inference.* Clarendon Press, Oxford, UK (1996).

[32] H. K. Cummins, G. Llewellyn and J. A. Jones. Tackling systematic errors in quantum logic gates with composite rotations. *Phys. Rev. A* **67**, 42308 (2003).

[33] L. Childress *et al.* Coherent dynamics of coupled electron and nuclear spin qubits in diamond. *Science* **314**, 281 (2006).

[34] T. Gullion, D. B. Baker and M. S. Conradi. New, compensated carr-purcell sequences. *J. Magn. Reson.* **89**, 479 (1990).

[35] T. Legero, T. Wilk, A. Kuhn and G. Rempe. Characterization of Single Photons Using Two-Photon Interference. M. O. Scully and G. Rempe (editors), *Advances In Atomic, Molecular, and Optical Physics*, Academic Press, 253–289 (2006).

Deterministic quantum teleportation between remote solid-state qubits

W. Pfaff, B. Hensen, H. Bernien, S. van Dam, M.S. Blok, T.H. Taminiau, M.J. Tiggelman,
R.S. Schouten, M. Markham, D.J. Twitchen, and R. Hanson

Quantum teleportation allows for transfering arbitrary quantum states between remote parties that share an entangled state as resource. Such teleportation is an essential ingredient for the operation of a quantum network. Here we demonstrate deterministic teleportation of the quantum state of a nuclear spin onto an electronic spin over three metres. We combine the previously attained remote entanglement between two NV electronic spins with a local Bell-state measurement that acts on one of the entangled electronic spins and a source qubit encoded in a nuclear spin. This scheme allows us to teleport a source state prepared on the nuclear spin onto the remote electronic spin with a fidelity that clearly exceeds the classically allowed value. Our result shows that the NV is a prime candidate for the realisation of a macroscopic quantum network.

9.1 Introduction

Quantum teleportation allows the transfer of arbitrary, unknown quantum states between two parties that share an entangled pair and can communicate classically[1]. Teleportation has been suggested for remote quantum communication[2] as well as for the realisation of gates in measurement-bases quantum computing schemes[3], and thus is a promising tool for the creation and operation of quantum networks.

Qubit teleportation can be achieved using entanglement as a resource in the following way[1]: An entangled Einstein-Podolsky-Rosen (EPR) pair is shared between a sender (Alice) and a receiver (Bob). Alice, who is in possession of the source qubit in state $|\psi\rangle$ to be transmitted to Bob, performs a joint measurement on the source qubit and her half of the EPR pair. The measurement transforms the state of Bob's half of the EPR pair such that it is related to the source state by a unitary transformation that depends on the measurement outcome. Alice sends this information classically to Bob, who is then in possession of a pure state that is — up to a basis rotation — equal to the original source state.

Early demonstrations showed that teleportation over macroscopic distances can be achieved in practice for photonic[4] as well as for stationary matter qubits[5]. However, these proof-of-principle experiments were not deterministic, i.e., the entanglement was consumed most of the times without resulting in a successfully teleported state on Bob's side, and the source state was lost.

The teleportation is deterministic if it succeeds with unit probablity, regardless of the outcome of Alice's joint measurement — this has the great advantage that each successful generation of an EPR pair results with certainty in transmission of the source state. Deterministic qubit teleportation has been demonstrated previously between ions within one trap[6,7], superconducting qubits on the same chip[8], and photonic qubits[9]. Here we aim to demonstrate deterministic teleportation between remote scalable quantum registers that are separated by a distance of several metres.

For our implementation we choose spins in diamond that are associated to single NV color defects as qubits. The NV centre has a long-lived electronic spin ($S = 1$) that can be used as a spin qubit[10–12]. Nuclear spins surrounding the defect can be used in quantum registers[13,14]. Furthermore, the NV centre provides an optical interface that can be used to perform quantum measurements on the electron spin as well as on a quantum register of nuclear spin qubits[15,16], and is suited for the generation of entanglement between remote electron spins[17,18]. The combination of these features makes the NV centre an attractive system of choice for the implementation of deterministic remote teleportation.

9.2 Protocol

Alice and Bob are two NV centres in diamond samples cooled to liquid helium temperatures, located in two different cryogenic confocal microscope setups at a distance of about 3 metres

(Fig. 9.1a). The source qubit is the NV ^{14}N nuclear spin on Alice's side. The EPR pair is created with the two NV electronic spins on Alice's and Bob's sides. Both setups can be operated independently: the spins can be read out in a single shot by spin-resolved optical excitation[15], and manipulated individually by microwave (MW) and radio-frequency (RF) pulses applied via on-chip strip lines.

Remote entanglement between the two NV electron spins can be created using quantum interference of indistinguishable photons from the zero phonon lines (ZPLs) on a beam splitter. For the creation of such photons we tune Alice's E_y transition on resonance with Bob's E_y transition using the d.c. Stark effect by applying a voltage on an on-chip gate-electrode[18]. Heralded entanglement is then generated by interference and measurement of ZPL photons from the E_y transistions that are correlated with the electron spin states[18].

We implement deterministic teleportation as follows (Fig. 9.1b). We bring Alice's nuclear spin into $|1\rangle$ by a projective measurement[15,16], and both electron spins into $|0\rangle$ by optical spin pumping[15]. Following this intialisation we create remote entanglement between the electron spins probabilistically[18,19], and prepare the source state $|\psi\rangle = \alpha |0\rangle + \beta |1\rangle$ on Alice's nuclear spin. The prepared state has the form

$$(\alpha |0\rangle + \beta |1\rangle)(|01\rangle \pm |10\rangle)/\sqrt{2}, \tag{9.1}$$

where the first qubit is the nuclear source qubit, and the second and third qubits are Alice's and Bob's electronic spins, respectively.

The key operation for teleportation is a joint measurement in the Bell-basis on the source qubit and one of the two entangled qubits. A two-qubit Bell-state measurement can be implemented by performing a controlled-NOT (CNOT) gate, followed by a Hadamard gate on the control qubit and subsequent readout of both qubits[20]. In the following we will assume that the entangled state between the two electron spins is $|\Psi^-\rangle = (|01\rangle - |10\rangle)/\sqrt{2}$; for $|\Psi^+\rangle = (|01\rangle + |10\rangle)/\sqrt{2}$, the treatment is similar. After an inversion of Alice's electron spin conditional on the nuclear spin state $|1\rangle$, followed by a Hadamard gate on the nuclear spin, the total state of the system can be written as

$$\begin{aligned}
\frac{1}{2}\Big(&|00\rangle \left(-\beta |0\rangle + \alpha |1\rangle\right) \\
&+ |01\rangle \left(-\alpha |0\rangle + \beta |1\rangle\right) \\
&+ |10\rangle \left(\beta |0\rangle + \alpha |0\rangle\right) \\
&- |11\rangle \left(\alpha |0\rangle + \beta |1\rangle\right)\Big).
\end{aligned} \tag{9.2}$$

From equation (9.2) it becomes clear that depending on the measurement outcome $|ij\rangle$ obtained on Alice's nuclear and electron spin, respectively, the state of Bob's electronic spin,
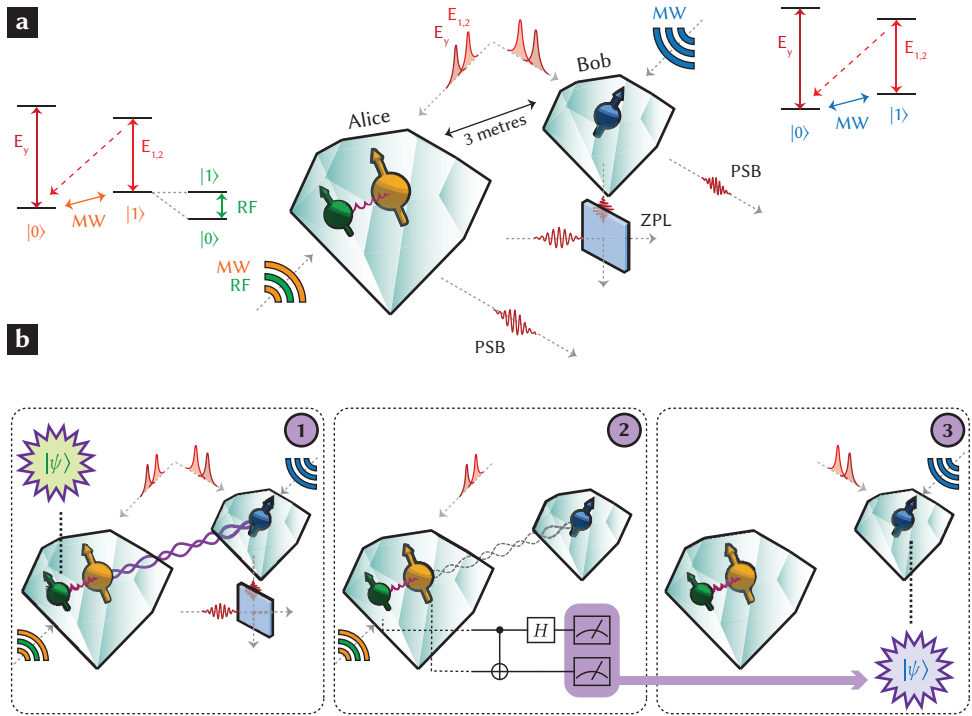
Figure 9.1 | Deterministic teleportation between remote spins in diamond. a, Alice and Bob are NV centres in two remote diamond samples. The electronic spins of the two NVs can be prepared into $|0\rangle \equiv m_s = 0$ by optical spin-pumping on the $E_{1,2}$ transitions. Single shot readout of the electron spin is performed by spin-resolved optical excitation on E_y detecting fluorescence from the NV centre's phonon side band (PSB). The spectrally separated zero phonon line (ZPL) emission is used to create remote entanglement by two-photon quantum interference on a beam splitter. High-fidelity manipulation between $|0\rangle$ and $|1\rangle \equiv m_s = -1$ is achieved by microwave (MW) pulses. The source qubit is Alice's ^{14}N nuclear spin, with basis states $|0\rangle \equiv m_I = 0$, and $|1\rangle \equiv m_I = -1$, defined in the $m_s = -1$ manifold. It can be initialised by projective measurement and manipulated by radio-frequency (RF) pulses. **b,** Outline of the teleportation protocol. *(1)* Using electron spin rotations and optical π-pulses the two electronic spins are prepared in an entangled state using the Barrett-Kok protocol by detection of indistinguishable ZPL photons from both NVs that are interfered on a beam splitter; the nitrogen spin is prepared in the source state $|\psi\rangle$. *(2)* We perform a two-qubit Bell-state measurement on Alice's qubits. The result of the Bell-state measurement is fed forward in real time to Bob, *(3)* where a basis rotation is performed conditional on the measurement result. Optical readout allows to determine the fidelity with the source state.

$|\psi\rangle_{ij}$, is

$$
\begin{aligned}
|\psi\rangle_{00} &= Y^\dagger \, |\psi\rangle \,, \\
|\psi\rangle_{01} &= Z^\dagger \, |\psi\rangle \,, \\
|\psi\rangle_{10} &= Z^\dagger Y^\dagger \, |\psi\rangle \,, \\
|\psi\rangle_{11} &= \mathbb{1} \, |\psi\rangle \,.
\end{aligned}
\tag{9.3}
$$

Y and Z denote π-rotations around the y and z axes, respectively. This state of the target qubit is thus equal to the source state up to a basis rotation that depends on the BSM outcome.

We achieve teleportation by performing a unitary operation on the target qubit conditional on the result of the BSM (feed-forward) before readout. Crucially, each run of the BSM results in an outcome and a feed-forward operation, making the teleportation deterministic. We determine the success of the protocol by using the six source states $|\psi\rangle = \{|\pm X\rangle, |\pm Y\rangle, |\pm Z\rangle\}$ as inputs [21], where $|+Z\rangle = |0\rangle$, $|-Z\rangle = |1\rangle$, $|\pm X\rangle = (|0\rangle \pm |1\rangle)/\sqrt{2}$, and $|\pm Y\rangle = (|0\rangle \pm i\,|1\rangle)/\sqrt{2}$. An average fidelity of the target state with respect to the source state of $\mathcal{F} > 2/3$ proves successful teleportation [22].

9.3 Implementation

The crucial technical challenge for implementing this protocol is the preservation of qubit states during the operations required. In particular, we need to (1) preserve the ^{14}N source qubit while generating entanglement between the two electronic spins; (2) perform the BSM on Alice's nuclear and electron spin qubits that differ in manipulation and coherence times by about four orders of magnitude; (3) at the same time preserve the state of Bob's electron spin qubit before the result of the BSM is available for feed-forward.

9.3.1 System initialisation

We prepare the system as shown in Fig. 9.2: Our protocol first ensures that both NVs are in their negatively charged state and that our lasers are on resonance with the optical transitions used (Fig. 9.2a). The next step is to create entanglement between the electronic spins and to prepare Alice's nuclear spin in the source state.

Each attempt to generate entanglement between the electronic spins consists of preparation into $|0\rangle$ by optical spin-pumping followed by two rounds of spin-rotation by microwaves and spin-selective optical excitation (Fig. 9.2c), conducted simultaneously on Alice's and Bob's sides [18,19]. Each attempt takes on the order of $10\,\mu s$ and results in heralded entanglement with a success probability of $\sim 10^{-7}$. To avoid disturbance of Alice's nuclear spin we keep it in an eigenstate, created by measurement-based initalisation, during entanglement generation (Fig. 9.2b). By doing so we are able to prevent dephasing caused by optical spin-pumping of the electronic spin. We further preserve the purity of the state by re-initialising after every 250 failed entanglement generation attempts (Supporting Material).
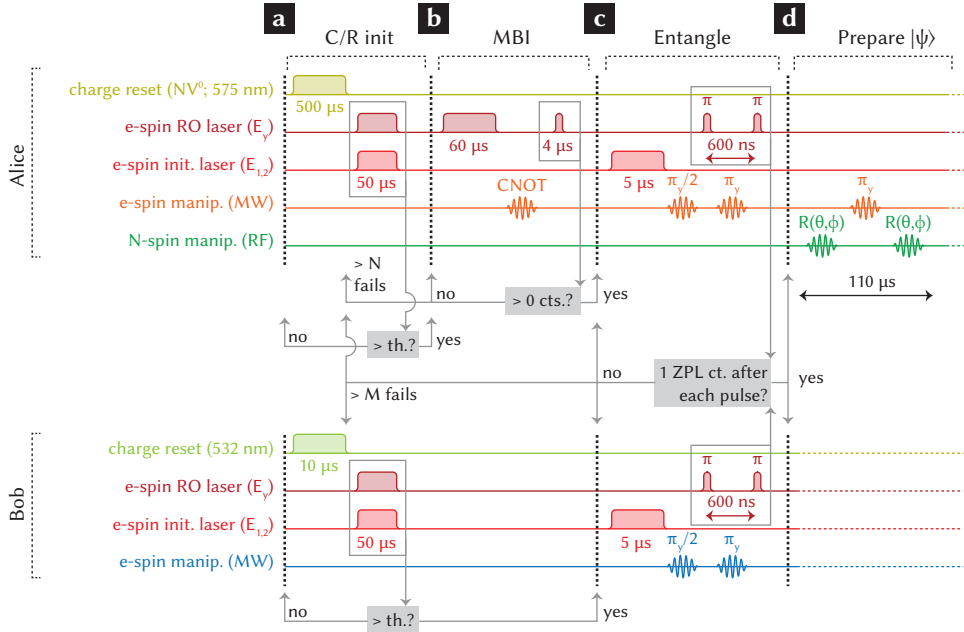
Figure 9.2 | System initialisation. a, We verify charge and resonance condition of Alice and Bob (asynchronously) by applying laser pulses on E_y and $E_{1,2}$ simultaneously and putting a lower threshold on the number of PSB photons detected during those pulses. If the threshold is not met we reset the charge state: On Alice, we repump $NV^0 \rightarrow NV^-$ using a laser at 575 nm, on resonance with the ZPL of NV^0 [23]. On Bob, we use off-resonant excitation at 532 nm. We repeat verification and repump until success. **b,** Following spin-pumping into $m_s = \pm 1$ by excitation of E_y we apply a CNOT on the electronic spin, such that only $m_I = -1$ is rotated to $m_s = 0$. A PSB photon detected during a short readout pulse on E_y signals a high-fidelity measurement of $m_s = 0$ and projection of the nuclear spin into $m_I = -1$. If no photon is detected, we re-try for a maximum of N times (here, $N = 100$), before charge and resonance are re-evalutated. **c,** As soon as both Alice and Bob are initialised, we attempt to generate entanglement between them. Each attempt starts with an electron spin reset to $m_s = 0$. Two rounds of optical excitation with optical π-pulses on E_y follow, separated by MW π-pulse. Detection of exactly one ZPL photon after each pulse heralds creation of entanglement. We perform a maximum of M attempts before re-initialisation (here, $M = 250$). **d,** When entanglement is created, we prepare the ^{14}N spin of Alice unconditional on the electron spin state, while preserving the electron spin phase. The RF pulse that generates the rotation is only resonant for $m_s = -1$; we perform the rotation twice, separated by a π-pulse on the electron.

As soon as the entanglement generation succeeds, we prepare the source state $|\psi\rangle$ (Fig. 9.2d). We perform this operation unconditionally on the electron state being either $m_s = 0$ or $m_s = -1$. To this end we apply the corresponding RF pulse that is resonant with the qubit transition in $m_s = -1$ twice, separated by an electron π-pulse. This procedure additionally protects the electronic spin from dephasing by a spin-echo [12].

9.3.2 Bell-state measurement

The basic principle for the two-qubit BSM on Alice's side is shown in Fig. 9.3a: We perform a rotation of π on the electronic spin qubit, conditional on the nuclear spin qubit being in $|1\rangle$. After that a Hadamard gate acts on the nuclear spin, before finally both qubits are measured. The main characteristic of this procedure is that it maps each input Bell state, $|\Phi^{\pm}\rangle = (|00\rangle \pm |11\rangle)/\sqrt{2}$ and $|\Psi^{\pm}\rangle = (|01\rangle \pm |10\rangle)/\sqrt{2}$, onto a different two-qubit measurement outcome $|ij\rangle$ ($i, j \in \{0, 1\}$). The BSM outcome is fed forward to Bob's electronic spin, where an operation of the form $Y^j Z^i$ recovers the source state $|\psi\rangle$ (see Supporting Material).

Our actual implementation of this scheme is shown in Figs. 9.3b,c. Following the CNOT gate we perform an unconditional $\pi/2$ rotation on the nuclear spin, replacing the Hadamard gate (Supporting Material). We then read out the electron spin in a single shot by spin-resolved optical excitation on E_y [15]. The readout of the nuclear spin is performed after that, by first mapping the nuclear spin states $|0\rangle$, $|1\rangle$ onto the electronic spin states $m_s = 0, m_s = -1$, respectively, by a conditional electron spin rotation and then reading out the electron again. The number of phonon side band photons detected during the readout pulses determine the result of the BSM.

We characterise the BSM using Bell states created by electron spin rotations conditional on the nuclear spin state (Fig. 9.3d). Each Bell state results in a different two-qubit measurement outcome for the nitrogen and electron spins, respectively. We estimate a fidelity of the Bell state measurement, given by the probability to obtain the ideal measurement outcome, of $\mathcal{F}_{BSM} = (89 \pm 2)\%$ (not corrected for nuclear spin initialisation or preparation of the states used to characterise the BSM). The fidelity is limited mainly by the single-shot readout fidelity of the electronic spin, with a mean fidelity of $\mathcal{F}_{RO} \approx 96\%$.

9.3.3 Feed-forward and readout of Bob's state

During the source state preparation and BSM (lasting $\geq 200\,\mu s$) we protect the phase of Bob's electronic spin against dephasing by an XY4 dynamical decoupling sequence [11]. This sequence is sufficiently long for us to obtain the BSM result and initiate the correct feed-forward operation on Bob's side. At the time at which the feed-forward operation is to be performed we find that an intial superposition state of Bob's electronic spin is preserved with a fidelity of 0.96 ± 0.01. As soon as the result of the BSM is available, we trigger a unitary operation performed on Bob's electron spin that is conditional on the BSM outcome, transforming Bob's state into the readout basis (Z-basis), which is universal to all BSM outcomes. This step is a genuine feed-forward operation required for the demonstration of
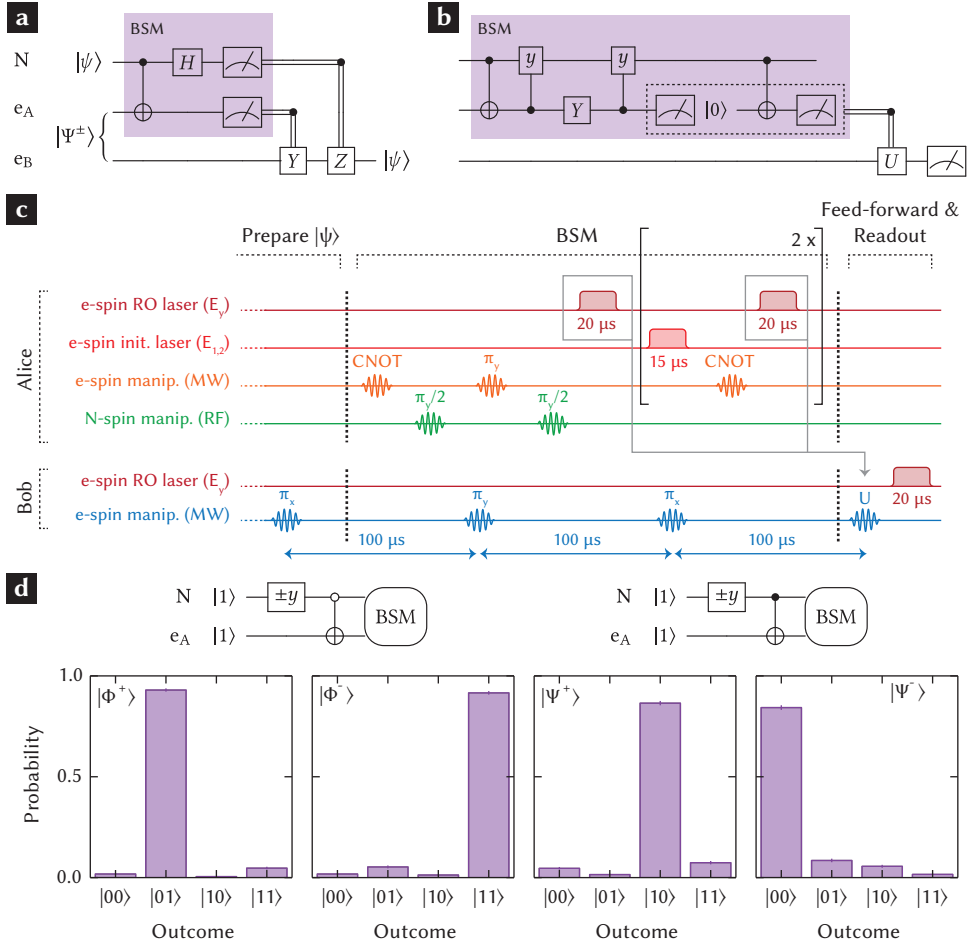
Figure 9.3 | Bell-state measurement and feed-forward. a, Circuit-diagram for the basic scheme. The shaded region marks the Bell-state measurement. **b,** Actual implementation. The nuclear spin is rotated unconditionally by performing the corresponding pulse twice, with a π-pulse applied on the electron in between. Read out of the nitrogen spin is performed via the electron after measuring and resetting the electron spin first. **c,** Corresponding pulse scheme. Note that we perform repetitive readout (2 repetitions) of the nuclear spin to obtain a higher readout fidelity [15]. **d,** Characterisation of the Bell-state measurement. We create each of the four Bell-states, $|\Phi^{\pm}\rangle = (|00\rangle \pm |11\rangle)/\sqrt{2}$ and $|\Psi^{\pm}\rangle = (|01\rangle \pm |10\rangle)/\sqrt{2}$ with conditional electron spin rotations and perform the BSM, mapping each Bell-state onto a different two-qubit measurement result. Error bars are one statistical standard deviation.

deterministic teleportation. We finally read out Bob's state in a single shot by spin-resolved optical excitation on E_y.

9.4   Preliminary result and conclusion

Preliminary analysis of the state-fidelities of the six mutually unbiased basis states with respect to the ideal states is shown in Fig. 9.4a. We find an average state fidelity of $\mathcal{F}$ = 0.77 ± 0.03, violating the classical of limit of 2/3 by more than three standard deviations. This result clearly shows the quantum nature of the teleportation scheme. We note that the data has not been corrected for initialisation errors, which we estimate to be on the order of $\sim 10\%$ (Supporting Material). This value is therefore a lower bound on the actual teleportation fidelity. Furthermore, we perform quantum state tomography on the teleported state $|Y\rangle$ (Fig. 9.4b).

In conclusion, we have demonstrated deterministic teleportation between remote solid-state qubits. Our protocol unifies our recent results of long-distance entanglement[18], quantum measurements on electron and nuclear spins[15,16], and decoherence protection[11,12] in a single experiment.

The NV's hybrid nature, consisting of a electronic interface qubit and nuclear storage qubits, allows us to perform remote entanglement generation while keeping a nuclear spin in a well-defined state. Vice versa, we are able to keep the entanglement while performing a joint measurement on electronic and nuclear spin locally. This result demonstrates the great potential of the NV centre as a platform for large-scale quantum networks.
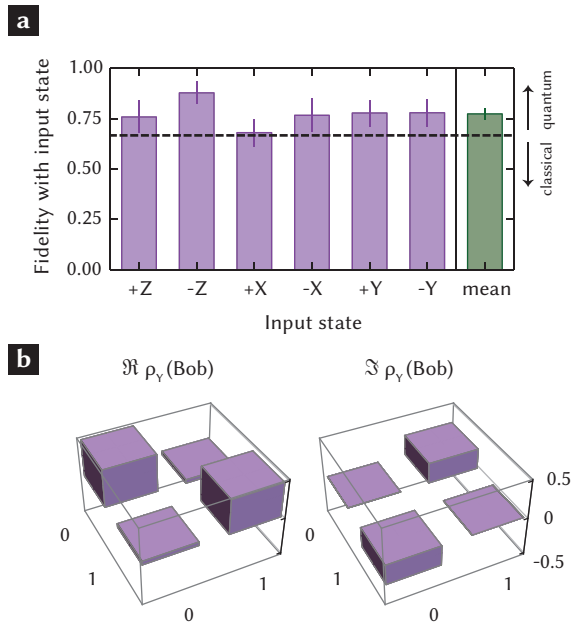
Figure 9.4 | Characterisation of the teleported state. a, Teleportation fidelity. The fidelity for each input state is determined unconditionally on the BSM outcomes. The mean fidelity is $\mathcal{F} = (0.77 \pm 0.03)$. The dashed line marks the classical limit of 2/3. The data has been corrected only for Bob's single-shot readout infidelity [18]. Error bars are one standard deviation, sample sizes for the individual input states $|+Z\rangle, |-Z\rangle, |+X\rangle, |-X\rangle, |+Y\rangle, |-Y\rangle$ are 54, 89, 73, 49, 52, and 47, respectively. **b,** State estimation for input state $|+Y\rangle$. We estimate the density matrix ρ_Y on Bob's side (real part on the left, imaginary part on the right) from measurements of the expectation values $\langle X \rangle$, $\langle Y \rangle$, and $\langle Z \rangle$. The elements of the density matrix of the ideal state are $\rho_{00} = 0.5$, $\rho_{01} = 0.5i$, $\rho_{10} = -0.5i$, and $\rho_{11} = 0.5$.

9.5   Supporting Material

Conventions

Basis states

The basis states used for the electrons are $|0\rangle = |m_s = 0\rangle$ and $|1\rangle = |m_s = -1\rangle$. For the nitrogen, $|0\rangle = |m_I = 0\rangle$ and $|1\rangle = |m_I = -1\rangle$. When specifying joint quantum states, the first qubit is the nitrogen on site A, the second the electron on site A, and the third the electron on site B. Teleportation is therefore to be performed from qubit 1 onto qubit 3.

Gates

By x, y, z we denote $\pi/2$ rotations around the $+X, +Y, +Z$ axes respectively. Bars over gate symbols indicate negative rotation sense. In the measurement sequences, rotations around $+X, +Y$ correspond to phases of the applied driving pulses of $+90°$ and $0°$, respectively. We prepare $|x\rangle \equiv |0\rangle + |1\rangle$ by $y|0\rangle$ and $|y\rangle \equiv |0\rangle + \mathrm{i}|1\rangle = \bar{x}|0\rangle$. Capital letters X, Y, Z indicate π rotations.

Hamiltonian of Alice

The relevant energy levels of the electron and nuclear spins of Alice are depicted in Fig. 9.5. In the rotating frame, the relevant Hamiltonian without driving can be written as

$$\mathcal{H}_0^A = \begin{pmatrix} -A & 0 & 0 & 0 \\ 0 & 0 & 0 & 0 \\ 0 & 0 & 0 & 0 \\ 0 & 0 & 0 & 0 \end{pmatrix}, \tag{9.4}$$

where $A = 2\pi \times 2.19\,\mathrm{MHz}$ is the parallel hyperfine coupling constant of electron and nitrogen at low temperatures. The spin eigenstates are $|00\rangle, |01\rangle, |10\rangle, |01\rangle$.

State evolution

After generating entanglement, we start with the state

$$|1\rangle (|01\rangle - |10\rangle) / \sqrt{2}. \tag{9.5}$$

Source state preparation

We perform the desired rotation on the nitrogen spin for the $m_s = -1$ manifold, then apply a π-pulse to the electron and repeat the operation. In this way the operation on the nitrogen spin is unconditional on the electron state and the electron phase is protected by a spin-echo. With an RF operation $|1\rangle \mapsto \alpha|0\rangle + \beta|1\rangle$ this procedure yields

$$\frac{1}{\sqrt{2}} \left(\left(e^{-iA(t-t_0)} \alpha |0\rangle + \beta |1\rangle \right) |00\rangle + (\alpha |0\rangle + \beta |1\rangle) |11\rangle \right). \tag{9.6}$$
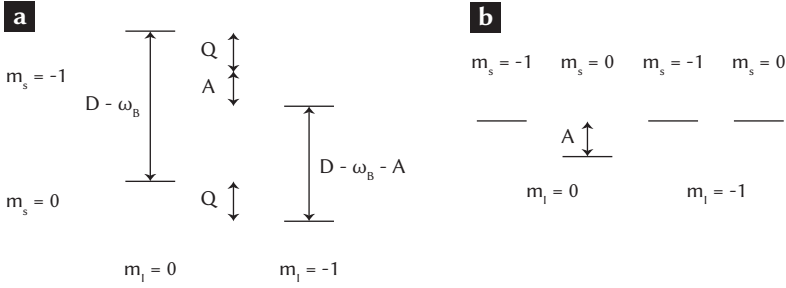
Figure 9.5 | Relevant spin states on Alice's side. a, Lab frame. **b,** Rotating frame chosen. $D = 2\pi \times 2.878\,\mathrm{GHz}$ is the NV electron zero-field splitting, $\omega_\mathrm{B} \approx 2\pi \times 50\,\mathrm{MHz}$ is the Zeeman splitting of the electron, $A = 2\pi \times 2.19\,\mathrm{MHz}$ is the electron-nitrogen hyperfine coupling constant.

Note that the states associated with $|00\rangle$ on Alice's accumulate a time-dependent phase due to the choice of rotating frame. t_0 is the time at which the π-pulse on the electron is performed during preparation. By chosing the evolution time such that $A(t - t_0)$ is a multiple of 2π the initial state can be factorized.

Bell-state measurement

The BSM consists of a CNOT rotation around the y axis on Alice's electron spin, conditional on the nitrogen spin being in $|0\rangle$, followed by a $\pi/2$ rotation around the y axis on the nitrogen spin. We implement the CNOT by rotating $m_\mathrm{I} = -1$ by π and $m_\mathrm{I} = 0$ by 2π. During this pulse Alice's states $|00\rangle$ and $|01\rangle$ are not affected. In particular, the time-dependent phase of the state $|00\rangle$ is reduced than compared to not performing the pulse (or compared to the case of an ideal CNOT gate in which only a real $\mathbb{1}$ operation would be applied to this state) because some population temporarily leaves this state. Conversely, $|01\rangle$ will acquire some phase because some population will temporarily be in $|00\rangle$. An unconditonal rotation of the nitrogen spin is achieved in the same was as for preparation, by performing the operation twice, with an electron flip in between. After these gate operations we have

$$
\begin{aligned}
\frac{1}{2}\Bigg[& |00\rangle\left(\beta\,|0\rangle - e^{i\lambda}\alpha\,|1\rangle\right) \\
+ & |01\rangle\left(e^{-iA(t_1 - t_0) - i\kappa}\alpha\,|0\rangle + \beta\,|1\rangle\right) \\
+ & |10\rangle\left(-\beta\,|0\rangle - e^{i\lambda}\alpha\,|1\rangle\right) \\
+ & |11\rangle\left(e^{-iA(t_1 - t_0) - i\kappa}\alpha\,|0\rangle - \beta\,|1\rangle\right)\Bigg].
\end{aligned}
\tag{9.7}
$$

t_1 is the time of the π-pulse on the electron, and λ, κ are the additional phases on $|00\rangle$ and $|01\rangle$.

Phase calibration

We can eliminate the undesired phases by adapting the rotation axis of the $\pi/2$ operation on the nitrogen in the BSM, and the evolution times. After initializing the nitrogen and electron spin states of Alice into $|1\rangle\,(|0\rangle - |1\rangle)/\sqrt{2}$ (equivalent to the entanglement operation on Alice, ignoring Bob), we prepare the nitrogen in $|\bar{x}\rangle = (|0\rangle - |1\rangle)/\sqrt{2}$ (preparation operation is y) and perform the BSM, yielding

$$\frac{1}{2\sqrt{2}} \Bigg[|00\rangle \left(-1 - e^{i\lambda} \right)$$
$$+ |01\rangle \left(-1 + e^{-iA(t_1-t_0)-i\kappa} \right)$$
$$+ |10\rangle \left(1 - e^{i\lambda} \right)$$
$$+ |11\rangle \left(1 + e^{-iA(t_1-t_0)-i\kappa} \right) \Bigg] \tag{9.8}$$

before readout. Calibration is therefore achieved by maximising the probabilities for outcomes $|00\rangle$ and $|11\rangle$ (Fig. 9.6).
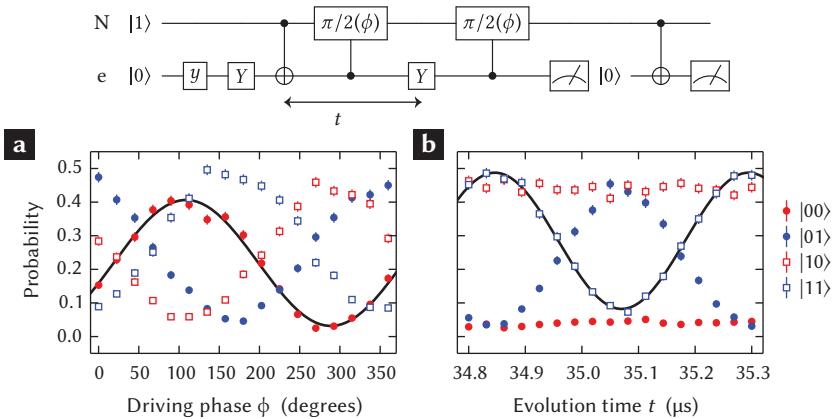
Figure 9.6 | Calibration of the Bell-state measurement. a, Calibration of the driving phase of the Hadamard operation, and **b,** subsequent calibration of the evolution time between the CNOT gate of the BSM and the electron π-pulse for the unconditional rotation of the nuclear spin. The solid lines are sinosoidal fits to the BSM outcomes to be maximised. Note that the calibration is performed with the full teleportation protocol including the MW pulses during entanglement generation attempts (but without optical π-pulses).

Dynamical decoupling of Bob's electron spin

To protect the target state against dephasing during the BSM, we perform an XY4 decoupling sequence in parallel. The first π-pulse of this echo sequence is the π-pulse performed during the entanglement generation attempt, and the remaining X-Y-X sequence during the BSM. Taking these additional rotations into account, the total state before readout, including phase calibration, is

$$\frac{1}{2}\left[|00\rangle \left(\alpha |0\rangle + \beta |1\rangle \right) \right.$$
$$+ |01\rangle \left(-\beta |0\rangle + \alpha |1\rangle \right)$$
$$+ |10\rangle \left(\alpha |0\rangle - \beta |1\rangle \right)$$
$$\left. + |11\rangle \left(\beta |0\rangle + \alpha |1\rangle \right) \right]. \tag{9.9}$$

Feed-forward

The required feed-forward operations to re-create $|\psi\rangle$ on the target spin can be taken straightforward from Eq. 9.9, see Tab. 9.1.

Table 9.1 | Feed-forward operations on the target qubit for re-creating the source state in dependence of the BSM outcome.

result N	result e	operation
$|0\rangle$	$|0\rangle$	$\mathbb{1}$
$|0\rangle$	$|1\rangle$	Y
$|1\rangle$	$|0\rangle$	Z
$|1\rangle$	$|1\rangle$	YZ

In principle we could always apply the operations as given in Table 9.1 before readout. However, if the readout result is available in real time, the target state is $U_{i,j} |\psi\rangle$ — i.e, the source state in a known rotated basis. We therefore do not apply $U_{i,j}^{\dagger}$ to recreate $|\psi\rangle$ but rotate the state directly into the readout basis. We note that this action has the same requirements as applying the operation $U_{i,j}^{\dagger}$ instead. Success of this protocol proves that we have indeed teleported the state — albeit in a different reference frame that is known in real time — without any post-selection, and that the protocol is not dependent on the input state.

For the estimation of the fidelity of the teleported state with the source state it is sufficient to read out in the basis aligned with the source state vector. This readout is achieved by rotating the target state $U_{i,j} |\psi\rangle$ into the z-basis. The required operations for feed-forward and readout are summarized in Tables 9.2 and 9.3, for entangled states Ψ^- and Ψ^+, respectively.

The feed-forward operations required in case of Ψ^+ differ from the ones for Ψ^- by a Z rotation.

Table 9.2 | Feed-forward and readout operations applied for each BSM outcome, in case of the entangled state Ψ^-.

Input	$|00\rangle$	$|01\rangle$	$|10\rangle$	$|11\rangle$	ideal result
$|{+}z\rangle = Y\,|1\rangle$	$\mathbb{1}$	Y	$\mathbb{1}$	Y	$|0\rangle$
$|{-}z\rangle = \mathbb{1}\,|1\rangle$	Y	$\mathbb{1}$	Y	$\mathbb{1}$	$|0\rangle$
$|{+}x\rangle = \bar{y}\,|1\rangle$	$\bar{y}$	y	y	$\bar{y}$	$|0\rangle$
$|{-}x\rangle = y\,|1\rangle$	y	$\bar{y}$	$\bar{y}$	y	$|0\rangle$
$|{+}y\rangle = x\,|1\rangle$	x	x	$\bar{x}$	$\bar{x}$	$|0\rangle$
$|{-}y\rangle = \bar{x}\,|1\rangle$	$\bar{x}$	$\bar{x}$	x	x	$|0\rangle$

Table 9.3 | Feed-forward and readout operations applied for each BSM outcome, in case of the entangled state Ψ^+.

Input	$|00\rangle$	$|01\rangle$	$|10\rangle$	$|11\rangle$	ideal result
$|{+}z\rangle = Y\,|1\rangle$	$\mathbb{1}$	Y	$\mathbb{1}$	Y	$|0\rangle$
$|{-}z\rangle = \mathbb{1}\,|1\rangle$	Y	$\mathbb{1}$	Y	$\mathbb{1}$	$|0\rangle$
$|{+}x\rangle = \bar{y}\,|1\rangle$	y	$\bar{y}$	$\bar{y}$	y	$|0\rangle$
$|{-}x\rangle = y\,|1\rangle$	$\bar{y}$	y	y	$\bar{y}$	$|0\rangle$
$|{+}y\rangle = x\,|1\rangle$	$\bar{x}$	$\bar{x}$	x	x	$|0\rangle$
$|{-}y\rangle = \bar{x}\,|1\rangle$	x	x	$\bar{x}$	$\bar{x}$	$|0\rangle$

Source state initialization

The source qubit is formed by the $m_I = 0$ and $m_I = -1$ states of the ^{14}N nuclear spin on Alice's side. When preparing the source state to be teleported, the following errors can occur: (1) Initialisation by measurement into $m_I = -1$ succeeds with a fidelity p_{-1}. However, there is also a (small) chance for an initalisation error and the initial state to be in either $m_I = 0$ or $m_I = +1$, with probabilities p_0 and p_{+1}, respectively. (2) During the reset of the electron spin to $m_s = 0$ by optical spin-pumping the nuclear spin can flip — with $\Delta m_I = \pm 1$ — with a probability p_{flip}.

For the feasibility of the experiment it is desirable to maintain a high repetition rate. Nuclear spin initialisation is much slower than a single entanglement generation attempt

(on the order of a few milliseconds) and can therefore not be conducted anew before each round. Further, it needs to be performed before creating entanglement, because intialisation by measurement projects the electron spin.

The reset of the electronic spin to $|0\rangle$ implies an electronic spin flip with a probability of 50 % that affects the nuclear spin: a flip occurs at a random time during optical pumping at which the hyperfine interaction between electron and ^{14}N changes, causing dephasing of the nuclear spin. We therefore aim to keep the ^{14}N spin in a pre-initialised eigenstate during entanglement generation attempts, and prepare the source state $|\psi\rangle$ after successful entanglement creation.

Due to hyperfine interaction in the orbital excited state, an electron spin flip during optical pumping can occur as part of a flip-flop process between electronic and nuclear spin[24]. Therefore, optical pumping of the electronic spin can cause randomisation of the nuclear spin eigenstates.

Population outside the source qubit Hilbert space

With a certain probability the state of the ^{14}N nuclear spin is $m_I = +1$, i.e., outside the qubit Hilbert space. In this case all RF pulses performed are non-resonant and have no effect, and the nuclear-spin controlled CNOT operations on Alice's electron have no effect either. As a result, the electronic spin — and thus, the entangled state shared by Alice and Bob — dephases before the two-qubit readout that concludes the BSM, while the nuclear spin persists in $m_I = +1$. The phase of the electron spin in our sequence is only preserved up to the CNOT operation at the beginning of the BSM. Therefore, the final readout result obtained by Bob will be fully random in this case. It is therefore fair to model $m_I = -1$ as a fully mixed state of the source qubit, $\rho_{-1} = \mathbb{1}$, for which exactly the same result is expected.

Initialization by measurement

We initalise into $m_I = +1$, $m_I = 0$, and $m_I = +1$ with probabilities p_{-1}, p_0, and p_{+1}, respectively. Additional to the mixed-state contribution from $m_I = +1$ there is a mixed-state contribution with a probability that is equal to $2p_0$ (the population of $m_I = 0$ and an equal amount of population in $m_I = -1$). The initialized state is thus

$$\rho_N(0) = [2p_0 + p_{+1}]\,\mathbb{1} + [1 - 2p_0 - p_{+1}]\,|1\rangle\langle 1|. \tag{9.10}$$

We estimate an average initialisation fidelity of $p_{-1} = 0.97 \pm 0.01$ for the NV centre used on Alice's side.

Nuclear spin flips due to electron spin-pumping

Assuming that the conditional probabiliy for a nuclear spin flop accompanying an electron spin flip, p_{flip}, is identical for all $\Delta m_I = \pm 1$, the equations describing the changes of
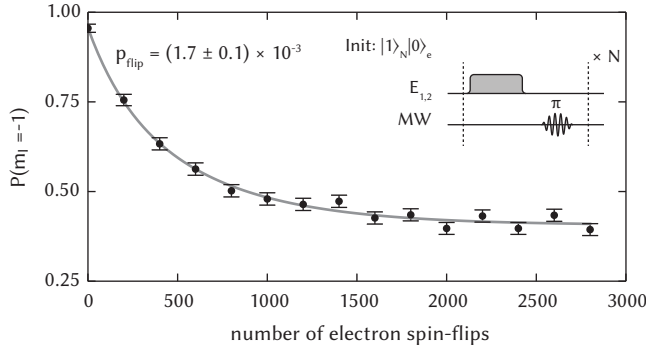
Figure 9.7 | nuclear spin state population as function of electron spin flips by optical spin-pumping. We measure nuclear spin flips that are conditional on electron spin flips when optically pumping on $E_{1,2}$. We prepare the nuclear spin in $m_s = -1$ and measure the probability for its preservation dependent on the number of cycles of electron spin-pumping $|1\rangle \rightarrow |0\rangle$ and re-preparation of $|1\rangle$ by a microwave π-pulse. The solid line is a fit to the solution of (9.11), yielding a nuclear spin-flip probability of $p_{\text{flip}} = (0.17 \pm 0.01)$ %. We note that the data shown has not been corrected for finite initialisation or readout fidelity.

populations in dependence of the number of electron spin flips, n, are

$$
\begin{aligned}
p_{-1}(n) - p_{-1}(n-1) &= p_{\text{flip}} \left(p_0(n-1) - p_{-1}(n-1) \right) \\
p_0(n) - p_0(n-1) &= p_{\text{flip}} \left(-2p_0(n-1) + p_{-1}(n-1) + p_{+1}(n-1) \right) \\
p_{+1}(n) - p_{+1}(n-1) &= p_{\text{flip}} \left(p_0(n-1) - p_{+1}(n-1) \right) .
\end{aligned}
\tag{9.11}
$$

The measured population of $m_I = -1$ in dependence of n is shown in Fig. 9.7.

Taking into account the imperfect initialization of the nuclear spin, the nuclear spin state before the RF pulse preparing the source state is

$$
\rho_N(n) = p_{\text{mixed}}(n) \, \mathbb{1} + (1 - p_{\text{mixed}}(n)) \, |1\rangle \langle 1|,
\tag{9.12}
$$

with

$$
\begin{aligned}
p_{\text{mixed}}(n) = \quad & p_0(0) \left(1 + (1 - 3p_{\text{flip}})^n \right) \\
& + \frac{1}{2} \left(-(p_{-1}(0) + p_{+1}(0))(-2 + (1 - 3p_{\text{flip}})^n) \right) \\
& + \frac{1}{2} \left((-p_{-1}(0) + p_{+1}(0))(1 - p_{\text{flip}})^n \right) .
\end{aligned}
\tag{9.13}
$$

We find a conditional probability for a nuclear spin flop to accompany an electron spin flip of $p_{\text{flip}} = (1.7 \pm 0.1) \times 10^{-3}$ for the NV centre on Alice's side under the conditions used for the

teleportation (Fig. 9.7). We therefore limit the number of entanglement generation attempts to 250 before re-initialising the nuclear spin. This corresponds to an average probability of $\sim 89\,\%$ that the nuclear spin is in $m_I = -1$ after successfully creating entanglement.

9.6 Bibliography

[1] C. H. Bennett *et al.* Teleporting an unknown quantum state via dual classical and Einstein-Podolsky-Rosen channels. *Phys. Rev. Lett.* **70**, 1895 (1993).

[2] H. J. Briegel, W. Dür, J. I. Cirac and P. Zoller. Quantum Repeaters: The Role of Imperfect Local Operations in Quantum Communication. *Phys. Rev. Lett.* **81**, 5932 (1998).

[3] D. Gottesman and I. L. Chuang. Demonstrating the viability of universal quantum computation using teleportation and single-qubit operations. *Nature* **402**, 390 (1999).

[4] D. Bouwmeester *et al.* Experimental quantum teleportation. *Nature* **390**, 575 (1997).

[5] S. Olmschenk *et al.* Quantum teleportation between distant matter qubits. *Science* **323**, 486 (2009).

[6] M. Riebe *et al.* Deterministic quantum teleportation with atoms. *Nature* **429**, 734 (2004).

[7] M. D. Barrett *et al.* Deterministic quantum teleportation of atomic qubits. *Nature* **429**, 737 (2004).

[8] L. Steffen *et al.* Deterministic quantum teleportation with feed-forward in a solid state system. *Nature* **500**, 319 (2013).

[9] S. Takeda, T. Mizuta, M. Fuwa, P. van Loock and A. Furusawa. Deterministic quantum teleportation of photonic quantum bits by a hybrid technique. *Nature* **500**, 315 (2013).

[10] G. D. Fuchs, V. V. Dobrovitski, D. M. Toyli, F. J. Heremans and D. D. Awschalom. Gigahertz dynamics of a strongly driven single quantum spin. *Science* **326**, 1520 (2009).

[11] G. de Lange, Z. H. Wang, D. Riste, V. V. Dobrovitski and R. Hanson. Universal Dynamical Decoupling of a Single Solid-State Spin from a Spin Bath. *Science* **330**, 60 (2010).

[12] T. van der Sar *et al.* Decoherence-protected quantum gates for a hybrid solid-state spin register. *Nature* **484**, 82 (2012).

[13] M. V. G. Dutt *et al.* Quantum register based on individual electronic and nuclear spin qubits in diamond. *Science* **316**, 1312 (2007).

[14] P. Neumann *et al.* Multipartite Entanglement Among Single Spins in Diamond. *Science* **320**, 1326 (2008).

[15] L. Robledo *et al.* High-fidelity projective read-out of a solid-state spin quantum register. *Nature* **477**, 574 (2011).

[16] W. Pfaff *et al.* Demonstration of entanglement-by-measurement of solid-state qubits. *Nature Phys.* **9**, 29 (2013).

[17] E. Togan *et al.* Quantum entanglement between an optical photon and a solid-state spin qubit. *Nature* **466**, 730 (2010).

[18] H. Bernien *et al.* Heralded entanglement between solid-state qubits separated by three metres. *Nature* **497**, 86 (2013).

[19] S. D. Barrett and P. Kok. Efficient high-fidelity quantum computation using matter qubits and linear optics. *Physical Review A* **71**, 60310 (2005).

[20] M. A. Nielsen and I. L. Chuang. *Quantum Computation and Quantum Information.* Cambridge University Press, Cambridge (2000).

[21] S. J. van Enk, N. Lutkenhaus and H. J. Kimble. Experimental procedures for entanglement verification. *Phys. Rev. A* **75**, 52318 (2007).

[22] S. Massar and S. Popescu. Optimal extraction of information from finite quantum ensembles. *Phys. Rev. Lett.* **74**, 1259 (1995).

[23] P. Siyushev *et al.* Optically Controlled Switching of the Charge State of a Single Nitrogen-Vacancy Center in Diamond at Cryogenic Temperatures. *Phys. Rev. Lett.* **110**, 167402 (2013).

[24] P. Neumann *et al.* Single-Shot Readout of a Single Nuclear Spin. *Science* **329**, 542 (2010).

Conclusions and future directions

The NV centre has become a very promising platform for quantum information processing and constructing quantum networks. The experiments presented in this thesis contribute to this status by expanding the capabilities of quantum control, measurements and entanglement for few-qubit registers. In this chapter we will review the current status and identify major challenges towards building large-scale quantum networks with NV centres. We discuss future research directions that will address these challenges.

10.1 Summary

The work presented in this thesis can be summarised in the following way:

1. The optical transitions of the NV centre can be manipulated coherently and the main dephasing mechanism can be overcome by a resonance preselection method.

2. We can use the NV centre with its nearby nuclear spins as a quantum register in which we can initialize, control, and projectively measure the individual qubits as well as perform conditional few-qubit gates.

3. We can obtain indistinguishable photons from two separate NV centres. Using electric fields the transition frequencies can be shifted and two NV centres brought on resonance.

4. By interfering photons from two NV centres we are able to implement a measurement-based entanglement protocol and create entanglement between remote non-interacting NV centres.

5. We can use remote entanglement between two NV centres as a resource to deterministically teleport the state of a nuclear spin onto a distant electron spin.

These results show that NV centres in diamond could serve as the building blocks of a quantum network in which few-qubit nodes that are capable of storing and processing quantum information are coherently linked together. Furthermore, these experiments and the new techniques developed enable the study of fundamental aspects of quantum mechanics [1–3].

10.2 Systems for implementing a quantum network

The realisation of a quantum network is a very active research field and is pursued by different scientific communities with different approaches on how to construct nodes that are connected via photonic channels. Each implementation has its advantages and challenges.

Atomic ensembles can be used as quantum memories that offer an optical interface. These ensembles can be laser-cooled atomic gases [4,5], room-temperature atomic vapors [6–8], or rare-earth ion doped crystals [9,10]. Entanglement has been created between two [11–13] and even four [14] separate memories. A strong point of these atomic systems is that their properties are very reproducible which makes the nodes behave almost identical. A challenge of these systems is the construction of multi-qubit registers.

Another approach is based on *individually trapped ions [15] or atoms [16,17]* which offer the advantage of reproducibility as well. A neutral atom can be placed in a high quality optical cavity which provides very efficient optical access [18]. The construction of two-qubit gates between multiple trapped neutral atoms remains challenging. In the case of trapped ions these gates can be achieved by using the coulomb interaction between the ions [19]. In order to

combine multiple-qubit operations inside the node with entanglement generation between the nodes it would be necessary to efficiently isolate the register qubits from the communication qubit[19]. This could be achieved by trapping two different ion species with different optical transition frequencies.

Solid state systems have the potential of scalability through the availability of a large range of fabrication techniques. *Quantum dots* can be incorporated inside high-quality cavities which provide an effective photonic interface[20]. Entanglement between a quantum dot and a single photon has been demonstrated[21,22]. Regarding the memory capability of the node, the coherence times of the quantum dot spin need to be extended[23]. A different solid state approach are *superconducting qubits*[24]. The challenges for this system are the coupling to a photonic channel[25,26] and extending the coherence time.

The NV centre as an implementation of a node in the network has the potential of combining the strong points of a solid state approach with the advantages of an atomic realisation. Compared to individually trapped ions and atoms, the experimental effort is relatively easy as no special techniques are needed to localise and trap single NV centres. Furthermore, solid-state fabrication techniques allow us to construct optimized devices (e.g. chapter 3.2) and show the prospect of scalability[27,28]. A remarkable feature of the NV centre is the presence of nearby nuclear spins that coherently couple to the electronic spin. These spins form a long-lived quantum memory and can be used for multi-qubit protocols. In chapter 9 we show that operation of these register spins can be combined with photonic interconnects between the nodes.

In spite of impressive progress that has been made with all of the above mentioned approaches, setting up a practical large-scale network that can be used for quantum communication and computation still remains a big challenge. In the next two sections we will identify major challenges for the case of the NV centre by looking at two potential future research directions.

10.3 Establishing entanglement over larger distances

In chapters 8 and 9 entanglement is created between two NV centres that are separated by three metres. This distance is comparable to the distances achieved in state-of-the-art experiments with trapped ions and atoms[15–17]. However, for applications in quantum communication it would be desirable to enlarge this distance much further reaching kilometres and beyond.

Furthermore, reaching these lengths could open the possibility to test fundamentals of quantum mechanics by performing a loophole-free Bell test[29–32]. If the separation of the two qubits divided by the speed of light is larger than the time it takes to measure the spin state of the qubit, communication between the two measurement results is impossible. In this way the locality loophole could be closed[33,34]. Additionally, matter qubits are well suited for closing the fair-sampling loophole as the qubit states can be measured in a single shot with
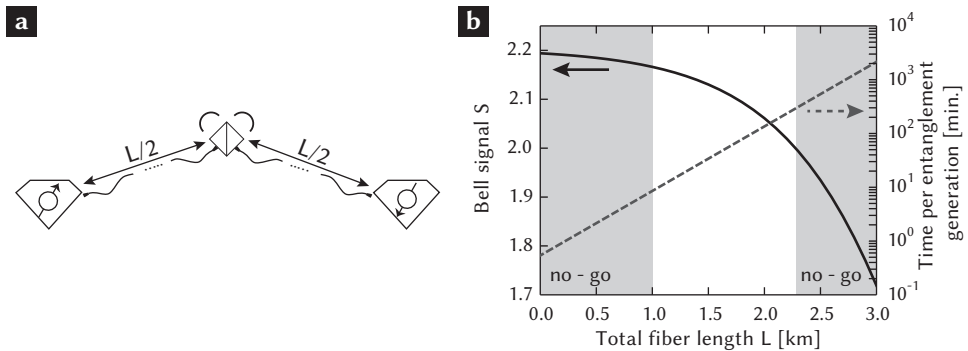
Figure 10.1 | Entanglement generation over larger distances. a, The separation between the diamonds can be made larger by increasing the length of the input arms of the fiber-beamsplitter used for entanglement generation. Choosing the two arms to be equal in length minimizes the effect of APD dark counts on the entanglement fidelity. **b,** Simulation of the Bell signal S and time it takes to generate entanglement in dependence of the total fiber length. For S > 2 a CHSH Bell inequality[30] can be violated. This defines the right 'no-go-region'. The left 'no-go-region' is given by the time it takes to read out the spins. The parameters are realistic estimates based on the experiments described in chapters 8 and 9. (Parameters: 85% initial state fidelity, 96% readout fidelity for $m_s = 0$ and 100% for $m_s = \pm 1$, 12 dB/km fiber attenuation, 1 dB additional attenuation, 20 counts/s APD dark count rate, 30 ns detection window, 14×10^{-4} detection probability for detecting a ZPL photon, 100 kHz repetition rate of the experiment)

high fidelity[2,35–37]. For the NV centre a fast single-shot readout in a few microseconds seems feasible. This means that the two NV centres should be separated by at least one kilometer in order to perform a loophole-free Bell test.

The major challenge when increasing the separation is overcoming losses in the optical paths to the beamsplitter (Fig. 10.1 a). For a wavelength of 637 nm the attenuation in an optical fiber is on the order of 12 dB/km. This not only reduces the success rate of the protocol but also lowers the fidelity (the overlap with the desired Bell state) of the entangled state as the effect of dark counts of the APDs gets larger (see also chapter 8.6.3). Figure 10.1 b shows the expected Bell signal S (for the construction of S see for example[2,35–37]) and the generation rate as the separation between the two NV centres is increased. For S > 2 a CHSH-type Bell inequality is violated[30]. The parameters are based on the measurements performed in chapters 8 and 9.

As can be seen from figure 10.1 b performing a Bell test that simultaneously addresses the fair-sampling and the locality loophole seems to be possible with the current techniques albeit with a low success rate for the entanglement generation. Increasing the distance even further within the current design would be impractical and needs technologic improvements.

One possible route for enabling larger distances would be to enhance the collection efficiency of ZPL-photons. This could be achieved by incorporating the NV centre into a cavity. An attractive architecture are fiber-based micro cavities[38,39]. Simulations for cavities with realistic quality factors indicate that the ZPL emission could be enhanced from 3% to about 30% of the overall emission and that the detection efficiency could be improved from 5% to 50%[40]. This would lead to a 10^4-enhancement of the success rate, making an entanglement generation every few milliseconds possible.

An additional strategy in order to enlarge the distance between the two NV centres would be to make use of the nuclear spins in the surroundings. In a proposal from Campbell and Benjamin[41] using one nuclear spin as an additional qubit allows for multiple tries in the second round of the entanglement scheme. This would drastically increase the success rate. Furthermore, the nuclear spins form a memory that could allow to implement quantum repeater schemes[42,43] thereby making larger distances possible.

A further approach to boost the entanglement generation rate is to convert the wavelength of the photons to the telecom band around 1300 nm or 1500 nm. At these wavelengths fibers have minimal attenuation. An implementation of this process with silicon vacancy centres in diamond reached more than 30% conversion efficiency[44].

10.4 Connecting multiple nodes

A second research direction is to increase the number of nodes involved in the network. Clearly, given the current entanglement generation rate between two nodes (about once every 12 minutes, see chapter 8) this is a long-term goal. However, following the routes described above that could drastically increase the generation rate this long-term goal seems reachable. This would open the possibility to form a graph state in which many nodes are linked together by entanglement. These states are the essential resource for measurement-based quantum computation in which one and multiple-qubit gates are realised by sequential measurements that consume the graph state[45,46].

A related approach that makes use of multiple qubits per node was proposed by Nickerson, Li and Benjamin[47]. They suggest to implement a surface code on a network in which nodes that contain four or more qubits are linked with error prone entanglement. In their scheme they reach reasonably high error thresholds (see Fig. 10.2 a) both for the linking of separate nodes (>10%) and for the inter node measurement, initialization and manipulation errors (>0.75%).

The proposed network structure is very applicable to the situation of NV centres where nearby nuclear spin can be used as the data and ancilla qubits within the node and entanglement can be created between the nodes using the electronic spin (chapter 8). High-fidelity initialization, manipulation and measurement of the electronic spin and the nuclear spins has been realised[48–51] with fidelities above or close to the required thresholds. However, combining all these operations remains a challenge.
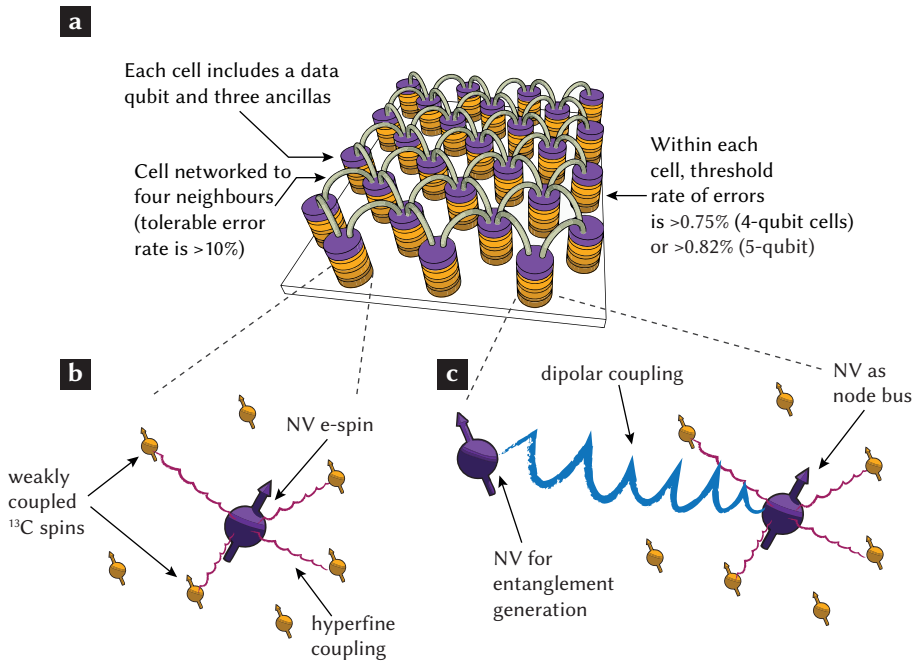
Figure 10.2 | Network for quantum computation. a, Noisy-network architecture proposed by Nickerson, Li and Benjamin to implement a surface code [47]. The nodes are linked by channels that are susceptible to errors. Figure adapted from [47]. **b,** Implementation of the node with an NV centre and weakly coupled ^{13}C-spins. For details see main text. **c,** An alternative implementation that uses two NV centres that are coupled by magnetic dipolar interaction in order to protect the node spins during entanglement generation and readout.

In particular keeping the nuclear qubits coherent while manipulating the electron spin is not trivial. Due to different hyperfine couplings for different electronic spin states, random electronic spin flips can cause dephasing of the nuclear qubits. This mechanism is more efficient the stronger the hyperfine coupling is. Initializing the electron spin by optical spin-pumping (chapter 6) which is needed for each entanglement attempt between separate nodes involves electron spin flips. This implies that the nitrogen nuclear spin and strongly coupled ^{13}C-spins are not suited as the data and ancilla qubits within each node.

An alternative choice are weakly coupled ^{13}C-spins (figure 10.2 b). These spins are not visible in a regular ESR-spectrum (see for example Fig. 6.4) because the hyperfine coupling is smaller than the linewidths observed in the spectrum. Nevertheless, using decoupling techniques these weakly coupled ^{13}C-spins can be detected [52–54] and manipulated [55]. A quantum error correction protocol has recently been implemented using a register consisting of two weakly coupled ^{13}C and the electron spin of the NV centre [55]. Even though the effect of a

single random electron flip is weaker on these spins than on the strongly coupled nuclei, it can still completely dephase the qubit. However, if the electron flip rate is increased to an extend that it is larger than the hyperfine coupling, a regime can be reached, where the nuclear spins are decoupled from the electron spin[56]. With this method a coherence time of over one second has been achieved for a weakly coupled ^{13}C-spin[57].

A second possible node implementation that separates the electron spin used for entanglement generation from the node is shown in figure 10.2 c. This architecture uses two NV centres that are close enough to each other to be coupled by magnetic dipolar interaction. One NV centre is used to generate entanglement and for readout, while the other is used to address the ^{13}C-spins within the node. The dipolar coupling can be switched off by putting one of the NV centres into the $m_s = 0$ state. NV complexes with two centres that are coupled in this way can be produced by ion-implantation[58,59].

10.5   Conclusion

A quantum network is the essential resource for distributed quantum computation and the enabling technology for secure quantum communication over large distances. Setting up such a network with NV centres is an outstanding goal that will require a long-term research effort. However, none of the challenges mentioned above are fundamental and the strategies outlined have the potential of solving these issues. On the way towards reaching this goal there will be a number of very exciting experiments performed. A loophole-free Bell test seems possible with the current techniques and the construction of a quantum repeater node would become feasible if NV centres are placed in cavities.

10.6 Bibliography

[1] R. E. George *et al.* Opening up three quantum boxes causes classically undetectable wavefunction collapse. *Proceedings of the National Academy of Sciences* **110**, 3777 (2013).

[2] W. Pfaff *et al.* Demonstration of entanglement-by-measurement of solid-state qubits. *Nature Physics* **9**, 29 (2013).

[3] M. S. Blok *et al.* Manipulating a qubit through the backaction of sequential partial measurements and real-time feedback. *Nature Physics in press* (arXiv:1311.2899).

[4] Y. O. Dudin *et al.* Entanglement of Light-Shift Compensated Atomic Spin Waves with Telecom Light. *Physical Review Letters* **105**, 260502 (2010).

[5] X.-H. Bao *et al.* Efficient and long-lived quantum memory with cold atoms inside a ring cavity. *Nature Physics* **8**, 517 (2012).

[6] B. Julsgaard, J. Sherson, J. I. Cirac, J. Fiurásek and E. S. Polzik. Experimental demonstration of quantum memory for light. *Nature* **432**, 482 (2004).

[7] K. F. Reim *et al.* Single-Photon-Level Quantum Memory at Room Temperature. *Physical Review Letters* **107**, 53603 (2011).

[8] M. Hosseini, G. Campbell, B. M. Sparkes, P. K. Lam and B. C. Buchler. Unconditional room-temperature quantum memory. *Nature Physics* **7**, 794 (2011).

[9] C. Clausen *et al.* Quantum storage of photonic entanglement in a crystal. *Nature* **469**, 508 (2011).

[10] E. Saglamyurek *et al.* Broadband waveguide quantum memory for entangled photons. *Nature* **469**, 512 (2011).

[11] B. Julsgaard, A. Kozhekin and E. S. Polzik. Experimental long-lived entanglement of two macroscopic objects. *Nature* **413**, 400 (2001).

[12] C. W. Chou *et al.* Measurement-induced entanglement for excitation stored in remote atomic ensembles. *Nature* **438**, 828 (2005).

[13] I. Usmani *et al.* Heralded quantum entanglement between two crystals. *Nature Photonics* **6**, 234 (2012).

[14] K. S. Choi, A. Goban, S. B. Papp, S. J. van Enk and H. J. Kimble. Entanglement of spin waves among four quantum memories. *Nature* **468**, 412 (2010).

[15] D. L. Moehring *et al.* Entanglement of single-atom quantum bits at a distance. *Nature* **449**, 68 (2007).

[16] S. Ritter *et al.* An elementary quantum network of single atoms in optical cavities. *Nature* **484**, 195 (2012).

[17] J. Hofmann *et al.* Heralded Entanglement Between Widely Separated Atoms. *Science* **337**, 72 (2012).

[18] C. Nölleke *et al.* Efficient Teleportation Between Remote Single-Atom Quantum Memories. *Physical Review Letters* **110**, 140403 (2013).

[19] C. Monroe and J. Kim. Scaling the Ion Trap Quantum Processor. *Science* **339**, 1164 (2013).

[20] A. Kiraz *et al.* Cavity-quantum electrodynamics with quantum dots. *Journal of Optics B: Quantum and Semiclassical Optics* **5**, 129 (2003).

[21] W. B. Gao, P. Fallahi, E. Togan, J. Miguel-Sanchez and A. Imamoglu. Observation of entanglement between a quantum dot spin and a single photon. *Nature* **491**, 426 (2012).

[22] K. De Greve *et al.* Quantum-dot spin–photon entanglement via frequency downconversion to telecom wavelength. *Nature* **491**, 421 (2012).

[23] W. B. Gao *et al.* Quantum teleportation from a propagating photon to a solid-state spin qubit. *Nature Communications* **4**, 2744 (2013).

[24] M. H. Devoret and R. J. Schoelkopf. Superconducting Circuits for Quantum Information: An Outlook. *Science* **339**, 1169 (2013).

[25] R. W. Andrews *et al.* Reversible and efficient conversion between microwave and optical light. *arXiv:1310.5276* (2013).

[26] J. Bochmann, A. Vainsencher, D. D. Awschalom and A. N. Cleland. Nanomechanical coupling between microwave and optical photons. *Nature Physics* **9**, 712 (2013).

[27] D. M. Toyli, C. D. Weis, G. D. Fuchs, T. Schenkel and D. D. Awschalom. Chip-scale nanofabrication of single spins and spin arrays in diamond. *Nano Letters* **10**, 3168 (2010).

[28] C. Derntl *et al.* Arrays of open, independently tunable microcavities. *arXiv:1309.0023* (2013).

[29] J. S. Bell. On the Einstein-Podolsky-Rosen paradox. *Physics* **3**, 195 (1964).

[30] J. F. Clauser, M. A. Horne, A. Shimony and R. A. Holt. Proposed Experiment to Test Local Hidden-Variable Theories. *Physical Review Letters* **23**, 880 (1969).

[31] J. S. Bell. *Speakable and unspeakable in quantum mechanics.* Cambridge University Press (1987).

[32] N. Brunner, D. Cavalcanti, S. Pironio, V. Scarani and S. Wehner. Bell nonlocality. *arXiv:1303.2849* (2013).

[33] G. Weihs, T. Jennewein, C. Simon, H. Weinfurter and A. Zeilinger. Violation of Bell's Inequality under Strict Einstein Locality Conditions. *Physical Review Letters* **81**, 5039 (1998).

[34] T. Scheidl *et al.* Violation of local realism with freedom of choice. *Proceedings of the National Academy of Sciences* **107**, 19708 (2010).

[35] M. A. Rowe *et al.* Experimental violation of a Bell's inequality with efficient detection. *Nature* **409**, 791 (2001).

[36] D. Matsukevich, P. Maunz, D. L. Moehring, S. Olmschenk and C. Monroe. Bell Inequality Violation with Two Remote Atomic Qubits. *Physical Review Letters* **100**, 150404 (2008).

[37] M. Ansmann *et al.* Violation of Bell's inequality in Josephson phase qubits. *Nature* **461**, 504 (2009).

[38] R. Albrecht, A. Bommer, C. Deutsch, J. Reichel and C. Becher. Coupling of a Single Nitrogen-Vacancy Center in Diamond to a Fiber-Based Microcavity. *Physical Review Letters* **110**, 243602 (2013).

[39] H. Kaupp *et al.* Scaling laws of the cavity enhancement for nitrogen-vacancy centers in diamond. *Physical Review A* **88**, 53812 (2013).

[40] Unpublished simulations performed by Christian Bonato (2013).

[41] E. Campbell and S. C. Benjamin. Measurement-Based Entanglement under Conditions of Extreme Photon Loss. *Physical Review Letters* **101**, 130502 (2008).

[42] W. Dür, H. J. Briegel, J. I. Cirac and P. Zoller. Quantum repeaters based on entanglement purification. *Physical Review A (Atomic* **59**, 169 (1999).

[43] L. Childress, J. M. Taylor, A. S. Sørensen and M. D. Lukin. Fault-Tolerant Quantum Communication Based on Solid-State Photon Emitters. *Physical Review Letters* **96**, 070504 (2006).

[44] S. Zaske *et al.* Visible-to-Telecom Quantum Frequency Conversion of Light from a Single Quantum Emitter. *Physical Review Letters* **109**, 147404 (2012).

[45] R. Raussendorf and H. J. Briegel. A One-Way Quantum Computer. *Physical Review Letters* **86**, 5188 (2001).

[46] H. J. Briegel, D. E. Browne, W. Dür, R. Raussendorf and M. Van den Nest. Measurement-based quantum computation. *Nature Physics* **5**, 19 (2009).

[47] N. H. Nickerson, Y. Li and S. C. Benjamin. Topological quantum computing with a very noisy network and local error rates approaching one percent. *Nature Communications* **4**, 1756 (2013).

[48] V. V. Dobrovitski, G. de Lange, D. Riste and R. Hanson. Bootstrap Tomography of the Pulses for Quantum Control. *Physical Review Letters* **105**, 077601 (2010).

[49] P. Neumann *et al.* Single-Shot Readout of a Single Nuclear Spin. *Science* **329**, 542 (2010).

[50] L. Robledo *et al.* High-fidelity projective read-out of a solid-state spin quantum register. *Nature* **477**, 574 (2011).

[51] F. Dolde *et al.* High fidelity spin entanglement using optimal control. *arXiv:1309.4430* (2013).

[52] T. H. Taminiau *et al.* Detection and Control of Individual Nuclear Spins Using a Weakly Coupled Electron Spin. *Physical Review Letters* **109**, 137602 (2012).

[53] S. Kolkowitz, Q. P. Unterreithmeier, S. D. Bennett and M. D. Lukin. Sensing Distant Nuclear Spins with a Single Electron Spin. *Physical Review Letters* **109**, 137601 (2012).

[54] N. Zhao *et al.* Sensing single remote nuclear spins. *Nature Nanotechnology* **7**, 657 (2012).

[55] T. H. Taminiau, J. Cramer, T. van der Sar, V. V. Dobrovitski and R. Hanson. Universal control and error correction in multi-qubit spin registers in diamond. *Nature Nanotechnology in press* (arXiv:1309.5452).

[56] L. Jiang *et al.* Coherence of an Optically Illuminated Single Nuclear Spin Qubit. *Physical Review Letters* **100**, 073001 (2008).

[57] P. C. Maurer *et al.* Room-Temperature Quantum Bit Memory Exceeding One Second. *Science* **336**, 1283 (2012).

[58] P. Neumann *et al.* Quantum register based on coupled electron spins in a room-temperature solid. *Nature Physics* **6**, 249 (2010).

[59] F. Dolde *et al.* Room-temperature entanglement between single defect spins in diamond. *Nature Physics* **9**, 139 (2013).

Summary

A quantum network is the essential resource for distributed quantum computation and the enabling technology for secure quantum communication over large distances. Setting up such a network would require establishing quantum connections between local nodes which are capable of generating, processing and storing quantum information. Intensive research is carried out in laboratories around the world investigating suitable systems for implementing a quantum network. The experiments presented in this thesis explore the possible realisation with nitrogen vacancy (NV) centres in diamond. We study how these centres could serve as nodes in such a network and develop a toolbox that consists of quantum control and measurement acting on these nodes. Furthermore, we demonstrate how to connect nodes and create entanglement between two distant NV centres.

The NV centre in diamond is a crystal defect that consists of a vacant lattice side next to a substitutional nitrogen atom. The diamond host lattice interacts very little with the NV centre due to its large band gap and the fact that the crystal consists mainly out of the spin free carbon isotope ^{12}C. In this sense the system behaves similar to a single trapped ion or atom. The NV centre has an electronic spin that can be used as a qubit in the orbital ground state, and that can be optically addressed. This spin has a remarkably long coherence time - orders of magnitude longer than the typical time it takes to manipulate this qubit by magnetic resonance techniques. Furthermore, individual nuclear spins close to the NV centre can couple coherently to the electronic spin via hyperfine interaction. These long-lived spin states can be addressed via the electronic spin and be manipulated by magnetic resonance. These properties make the NV centre a few-qubit register and an attractive candidate as a node in a quantum network.

In chapter 3 we describe our measurement techniques. We use a confocal microscope to optically address single NV centres and magnetic resonance techniques to manipulate the spin states. We enhance the collection efficiency of the microscope by fabricating solid immersion lenses into the diamond around preselected centres. The lenses increase the signal obtained from the NV centres by more than one order of magnitude, which is essential for the experiments presented in this thesis.

In order to connect separate NV centres via photons we need a coherent optical interface. In chapter 4 we investigate the optical transitions of the NV centre at low temperatures and show that we can coherently manipulate them. When applying short resonant laser pulses, we observe optical Rabi oscillations with a half period as short as 1 ns, one order of magnitude shorter than the spontaneous emission time. By studying the decay of the Rabi oscillations, we find that the decoherence is dominated by laser-induced spectral jumps and develop a method to overcome this decoherence mechanism.

The energy structure involved in the optical cycle of the NV centre is studied further in chapter 5. We use off-resonant excitation and microwave spin control to determine the spin-dependent excited state lifetime as well as the optically induced spin polarization. These

properties are governed by the inter-system-crossing probabilities between triplet and singlet energy states that are spin-dependent. We determine these probabilities and provide a full description of spin dynamics in the optical cycle of NV centres under off-resonant excitation.

In chapter 6 we develop the tools that allow us to use the NV centre together with nearby nuclear spins as a quantum register which could serve as a few-qubit node for the proposed network architecture. We implement high fidelity initialization and projective quantum measurement of the electronic spin by using spin-selective resonant excitation at low temperatures. The preparation and measurement can be extended to nearby nuclear spins by mapping their state onto the electron using microwave pulses that are conditional on the nuclear spin state. A subsequent electron readout projects the nuclear spins into a well-defined state. Finally, we show compatibility with qubit control: we demonstrate initialization, coherent manipulation and single-shot read-out in a single experiment on a two-qubit register, using techniques suitable for extension to larger registers.

For connecting distant nodes of the network via a photonic channel the photons emitted by the nodes have to be indistinguishable. We show that this condition can be fulfilled with NV centres in chapter 7. We observe two-photon quantum interference from two separate centres. Optically induced spin polarization in combination with polarization filtering allows us to isolate a single transition within the zero-phonon line of the non-resonantly excited NV centers. The time-resolved two-photon interference contrast of this filtered emission reaches 66%. Furthermore, we observe quantum interference from dissimilar NV centers tuned into resonance through the dc Stark effect.

In chapter 8 we demonstrate how to connect the nodes of the network by creating entanglement between two distant NV centres. We use a measurement-based protocol to establish entanglement over a distance of three metres between the electronic spins of two NV centres. The protocol is based on creation of spin-photon entanglement at each location and a subsequent joint measurement of the photons: The indistinguishable photons are overlapped on a beamsplitter that erases the which-path information. Detection of the photons heralds the projection of the electronic spins onto an entangled state. We verify the resulting non-local quantum correlations by performing single-shot readout on the NV centres in different bases.

Finally, we demonstrate a key capability of a quantum network in chapter 9: the transfer of an arbitrary quantum state via quantum teleportation. We demonstrate the deterministic teleportation of a nuclear spin state onto an electronic spin over three metres. We first create entanglement between the electronic spins of two remote NV centers and prepare a nuclear spin on the sender site in an initial state. By using magnetic resonance manipulation of the electronic and nuclear spins on the sender site, followed by optical readout, we are able to perform a joint measurement in the Bell basis. Feeding the result of this measurement forward by classical communication allows to recover the source state on the remote electronic spin. We prove teleportation by showing that the average fidelity of the target state with the source state exceeds the highest value allowed by classical physics.

Samenvatting

Een quantumnetwerk vormt de fundamentele bouwsteen voor gedistribueerde quantum berekeningen en het is deze technologie die veilige quantumcommunicatie over grote afstanden mogelijk maakt. Het opzetten van een quantumnetwerk vereist het aanmaken van quantumverbindingen tussen lokale knooppunten die elk in staat zijn quantuminformatie te genereren, verwerken en op te slaan. Het onderzoek naar geschikte systemen voor de implementatie van quantumnetwerken staat momenteel zeer in de belangstelling en wordt wereldwijd in verschillende laboratoria uitgevoerd. De experimenten beschreven in dit proefschrift zijn gericht op het bestuderen van een mogelijke implementatie met behulp van nitrogen vacancy (NV) centra in diamant. We bestuderen hoe deze centra kunnen dienen als knooppunten in een quantumnetwerk en we ontwikkelen verschillende relevante instrumenten gebaseerd op quantumcontrole en quantummetingen van de knooppunten. Verder demonstreren we hoe de knooppunten verbonden kunnen worden en we genereren en detecteren quantumverstrengeling tussen twee NV centra op afstand.

Het NV centrum in diamant is een kristalroosterdefect dat wordt gevormd door een missend koolstofatoom gelegen naast een stikstofatoom dat zich op de plaats van een koolstofatoom bevindt. Het diamantrooster vertoont vrij weinig interactie met het NV centrum, aangezien het een grote bandgap heeft en voornamelijk bestaat uit ^{12}C atomen die geen spin bezitten. In dit opzicht vertoont het systeem veel overeenkomsten met een enkel geïsoleerd ion of atoom. Het NV centrum heeft een elektronspin die in de orbitale grondtoestand gebruikt kan worden als quantum bit (qubit) en die optisch geadresseerd kan worden. Deze spin heeft een uitzonderlijk lange coherentietijd, ordes van grootte langer dan de typische tijden die nodig zijn om het qubit via magnetische resonantietechnieken te manipuleren. Verder kunnen individuele kernspins die zich vlakbij het NV centrum bevinden coherent gekoppeld worden aan de elektronspin via de hyperfijnwisselwerking. Deze kernspintoestanden kunnen geadresseerd worden via de elektronspin en ze kunnen gemanipuleerd worden met magnetische resonantie.

In hoofdstuk 3 worden de gebruikte meettechnieken beschreven. We maken gebruik van een confocale microscoop om individuele NV centra optisch te kunnen adresseren en magnetische resonantietechnieken om de spintoestanden te manipuleren. De collectie-efficiëntie van de microscoop wordt verhoogd doordat we zogenaamde solid immersion lenzen definiëren op het oppervlak van de diamant op de plek van geselecteerde NV centra. De lenzen verhogen het signaal van de NV centra met meer dan een factor tien, wat essentieel bleek te zijn voor de experimenten die worden beschreven in dit proefschrift.

Om verschillende NV centra via fotonen met elkaar te verbinden hebben we een coherente optische interface nodig. In hoofdstuk 4 onderzoeken we de optische overgangen van het NV centrum bij lage temperaturen en tonen aan dat we ze coherent kunnen manipuleren. Bij het aanbieden van korte laserpulsen observeren we optische Rabi oscillaties met een halve periode van 1 ns, wat een orde van grootte korter is dan de spontane emissietijd. Door het verval van de Rabi oscillaties te bestuderen, zien we dat de decoherentie voornamelijk

bepaald wordt door spectrale sprongen gedreven door het laserlicht. Bovendien hebben we een methode ontwikkeld om dit decoherentiemechanisme uit te schakelen.

Het energiespectrum dat relevant is voor de optische cyclus van het NV centrum wordt verder bestudeerd in hoofdstuk 5. We gebruiken niet-resonante excitatie en beheersing over de spintoestand door middel van microgolven om de spin-afhankelijke vervaltijd van de aangeslagen toestand, alsmede de optisch geïnduceerde spinpolarisatie te bepalen. Deze eigenschappen worden bepaald door de spin-afhankelijke waarschijnlijkheden van overgangen tussen de verschillende triplet- en singlet-toestanden. We bepalen deze waarschijnlijkheden en geven een volledige beschrijving van de spindynamica tijdens de optische cyclus van NV centra onder niet-resonantie excitatie.

In hoofdstuk 6 ontwikkelen we de gereedschappen die het mogelijk maken om het NV centrum samen met nabijgelegen kernspins te gebruiken als quantumregister met enkele qubits. Dit register kan dienen als een knooppunt voor een quantumnetwerk architectuur. We implementeren zeer betrouwbare initialisatie en projectieve quantummetingen van de elektronspin met behulp van spin-selectieve, resonante excitatie bij lage temperaturen. De initialisatie en metingen kunnen uitgebreid worden naar nabijgelegen kernspins door het overbrengen van hun toestand op het elektron met behulp van microgolfpulsen, die afhankelijk zijn van de kernspintoestand. Als hierna de toestand van het elektron wordt uitgelezen, dan worden de kernspins in een welbepaalde toestand geprojecteerd. Als laatste laten we ook zien dat deze technieken compatibel zijn met qubitcontrole en manipulatie: in een enkel experiment met een twee-qubitregister tonen we aan de qubits te kunnen initialiseren, coherent te manipuleren en op een 'single-shot'-wijze uit te lezen. De hiervoor gebruikte technieken kunnen verder uitgebreid worden voor gebruik met grotere registers.

Om verschillende verafgelegen knooppunten van het netwerk met elkaar te verbinden via een fotonisch kanaal is het noodzakelijk dat de fotonen afkomstig van de knooppunten onderling niet van elkaar te onderscheiden zijn. We tonen in hoofdstuk 7 aan dat met NV centra aan deze voorwaarde voldaan kan worden. In dit experiment observeren we quantuminterferentie tussen twee fotonen afkomstig van twee verschillende NV centra. Met behulp van optisch geïnduceerde spinpolarisatie, gecombineerd met het filteren op polarisatie kunnen we een enkele overgang binnen de nul-fonon-lijn van de niet-resonante geëxciteerde NV centra onderscheiden. Het tijdsopgeloste contrast van de twee-foton interferentie van het gefilterde signaal loopt op tot 66%. Verder observeren we quantuminterferentie tussen ongelijke NV centra die resonant gemaakt kunnen worden via het dc Stark-effect.

In hoofdstuk 8 laten we zien hoe de knooppunten van een netwerk met elkaar verbonden kunnen worden door het verstrengelen van twee verafgelegen NV centra. We gebruiken hiervoor een protocol gebaseerd op metingen om verstrengeling te genereren tussen elektronspins van twee NV centra die zich op een afstand van drie meter van elkaar bevinden. Het protocol is gebaseerd op de creatie van spin-foton verstrengeling op beide locaties gevolgd door een meting van de twee fotonen. De niet-onderscheidbare fotonen overlappen op een stralingsdeler, waardoor de 'which-path' informatie niet behouden blijft. Door de waarneming van de fotonen worden de elektronenspins op een verstrengelde toestand geprojecteerd.

We controleren de gegenereerde niet-lokale quantumcorrelaties door middel van single-shot uitlezing van de NV centra in verschillende bases.

Ten slotte laten we in hoofdstuk 9 een belangrijke eigenschap van een quantumnetwerk zien: het vermogen om een willekeurige quantumtoestand over te brengen door middel van quantumteleportatie. We tonen aan een kernspintoestand deterministisch te teleporteren op een elektronspin over een afstand van drie meter. Eerst maken we verstrengeling tussen de elektronspins van twee verafgelegen NV centra en initialiseren een kernspin op de zendlokatie in de brontoestand. Door manipulatie van de elektron- en kernspins op de zendlokatie met behulp van magnetische resonantie, gevolgd door optische uitlezing, kunnen we het systeem uitlezen in een Bell-basis. Door het resultaat van deze meting op een klassieke manier te communiceren naar de ontvangstlokatie, kunnen we de brontoestand overbrengen op de elektronspin op de ontvangst-lokatie. We bewijzen dat dit gebeurt via teleportatie door aan te tonen dat de gemiddelde overlap van de doeltoestand met de brontoestand groter is dan toegestaan door klassieke processen.

Acknowledgements

When I came to the Quantum Transport group early 2010 to apply for a PhD-position I realized quickly that QT is a very special place. Never had I discussed science with so many motivated, clever people that are totally enthusiastic about their work. Those two application days also already gave me a first taste of the great social atmosphere that rules in QT. After my visit to Delft I was convinced that this is the perfect place for my PhD and I never regretted my decision to come to Delft. During my four years here, I have tremendously enjoyed and benefited from working in such an inspiring group. Here I have found not just brilliant colleagues to do research with but also friends, and we enjoyed many QT-parties and QT-trips together. I would like to thank all the people that make QT this special place, in particular the staff who set this all up and hold it together: Hans Mooij, Leo Kouwenhoven, Lieven Vandersypen, Ronald Hanson, Val Zwiller, Leo DiCarlo, Ad Verbruggen and Erik Bakkers.

I would like to especially thank my supervisor Ronald Hanson! Ronald, you are a great scientist, a fantastic team leader and you have created all the opportunities and possibilities that any PhD student could hope for. I have learned countless things from you, not only about science. Your leadership skills amaze me. You know exactly (enough of) what is going on in the research projects, identify early which challenges might come up and jump in at the right time to solve problems. Your research vision is remarkable and goals that sound like science fiction at first become reality. Thank you also for letting me stay and work on another vision - the Bell experiment.

Team Diamond is a group of very talented and enthusiastic people that like to spend their time in the dark lab eagerly shooting laser- and microwave-pulses at helpless atoms in diamond. I enjoyed very much the dynamic and inspiring atmosphere, the great fun in the lab and outside the lab (for example at legendary Diamond-Dinners) and would like to thank everyone from Team Diamond for that. Lucio, after I started in QT, I had the chance to directly dive into experiments with you. I learned an incredible lot about physics and practical skills in the lab from you. Outside the lab we had a lot of fun on climbing, surfing and snowboarding adventures. Lily, your PhD work got me into NV-research and I was very fortunate to have the opportunity to work together with you during your stay in Delft. This was a very productive time combined with great fun! I also want to thank my senior PhDs Toeno and Gijs for a lot of help when I started, and for the awesome Diamond spirit that they started! Tim, a discussion with you always gave me new insights and ideas. Thank you for that and for your input with the experiments! Christian, great to have you in the team and to always get to enjoy Italian goodies! My fellow-PhD Wolfgang, we went through most of our PhD together. This included many good times in the lab, measuring till late and also much fun outside the lab, with many dinners, a snowboard holiday, evenings at Klooster and much more. Thanks for all of that and also for your help with the thesis and a great cover design! I wish you a great start and a successful postdoc in Yale! Bas, I enjoyed very much being the supervisor of your master project and also learned a lot from it. I am very

glad that you decided to continue in team diamond and am looking forward very much to joining you with the Bell experiment. Machiel, it is great to have you join in the cleanroom. I very much enjoy discussing science and also non-science issues with you. Hopefully, we soon start studying Korean together. It is also exciting to see a new generation of motivated PhDs join the team: Julia and Stefan. Success with your projects, I am sure you will do excellent! I also had the pleasure to supervise Gerwin with his master project. Thank you for the great contributions to the entanglement experiment and for the late-night fun in the lab! It was also great to supervise Adriaan with his bachelor and it is good to see him back for his master. Good luck to you and Oleksiy!

My PhD work benefitted a lot from excellent technical support and help I got. Thank you, Raymond and Marijn for numerous little electronic magic boxes that keep the experiments running! I would also like to thank Paul Alkemade for his help with the focused ion beam that made the solid immersion lenses work so quickly. Many thanks to Bram (don't stop whistling), Mark, Jelle and Remco for many litres of helium and help with the cryostats. I would also like to say thanks for the big administrative help from Yuki, Marja and Angele that made the organizational side of the PhD work very smoothly.

QT is not only an excellent scientific environment but also a socially welcoming one and the fun is not just restricted to the lab but often continues outside with a beer or two. Thanks to all QT members and former QT-members for the many fun times at QT-uitjes and QT-parties! Thank you Bas, Machiel, Visa, Chris, Leo DC, Stijn, Maaike and Toeno for sharing your passion for music when playing together in the QT-band. Thank you Floris for my first Dutch lessons, many nice dinners, holidays/fusion spent together and for your help with the thesis. You are always welcome to stay on the couch here in Leiden for as long as you want. Stijn, I enjoyed the many conversations we had and the Nieuwelaan together with you. I would also like to thank Basia and Reinier for many fun occasions. Good luck to you, Reinier, in Yale and success with finishing your PhD, Basia! Thank you Maria, Tim and Vincent for the nice atmosphere in the office and many discussions not just about science.

Finally, I would like to thank the ones that are closest to me: My parents, brothers and sister who are always taking an interest in what I do and who are always there for me. And HyoYun, you are the source of my happiness and I am very grateful for all the love and support during the last four years! Thank you for reminding me of all the nice things in life outside the lab. I am very much looking forward to our future together!

List of Publications

1. W. Pfaff, B. Hensen, H. Bernien, S. van Dam, M.S. Blok, T.H. Taminiau, M.J. Tiggelman, R.S. Schouten, M. Markham, D.J. Twitchen, and R. Hanson. *Deterministic quantum teleportation between remote solid-state qubits.* In preparation.

2. H. Bernien, B. Hensen, W. Pfaff, G. Koolstra, M. S. Blok, L. Robledo, T. H. Taminiau, M. Markham, D. J. Twitchen, L. Childress, and R. Hanson. *Heralded entanglement between solid-state qubits separated by three meters.* Nature **497**, 86 (2013).

3. R. E. George, L. Robledo, O. J. E. Maroney, M. S. Blok, H. Bernien, M. Markham, D. J. Twitchen, J. J. L. Morton, G. A. D. Briggs, and R. Hanson. *Opening up three quantum boxes causes classically undetectable wavefunction collapse.* Proceedings of the National Academy of Sciences **110**, 3777 (2013).

4. W. Pfaff, T. H. Taminiau, L. Robledo, H. Bernien, M. Markham, D. J. Twitchen, and R. Hanson. *Demonstration of Entanglement-by-Measurement of Solid-State Qubits.* Nature Physics **9**, 29 (2013).

5. R. Hanson, H. Bernien, M. Markham, and D. J. Twitchen *Quantum Processing Device* Patent pending WO2013053911 (2013).

6. T. van der Sar, Z. H. Wang, M. S. Blok, H. Bernien, T. H. Taminiau, D. M. Toyli, D. A. Lidar, D. D. Awschalom, R. Hanson, and V. V. Dobrovitski. *Decoherence-protected quantum gates for a hybrid solid-state spin register.* Nature **484**, 82 (2012).

7. H. Bernien, L. Childress, L. Robledo, M. Markham, D. J. Twitchen, and R. Hanson. *Two-Photon Quantum Interference from Separate Nitrogen Vacancy Centers in Diamond.* Physical Review Letters **108**, 043604 (2012).

8. L. Robledo, H. Bernien, T. van der Sar, and R. Hanson. *Spin dynamics in the optical cycle of single nitrogen-vacancy centres in diamond.* New Journal of Physics **13**, 025013 (2011).

9. Y. G. Jeong, H. Bernien, J. S. Kyoung, H. R. Park, H. S. Kim, J. W. Choi, B. J. Kim, H. T. Kim, K. J. Ahn, and D. S. Kim *Electrical control of terahertz nano antennas on VO_2 thin film.* Optics Express **19**, 21211 (2011).

10. L. Robledo[*], L. Childress[*], H. Bernien[*], B. Hensen, P. F. A. Alkemade, and R. Hanson *High-fidelity projective read-out of a solid-state spin quantum register.* Nature **477**, 574 (2011).

11. L. Robledo, H. Bernien, I. van Weperen, and R. Hanson. *Control and Coherence of the Optical Transition of Single Nitrogen Vacancy Centers in Diamond.* Physical Review Letters **105**, 177403 (2010).

[*]Equally contributing authors

12. M. Seo, J. S. Kyoung, H. R. Park, S. Koo, H. S. Kim, H. Bernien, B. J. Kim, J. H. Choe, Y. H. Ahn, H. T. Kim, N. Park, Q. H. Park, K. J. Ahn, and D. S. Kim *Active Terahertz Nanoantennas Based on VO$_2$ Phase Transition.* Nano Letters **10**, 2064 (2010).

13. M. Römer, H. Bernien, G. Müller, D. Schuh, J. Hübner, and M. Oestreich *Electron-spin relaxation in bulk GaAs for doping densities close to the metal-to-insulator transition.* Physical Review B **81**, 075216 (2010).

Curriculum Vitae

Aug. 12, 1983	Born in Rostock, Germany.
1994–2003	Secondary school, *Heinrich-Heine-Schule*, Heikendorf, Germany.
2000	Exchange year, *Pittwater High School*, Sydney, Australia.
2003–2009	Dipl.-Phys., *Universität Hannover*, Germany Thesis research under supervision of Prof. dr. M. Oestreich.
2006–2007	Studies abroad, *Beijing University*, China.
2009	Research intern, *Seoul National University*, South Korea Supervisor Prof. dr. Dai-Sik Kim.
2010–2014	PhD in Applied Physics, *Delft University of Technology*, Netherlands Thesis research under supervision of Prof. dr. ir. R. Hanson.